Spectroscopic and electrochemical study of TiO_2/Si photocathode

Von der Fakultät für Mathematik, Naturwissenschaften und Informatik
der Brandenburgischen Technischen Universität Cottbus-Senftenberg

zur Erlangung des akademischen Grades

Doktor der Naturwissenschaften
(Dr. rer. nat.)

genehmigte Dissertation

vorgelegt von

Master of Technology in Material Science and Technology

Chittaranjan Das

geboren am 25.09.1983 in Bargarh (India)

Gutachter: Prof. Dr. rer. Nat. habil. Dieter Schmeißer

Gutachter: Prof. Dr. Sebastian Fiechter

Gutachter: Jun. Prof. Dr. Ulrike Kramm

Tag der mündlichen Prüfung: 04.05.2015

Dedicated to my beloved

parents and whole of my family !

“vidyA dadAti vinayaM, vinayAdyAti pAtratAM |

pAtratvAddhanamApnoti, dhanAddharmaM tataH sukhaM”

“A true knowledge gives discipline, from discipline comes worthiness, from worthiness one gets wealth, from wealth (one does) good deeds, from that (comes) joy”

(*Hitopadesha-Indian Philosophy on Education*)

Kurzfassung

Diese Dissertationsschrift beschäftigt sich mit der Atomlagenabscheidung (ALD) dünner TiO_2-Schichten auf p-Typ Silizium, untersucht die elektronischen Eigenschaften der abgeschiedenen Schichten und beschreibt die elektrochemische Charakterisierung von TiO_2/Si-Photoelektroden. Die Abscheidungsparameter, die elektronischen Eigenschaften und die Stabilität der TiO_2/Si-Proben werden miteinander korreliert.

Mittels der ALD-Technik wurden TiO_2-Schichten mit zwei verschiedenen Prekursoren (Titan-Isopropoxid und Titan-Methoxid) auf Si-Substraten abgeschieden. Labor- und Synchrotron basierte Röntgen-Spektroskopietechniken wurden benutzt, um die abgeschiedenen Schichten zu charakterisieren. Die Qualität der Schichten wurde dabei mittels Röntgen-Photoelektronenspektroskopie (XPS) beurteilt, wobei die Stöchiometrie, das Ti^{3+}/Ti^{4+}-Verhältnis sowie Defektzustände in den TiO_2-Filmen Kriterien darstellten. Um verschiedene Polymorphe von TiO_2 zu erhalten, wurde die Heizmethode der Schichten innerhalb der ALD-Prozedur variiert.

Die elektronischen Eigenschaften amorpher und Anatas-TiO_2-Schichten wurden mittels Synchrotronstrahlung bestimmt und mit denen eines TiO_2-Rutil-Einkristalls verglichen. Röntgen-Absorptionsspektroskopie (XAS) und resonante Photoelektronenspektroskopie (res-PES) wurden mit Synchrotronstrahlung durchgeführt. Dabei diente die XAS der Bestimmung der Art des Polymorphen und der elektronischen Struktur der TiO_2-Schichten. Res-PES-Messungen wurden an den O1s- und Ti2p-Kanten durchgeführt, um Auger-Prozesse mit multiplen Loch-Endzuständen sowie polaronische und Ladungstransferzustände zu untersuchen und um die elektronische Bandlücke der TiO_2-Schichten zu bestimmen.

Eines der Hauptergebnisse dieser Arbeit stellt die Bestimmung der partiellen Zustandsdichten (pDOS) von Sauerstoff und Titan im Valenz- und Leitungsband dar. In der Analyse der res-PES-Daten wurde die pDOS mit den entsprechenden Bandkantenpositionen kombiniert, um die energetische Lage der Ladungsneutralitätsniveaus (‚Charge neutrality levels‘) der verschiedenen TiO_2-Polymorphe zu ermitteln.

Photoelektrochemische Messungen wurden an unbeschichteten und TiO_2-beschichteten Si-Photoelektroden durchgeführt. Dabei wurde die elektrochemische Performance der Photoelektroden in verschiedenen Elektrolytmedien mit pH-Werten zwischen 1 und 13 untersucht. Die Beschichtung der Si-Oberfläche mit einer dünnen TiO2-Schicht verbesserte die Performance der Si-Photoelektrode, wobei die Stabilität der Elektrode in allen untersuchten Elektrolytmedien während der gesamten Messdauer von 12

Stunden erhöht wurde. Außerdem wurde festgestellt, dass die TiO_2/Si-Photoelektrode weniger empfindlich auf Änderungen des pH-Wertes reagiert.

Die elektrochemischen Ergebnisse werden auf Basis der elektronischen Eigenschaften der TiO_2-Schichten diskutiert. Die durch die spektroskopischen Messungen bestimmte elektronische Bandlücke sowie die photoelektrochemischen Charakterisierungen werden zur Erklärung der Performance und Stabilität der TiO_2/Si-Photoelektroden herangezogen.

Die Arbeit adressiert außerdem die Stabilität von mikrostrukturierten Photoelektroden (SiMP), die elektrochemisch präpariert wurden. Zunächst verschlechterte sich die Stabilität der SiMP schneller als bei der planaren Si-Photoelektrode. Jedoch führte die Nutzung einer TiO_2-ALD-Schutzschicht auf der SiMP zu einer besseren Gesamtperformance der SiMP auch im Vergleich zum System TiO_2/ planares Si.

Abstract

This thesis focuses on the deposition of thin TiO_2 films on p-type Si using atomic layer deposition (ALD) technique, on the study of the electronic proprieties of the grown films and on the electrochemical characterization of TiO_2/Si photoelectrodes. The deposition parameters, electronic properties and electrochemical performance and stability of the TiO_2/Si samples are correlated.

The ALD technique is used to deposit TiO_2 with two different precursors namely Titanium isopropoxide and Titanium methoxide onto Si substrates. Laboratory as well as synchrotron based X-ray spectroscopy techniques are used to characterize these films. The growth quality of the TiO_2 ALD films is determined by analyzing X-Ray photoelectron spectroscopy (XPS) data in terms of stoichiometry, defect states and Ti^{3+}:Ti^{4+} ratios. The ALD technique was modified with different heating arrangements to obtain various polymorphs of TiO_2.

The ALD and anatase TiO_2 films are characterized using synchrotron radiation to study their electronic properties and these films are compared with single crystal rutile TiO_2. X-ray absorption spectroscopy (XAS) and resonant photoelectron spectroscopy (res-PES) measurements are performed with synchrotron radiation. XAS measurements are used to determine the polymorphs as well as the electronic structure of TiO_2. Res-PES measurements are conducted at the O1s and Ti2p edges to study multiple hole Auger decay processes and polaronic and charge transfer states as well as to determine the electronic band gap of the TiO_2 layers. One of the main findings of this thesis is the determination of the partial density of states (pDOS) of O and Ti in the conduction and valence band. The combination of the pDOS and the band edge positions obtained from res-PES measurements are used to calculate the charge neutrality level of the TiO_2 polymorphs.

The photoelectrochemical measurements are conducted on bare-Si and TiO_2/Si photoelectrodes. The electrochemical performance of these photoelectrodes is studied in electrolytes having pH values ranging from 1 to 13. The deposition of TiO_2 on Si enhances the photoelectrochemical performance of the Si photoelectrode. The TiO_2 increases the stability of the photoelectrode in all electrochemical media over 12 hours of experimental condition. Moreover, it is also observed that the TiO_2/Si photoelectrode is less responsive to the pH value of the electrolyte. The electrochemical findings are explained on the basis of the electronic properties of the TiO_2 layer. The electronic band gap obtained from spectroscopic measurement and the photoelectrochemical measurements are used to explain the performance and stability of the TiO_2/Si photoelectrodes. The thesis also addresses the stability of Si microstructured photoelectrodes (SiMPs) prepared by an electrochemical method. The stability of the SiMPs deteriorates more rapidly than that one of the

planar Si photoelectrode. However, using a protective ALD TiO_2 layer on these SiMPs the overall performance is even more enhanced than on the TiO_2/planar Si system.

Chapter 1

INTRODUCTION

1.1 Introduction and motivation

In the 21st century, the scientific community is looking for the alternate source of energy than the traditional fossil fuels and nuclear energy. In 1970, Honda and Fujishima introduced the concept of photocatalytic water splitting using TiO_2 as an absorber (1). Then, the photocatalytic water splitting for hydrogen became an intensive field of research due to its potential to be used as the future technology for energy. For the purpose of water splitting, generally, semiconducting materials are needed which can utilize solar irradiation to be converted into chemical energy. Among all the semiconducting materials, metal oxides are considered to be proper candidates for water splitting due to the chemical stability and easy processing. Metal oxides such as Fe_2O_3, TiO_2, Cu_2O, $BiVO_4$ etc. show the ability for catalytic water splitting. However, most of the metal oxides have unfavorable band gaps and band edge positions for water splitting. On the other hand, the semiconducting material such as Si, InP, GaP, etc are not stable in electrochemical medium. For the stability of traditional semiconductors in water splitting devices a coating of conducting and chemically stable material can be used. Hence the metal oxides can be used as conducting protective layers on semiconducting materials. Nevertheless, most of the metal oxides have low carrier density, high recombination of charges and small diffusion length. Titanium dioxide (TiO_2) has a higher electron mobility (2.3×10^{-4} cm^2/Vs) and a carrier density of around $10^{17}/cm^2$ as compared to other metal oxides and is also comparably stable in electrochemical medium. Due to its excellent electrical properties it is used as a coating material for semiconductors such as Si, InP, and Cu_2O (2) against photoelectrochemical corrosion in electrochemical systems. But the electronic and electrical properties of different polymorphs of TiO_2 films also affect the performance of the water splitting devices.

Titanium dioxide is one of the most investigated materials in the last two decades not only due to its application in water splitting but also in other fields such as dye-sensitized solar cell, pigments, cosmetics, gas sensors and photonic devices (3). TiO_2 has also the self cleaning property in which it decomposes the organic molecules attached to it and hence can be used in the self-cleaning smart windows (3). The electrochromic property of TiO_2 makes it available for application in smart switchable windows (3). Other than devices it can be used as a coating material on implants in human body due to its non-toxic property (3). The next generation non-volatile memory can be substituted by TiO_2 due to the resistance switching behavior (4).

The above mentioned application of TiO_2 involved both electronic and surface properties. Moreover, the electronic and surface properties of TiO_2 are subjected to the synthesis techniques. Therefore, depending upon the application, a specific preparation technique is adopted. For example, for the use in photocatalysis, the wet chemical route or chemical vapor deposition (CVD) techniques are preferred. Oon the other hand, for the study of resistive switching and surface coating atomic layer deposition (ALD) technique is preferred.

Apart from the application based studies, TiO_2 can be used as a model to understand the material properties of metal oxides. TiO_2 has been investigated in both the procedure of scientific studies such as experimentally and theoretically. Some of the properties like density of states, local coordination geometry, and defect states were studied theoretically but with the advancement of experimental facility such as, x-ray absorption spectroscopy, resonance photoemission spectroscopy, and resonance x-ray emission, it becomes possible to study above properties experimentally. Availability of experimental techniques to study fundamental properties of TiO_2 not only helps to understand the properties of the material but is also helpful to modify the material with in close proximity of synthesis techniques.

The aim of this thesis is to study the electronic properties in combination with synthesis techniques. The synthesis of TiO_2 films is done by atomic layer deposition (ALD) techniques using the titanium tetra isopropoxide (TTIP) and titanium methoxide. For the study of growth parameters both laboratory and synchrotron based X-ray sources are used for photoelectron spectroscopy measurements. To study the electronic properties, synchrotron based photoelectron spectroscopy and absorption spectroscopy are used. The prepared TiO_2 ALD layers are used to enhance the photocatalytic stability of the Si photoelectrodes. Finally, the relation between the spectroscopic properties of TiO_2 and the photoelectrochemical property and stability of TiO_2/Si photocathode are investigated.

In this chapter, in the later part, details regarding the studied material system explaining about the anatase, rutile and brookite phases of TiO_2 and their respective properties are given. An overview of the literature work regarding the electronic properties is also stated. Following this, the concept of photoelectrochemical (PEC) will be stated taking Si as photoabsorber. Thereafter, in Chapter 2 a description about the experimental details used is given. The experimental part consists of the synthesis technique (ALD), characterization techniques such as X-ray photoelectron emission, resonate photoelectron emission and X-ray absorption techniques using synchrotron radiation and techniques used in PEC measurements. The results of the above experiments are presented in Chapter 3 where the data presentation and explanation are given. In the final Chapter 4 the summary of the thesis and outlook are given.

1.2 Material details

1.2.1 Crystal structures

Titanium dioxide is found in three different polymorphs in nature, which are anatase, rutile, and brookite. Other than these three phases, the phase diagram of titanium oxide suggests that titanium can be bonded with different number of oxygen atoms producing Ti_2O, TiO, Ti_2O_3, Ti_3O_5 and TiO_2 at room temperature (5). Apart from these titanium oxides it can stay in a composition of Ti_nO_{2n-1} where $n \geq 4$ and the stoichiometry of these oxides lay between Ti_2O_3 and TiO_2. This group of titanium oxides is known as Magnéli phase, but this phase has less thermodynamic stability than the other phases. From the application point of view anatase and rutile are of more importance in scientific study. Both anatase and rutile have a tetragonal crystal system. In these two polymorphs Ti is surrounded by six divalent oxygen atoms with distorted octahedral arrangement. The two polymorphs differ by their distortions in octahedral arrangement (6). The octahedra in anatase share their vertices but in rutile they share edges. Among all these polymorphs of TiO_2, rutile is the most stable phase. But when the diameter of the TiO_2 nanoparticle is below 14 nm the anatase phase becomes thermodynamically more stable than the rutile phase (7). Depending on the crystal size and impurity level in anatase a heat treatment between 700 to 1000 ºC can transform anatase to rutile permanently (8). The physical properties of anatase and rutile are given in the Table 1 below:

Table 1: Important physical properties of anatase and rutile. **(3)**

Phases	Crystal system	Lattice constant (Å)	Density (Kg/m^3)	Refractive index	Electron mobility($cm^2/V\text{-}s$)	Dielectric constant
Anatase	Tetragonal	a=b= 3.782 c= 9.502	3830	2.49	10	31
Rutile	Tetragonal	a= b=4.587 c= 2.953Å	4240	2.903	1	86

In Figure 1 the unit cell of rutile (left) and anatase (right) are shown. In the unit cell of rutile TiO_2 the position of Ti atoms are at [0,0,0] and [½,½,½]; each of them is surrounded by six oxygen atoms. The oxygen atoms surrounding Ti do not form a square in the equatorial plane since the TiO_6 coordination polyhedron is distorted. In the rutile structure the bond angle between the O-Ti-O bonds in the plane of shortest distance are 98.9º and 81.07º causing the shape of a distorted octahedron. In the rutile TiO_2 the bonds length of equatorial Ti-O bond is 1.946Å and the epical Ti-O bond length is 1.983Å. The lattice constants of rutile TiO_2 is a=b= 4.587Å, c= 2.953Å [(8) (9)]. The bond length of the titanium and oxygen atoms in TiO_2 is presented in Table 2 for anatase, rutile and amorphous phases.

Table 2: The bond length of Ti-O and O-O in the TiO_2 (rutile).

Bond length	**Rutile (Å)**		**Anatase (Å)**		**Amorphous (Å)**		**Ref.**
	Apical	Equatorial	Apical	Equatorial	Apical	Equatorial	
Ti-O	2.0	1.97	2.0	1.95	1.94		(9)
O-O	**Edge sharing**	**Corner sharing**	**Edge sharing**	**Corner sharing**	**Edge sharing**	**Corner sharing**	
	2.56	2.8	2.49	2.82	2.67		(9)

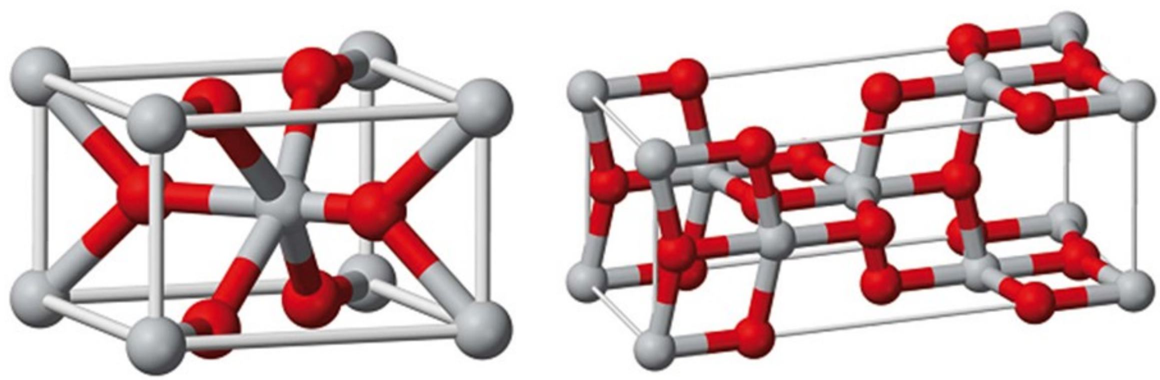

Figure 1: Unit cell of rutile on the left with lattice constants (a = b = 4.587Å, c = 2.953Å) and anatase on the right with lattice constants (a = b = 3.782Å, c = 9.502Å). In the stick ball diagram, the red balls represent oxygen and the white balls titanium atoms.

The Ti atoms in the anatase unit cell occupy the positions at [0,0,0,], [½,½,½], [0,½,¼] and [-±½,0,3/4]. The lattice constants for anatase are a=b=3.782Å, c= 9.502Å [(10) (11)]. The bond length of Ti-O in the equatorial plane is 1.937Å and along the apical direction the Ti-O bond length is 1.966Å. In this case also each Ti atom is coordinated a six O atoms to form a distorted octahedron. Unlike rutile, in anatase the equatorial oxygen atoms are not in the plan that forms the octahedron. In the equatorial plane the two oxygen atoms opposite to each other are below the plane and other pair of oxygen atoms above the equatorial plane. The bond angle of O-Ti-O for short and long bonds is 102.308º and between the two short bonds is 92.604º. The position of the O atoms and the angle between O-Ti-O result in anatase in a more distorted octahedron than in rutile.

In the rutile crystal the TiO_6 octahedral units are connected to two neighboring octahedra by sharing edges along the [001] direction and connected to eight TiO_6 unitby sharing the vertices along the plane of (001) (12). On the other hand, anatase TiO_6 octahedra are connected to four neighbors by sharing edges along the directions [100] and [010] forming a zigzag chain (3).

1.2.2 Electronic structure

In this section the electronic structure such as VB, CB edges, band gap, defect states and electronic properties from XAS of Ti $L_{2,3}$ edge will be discussed. The electronic structure discussed here will be based on previous experimental as well as theoretical studies on TiO_2.

1.2.2.1 Valence band and conduction band

Titanium as a d-group element has the electronic configuration [Ar] $3d^2$ $4s^2$ and that of oxygen is $1s^2$ $2s^2$ 2p4. Ti^{4+} and O^{2-} react with each other to form TiO_2 resulting in electronic configuration of $O2p^6$ $Ti3d^0$ $4s^0$. The ratio of Ti to O in a perfect TiO_2 crystal is 1:2. Ti^{4+} cation has a small diameter which enables it with strong polarization power and as a result of this TiO_2 has 70% of ionic and 30% of covalent bond character (13). Mostly the density functional theory (DFT) method is used to calculate the electronic structure of TiO_2. By using this calculation method the band gap is determined by taking the energy separation between the highest occupied state (or the valance band maxima VBM) and the lowest unoccupied state (or the conduction band minima CBM). According to the theoretical calculation the valence band (VB) consists of mainly O2p and the conduction band (CB) of Ti3d states (14). The contribution of individual atoms in the VB and CB presents the partial density of states (pDOS) and their combined contributions in each band represent the total density of states (DOS). With the advancement of computational power the calculation methods are providing more detailed insight in the electronic structure of these metal oxides. In the recent calculation it has been demonstrated that the VB has a considerable contribution of Ti3d states and the CB has a certain contribution of O2p states [(15) (16)]. The presence of Ti3d states in the VB and of O2p states in the CB leads to a hybridization of O2p and Ti3d states to form VB and CB [(17)]. The lower part of the VB is consisting of O2s and the width of this state is 1.9 eV on the other hand, the width of the upper part of the VB is around 6.22eV for anatase. In case of rutile the lower VB has a width of 1.94 eV, the upper VB is 5.9eV. The CB width for both anatase and rutile are around 5.9 eV (18).

The contribution of O2p and Ti3d states in the VB is mostly studied in theoretical works. The resonance photoelectron spectroscopy can be used to investigate the contribution of O2p and Ti3d states in the VB experimentally. In the resonant photoelectron spectroscopy measurements on rutile TiO_2, Drera et al. (19) showed the VB at 8.2 eV to have a higher intensity which corresponds to the O2p-Ti3d hybridization while the VB at 5 eV results due to non-bonding states of Ti-O. Eventually they also observed two satellite peaks in the VB region at binding energy (BE) around 12 and 18.5 eV. The satellite peaks especially the peak at 12 eV, has constant BE below the resonance photon energy. The photoemission peaks correspond to the $Ti3d^2 4p^2$ initial states. When the photon energy approaches the resonance energy the intensity of this peak increases as well as the BE is changing and leads to an Auger decay (LVV) at higher photon energy. The satellite has constant BE below the resonance photon energy due to the excitonic like state that is localized in the band gap of rutile.

Table 3: Comparison of band gap rutile determined by different calculation method band gaps are calculated considering it as a direct band gap.

	Rutile		**Anatase**		
Method	Band gap (eV)	Reference	Method	Band gap (eV)	Reference
PP-PAW	1.70	(20)	DFT+PBE	1.94	(21)
Variational density functional perturbation	1.87	(22)	LDA	2.00	(23)
PWGGA	1.90	(24)	PPCFs	2.02	(9)
PP-PW	2.03	(25)	OLCAO	2.04	(26)
SCC-DFTB	2.46	(27)	LSD-GGA+U	2.40	(28)
PP	2.80	(29)			
LCAO-BZW	3.05	(30)	GGA+HF	3.54	(31)
LCMTO	3.25	(32)	B3LYP	3.68	(33)
HF-PP	3.4	(34)	PBE–G0W	3.73	(21)
DFT-HF Hybrid	3.54	(24)	HSE06–G0W0	4.05	(21)
PBEO-LCAO	4.05	(35)	PBE+25%HF	4.50	(36)

1.2.2.2 Band gap of TiO_2

The minimum distance between the CBM and VBM in rutile is at the Γ point and hence it has a direct band gap (18). Recent calculations by Chinedu et al. showed that rutile can have an indirect band gap (30). On the other hand, the theoretical calculations have shown that anatase can have both a direct and indirect band gap [(23), (31)]. The theoretical determination of the band gap on subject of different calculation methods and the consideration of potential. The band gap of rutile ranges from 1.7 eV to 4.45 eV depending upon the calculation methods [(20), (35)]. In Table 3 the band gaps calculated by different methods are shown.

The differences in the band gap of TiO_2 with different calculation methods show the limitation of the calculation methods. Especially in the case of the DFT calculation method, the proper description of electron-electron correlations (37) cannot be taken into account and also have the problem with the residual electron self-interaction (38). More over the calculation method is more likely to be useful for predicting the electronic structure of TiO_2 in the ground state. These limitations in calculation method cost in the estimation of proper width of band gap. To eliminate the problem of self interaction of electrons in the calculation method, Vladimir et.al introduced the Hubbard potential (U) [(39), (40)]. The term U is added to the localized orbitals in which the electrons have repulsive interaction and for the calculation of hybrid density functional method is used [(41), (42)]. The hybrid density functional method has contributions of the Hartree-Fock exchange and DFT exchange-correlation functional theory. The inclusion of U into the theoretical measurements provides accurate value for band gap in comparison to the experimental band gap. However, the selection of the values of U is empirical in order to match the band gap to the experimental value. In the work of Dompablo et al. is demonstrated that with the different weight of U value the band gap of both anatase and rutile changes in both calculation methods such as GGA and LDA as shown in Figure 2 (a) (16). In another work Vu et al. also showed that with DFT+U calculation the band gap can increase from 2.5 to 4.5 eV with U values from 3 to 10 eV in Figure 2(b) (43). The experimental band gap of rutile and anatase TiO_2 is found to be 3.0 and 3.2 eV (3).

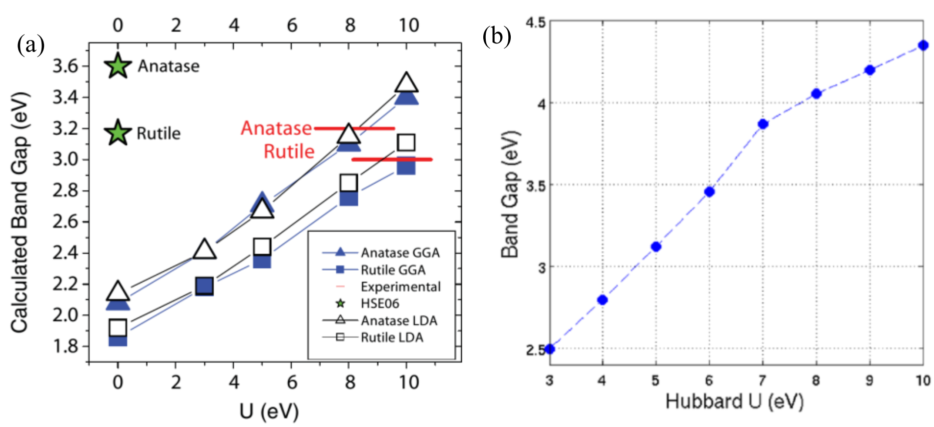

Figure 2: Band gap calculations of anatase and rutile using LDA+U and GGA+U (a) and using DFT+U for anatase TiO_2 with different values of U. The figures are reproduced from [(16), (43)*].*

The experimental band gaps obtained by optical measurements point at indirect band gaps, of both TiO_2 phases, which are often compare with the electronic band gap of TiO_2 obtained by theoretical calculations. However, in theoretical calculations the many body interaction and excitonic effects are not taken into consideration. Due to the ambiguous comparison between two quantities, the band gap of TiO_2 seems to be different in each case. The electronic band gap of TiO_2 is generally obtained determining the VBM position from UPS measurements and the CBM from inverse photoemission spectroscopy (IPES) The band gap obtained by this method is about 3.6±0.5 eV for rutile (44). The electronic band gap determined from dipoles allowed transitions and from experimentally determined dipoles allowed a gap of 4.2 eV (45). The presence of the excitonic states also affects the electronic band gap of TiO_2 in all the polymorphs. In the anatase polymorph, the excitonic states are localized while in rutile these states are delocalized. The work of Letizia et al. shows the compression of the electronic and optical properties taking into consideration many-body correction (46). The transition involved here are at 3.42, 3.55 and 3.59 eV in anatase. The optically active transition is only possible at 3.59eV while the other two transitions at lower energy are dark excitons. The transition at 3.59 eV is related to bright excitons. The dark excitons below the allowed optical transition are caused by O2p to the farther Ti3d states while in case of optically allowed (bright) transition the O2p electron will be excited into the Ti3d states. The theoretical calculation here are in agreement with the experimental value due to the consideration of electron-hole interaction in the calculation method.

The experimental electronic band gap of TiO_2 can be obtained from the analysis of X-ray electron spectroscopy. The XPS is able to identify the VBM of TiO_2 while XAS can be used to define the conduction band edge. The VB XPS and XAS are aligned to the Fermi level to determine the electronic band gap of TiO_2. From XPS (VBM) and XAS (CBM) the band gap of anatase and rutile is 4.15 and 4.72eV respectively (47). In another work the band gap of TiO_2 is determined from X-ray emission spectroscopy (XES) and XAS. In this case the band gap in this case determined 2.6 eV, which is far below the optical band gap of TiO_2 (48).

1.2.2.3 Defect states in TiO_2

In semiconducting materials defect states play an important role since they can change both the electrical and the optical properties of the semiconductors. Modifying the defect states can tailor the material properties of the semiconductors. In case of $TiO_{2,}$ is a matter of whether the defect states are mainly due to the oxygen vacancies or due to titanium interstitials, but there are some studies where the oxygen interstitial defects are also described. In the literature, it is always discussed that the defects in

TiO_2 comes from the reduction of TiO_2.The reduction process can result in the formation of TiO_{2-x} or $Ti_{1+x}O_2$.

After reduction, when TiO_2 is converted into TiO_{2-x}, the defects in the material are caused by the formation of oxygen vacancies (V_O) due to the removal of oxygen atom. But it has also been found that TiO_{2-x} can also crystallize in a stable Magnéli phase with a stoichiometry between Ti_2O_3 and TiO_2. When the stoichiometric ratio of O to Ti is less than 2 ($x > 10^{-4}$), the highly reduced TiO_2 can give rise to the formation of crystallographic shear (CS) planes. The CS plans in TiO_2 help to eliminate the defect in the material [(49)]. Defects due to oxygen vacancies have been modeled and observed by both experimental and theoretical methods. Moreover in case of anatase and rutile, the oxygen defect states can be produced by using difference process of reduction method. In theoretical studies, the position of oxygen vacancy defect states in TiO_2 is a matter of concern. In earlier studies the oxygen vacancy defect states are considered to be at the bottom of the conduction band and are delocalized [(50)]. With the improvement of computational methods the introduction of self-interaction of electrons (Hubbard U) into the calculation methods give rise to the observation of delocalized defect states in the band gap at about 1 eV below the conduction band edge [(51), (28)]. On the other hand, defect states have been observed by different experimental groups using X-ray photoelectron spectroscopy (XPS) (52), ultraviolet photoemission spectroscopy (UPS) (53), and electron energy loss spectroscopy (EELS) (54) located at, around 1eV below the Fermi level.

After reduction of the TiO_2 it is possible that an extra Ti atom occupy an interstitial site of TiO_2 providing a defect state in it. The interstitial Ti defect in TiO_2 acts as a shallow donor (55). The interstitial defect in TiO_2 is mainly practical by theoretical calculations. The interstitial defect also creates a localized state in the band gap. In the work of Cho et al. using LDA, it is demonstrated that the existence of an interstitial defect state is at 0.2 eV below the conduction band minima (20). In another work, Lee et al. (56) calculated the electronic states using the screened exchange (sX) hybrid density functional method. They found that the interstitial Ti defect is around 0.7 to 1.3 eV below the conduction band depending on the charge of the defect. The oxygen vacancy (V_O) with zero charge lays at around 0.7 eV to 2 eV below the conduction band depending on the charge at the defect side. There are less experimental evidences for Ti interstitial defects in TiO_2 than for oxygen vacancies. Most of the work is based on UPS studies using TiO_2 single crystal. In photoelectron emission experiments [(57), (58)] the interstitial defect in TiO_2 is found to be at around 0.7 to 0.9 eV below the conduction band minimum.

In TiO_2 both type of defects (oxygen vacancy and titanium interstitial) are formed by reduction of TiO_2. It has been explained that when the sputtered reduced TiO_2 is oxidized by vacuum annealing the Ti interstitials get into the bulk (59). On the other hand by annealing the reduced TiO_2 in the presence of O_2 the Ti interstitials migrate to the surface (58). In the theoretical work of Robertson et.al it has also been shown that the energetic positions of oxygen vacancies and Ti interstitial in the band gap overlap with each other (56). From the theoretical and experimental studies it is difficult to conclude which kind of defect states is present in TiO_2. It is possible that both, oxygen vacancies and he Ti interstitials co-exist as defect states in TiO_2.

There is a small number of studies describing the oxygen interstitial defects in TiO_2. In this type of defect the extra oxygen atom does not stabilize as a charged species in the interstitials position of the lattice. The extra oxygen will bond to the oxygen in the lattice forming O-O bonds (50). Unlike the oxygen vacancy it works as an electron trap in TiO_2 as observed by theoretical calculations increasing the bond length of O-O from 0.970 to 1.484 Å (60).

1.2.2.4 XAS of Ti $L_{2,3}$-edge

The X-ray absorption spectroscopy is one of the most important spectroscopic techniques to study the electronic and structural properties of the materials. It is also helpful to correlate changes in intrinsic properties with the local chemical environment. In this method the electron from the Ti2p orbital is excited into the Ti3d states which are supposed to be the empty states. The XAS at Ti $L_{2,3}$ edge allows to probe into the empty states of Ti3d states which has an effect on the local symmetry, coordination and bonding with the O atom. While experimental data of XAS are consistent the theoretical counterpart has more variation regarding the explanation about the cause of XAS peaks at the $TiL_{2,3}$ edge. To explain the origin of the peak in the XAS spectra the orbital crystal field theory is most accepted where the transitions are marked for $Ti2p_{3/2}$ to t_{2g} and eg states showing peaks at the L_3 edge and $Ti2p_{1/2}$ to t_{2g} and e_g states showing peaks at the L_2 edge (61). The orbital crystal field theory is based on the independent single particle system. But under experimental conditions the result is not due to the single particle system because in the orbital crystal field calculation the interaction between the core hole and the excited electron is neglected along with the particle interaction between them. In recent theoretical works, the above mentioned points are taken into consideration to explain the XAS spectra of the $TiL_{2,3}$ edge. The hole-electron interaction is considered in Bther-Salpeter equation (BSE) to produce XAS spectra. This calculation is successful in reproducing the XAS spectra of $SrTiO_3$ (62) while rutile TiO_2 (63) was not matching the experimental data. Time dependent density functional calculation have been used by Fronzoni et al. to simulate the XAS spectra of TiO_2 but these spectra poorly agree with the Ti $L_{2,3}$ edge of rutile TiO_2 (64). Recently, it could be demonstrated that the first-principle multichannel multiple scattering (MCMS) method with the core hole-electron interaction (excitons) to calculate the Ti $L_{2,3}$ edge XAS spectra (65) is in agreement with the experimental spectra. The contributions of individual transitions at the L_2 and L_3 edge are also determined by this method to explain the splitting of e_g at L_3 edge. In another work published by Blaha et al. the BSE calculation method is used to calculated the XAS at early 3d elements where the $TiL_{2,3}$ edge spectra are well reproduced (66). Moreover the branching ratio and the spin orbit splitting in XAS are also reproduced with this method.

1.3 Photoelectrochemical (PEC) water splitting

The photoelectrochemical (PEC) water splitting is the light driven process of electrolysis with the help of photoelectrocatalysts that perform act as specific electrodes in order to separate H_2 and O_2 from water (67). In this process the photoexcited electrons will react with the electrolyte to reduce the water to produce H_2 whereas the photo excited holes will react with electrolyte to perform oxidation of water for O_2 generation. Both, the reduction and oxidation of water can be performed using semiconducting electrocatalysts that can absorb light or employing an absorber with a co-catalyst on top of the electrode surfaces to improve the water splitting process. For the purpose of splitting of water into H_2 and O_2 (electrolysis) the total amount of energy required is 237 KJ/mol. The equivalent of electrical energy is 1.23V. In the process of photoelectrochemcial water splitting the photon energy is converted into electrical energy and then the electrical energy is converted into chemical energy. The PEC water splitting can be formed by using only semiconducting materials which can absorb the photons to convert them into electrical energy. A schematic presentation of the PEC water splitting using a semiconductor electrode is shown in the Figure 3.

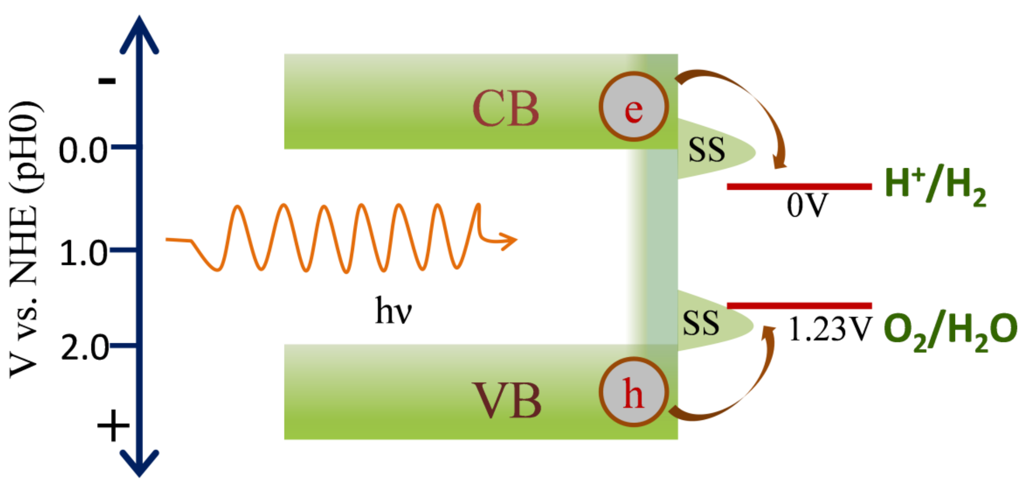

Figure 3: Schematic diagram of a photoelectrocatalytic water splitting system. The band edge positions are related to the energy scale at the left side. The abbreviation SS represent the surface states on semiconductor.

In a semiconducting material photons of appropriate energy generate pairs of charge carriers (electron-hole). The generated charge carriers will move from the semiconductor surface to the electrolyte and interact with the electrolyte to perform redox reaction as shown in the Figure 3. The photo excited electrons from the conduction band of semiconductor react with the electrolyte to trigger the hydrogen evolution reaction (HER) while photo-excited holes in the valence band will react with the electrolyte to provoke oxygen evolution reaction (OER). The generation of H_2 and O_2 is only possible when the photovoltage generated by the semiconductor electrodes is ≥1.23V. There are certain requirements for photoelectrocatalytic water splitting using semiconducting materials which are listed below;

- **Band gap and band edge position of the semiconductor**

Semiconductors that can be used for water splitting should generate a photovoltage of at least 1.23 V. Hence the semiconducting material should be able to absorb light of photon energy energies >1.23 eV i.e the light of a wavelength ~1000 nm and shorter should be absorbed by these kind of semiconductor materials and generating electron-hole pairs. Even under ideal conditions, the semiconducting material should have a band gap of 1.7 eV . Only a semiconductor with such a band gap can produce enough photovoltage to be required for photoelectrochemical water splitting. Under experimental condition there are lots of factors due to which the PEC system losses energy. The loss of energy in PEC device is determined by (i) polarization within the PEC, (ii) poor charge separation and recombination of photo-generated electron-hole pairs, (iii) overpotentials required for OER and HER, (iv) electrical resistances of both electrodes (v) IR drop in the electrolyte and (vi) contact resistance at the electrodes. All these factors contribute to a total loss of ≥ 0.4eV in the PEC system (67). Therefore a suitable semiconducting material needed for water splitting should have a band gap of about ~ 2.2 eV (68).

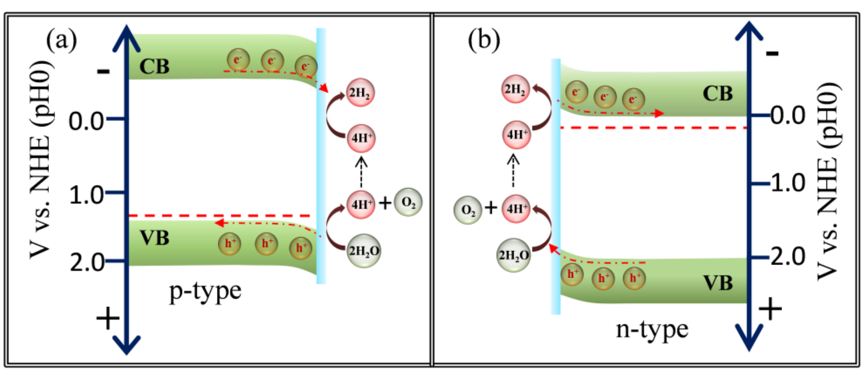

Figure 4: Schematic diagrams of the band alignment of semiconductor for overall HER and OER. In figure (a) a p-type semiconductor band edge position for HER and in figure (b) an n-type

semiconductor band edge position for OER are shown. The band edge positions are shown with respect to the electrochemical scale related to normal hydrogen electrode (NHE) potential.

Other than the band gap itself the energetic band edge positions with respect to the redox potentials are precondition to guarantee efficient water splitting performance by the semiconductor electrode. To generate the potential for water splitting valence band edge and conduction band edges need to be more positive to oxidation potential and more negative to reduction potential, when respectively using the electrochemical scale. Correct valence and conduction band edge positions with respect to redox potentials of water for effective water splitting are shown schematically in Figure 4.

- **Electrical properties of photoelectrodes**

The efficiency of a photoelectrochemical device also depends on the electronic properties of the semiconducting material. The charge carrier life time, its diffusion length, the rate recombination of photoexcited electron-hole pairs and the resistivity of the semiconductor will influence the photoelectrocatalytic performance of the PEC device [(69), (70)].

- **Stability against chemical and photo corrosion**

The corrosion of photoelectrodes in contact with an electrolyte is one of the most important issues of PEC water splitting. Most of the semiconductors used for water splitting are not stable for a long time in a photoelectrochemical environment. The exposure of the semiconductors in the aqueous electrolyte deteriorates the activity of the semiconductors. Most of them are either photo-corroded or change to some other inactive form of the same material. In the electrochemical process in aqueous electrolyte the photoelectrodes have to move through an anodic and/or cathodic process resulting in oxidation or reduction of photoelectrodes. The photoanodes are stable against photoelectrochemical corrosion when the free enthalpy of oxidation (E_{pd}) is more negative than the oxidation potential of water and the photocathodes are stable when the free enthalpy of reduction (E_{nd}) is more positive than the reduction potential of water reduction as presented in the equations below (71).

$$E(O_2/H_2O) < E_{pd} \tag{1.1}$$

$$E(H^+/H_2) < E_{nd} \tag{1.2}$$

The above mentioned properties are necessary for an ideal PEC water splitting system. After the discovery of the PEC water splitting device by Fujishima and Honda (1) lots of efforts have been put to identify appropriate semiconducting materials for PEC water splitting device.

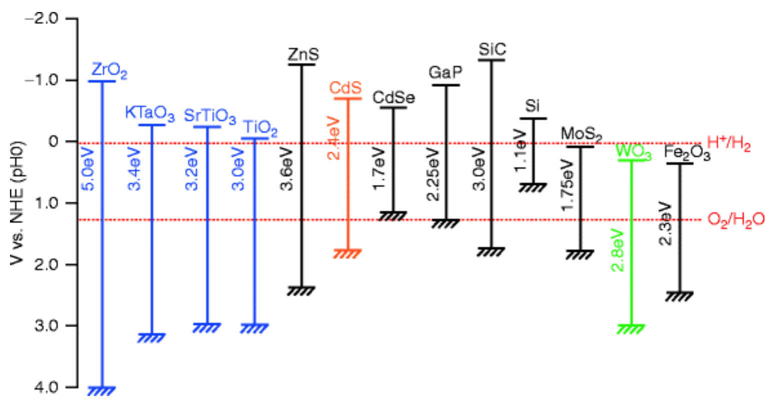

Figure 5: The band gap and band edge position of the most investigated semiconducting material with respect to the redox potentials of water for photoelectrocatalytic water splitting **(72)**.

The Figure 5 shows the band edge position of different semiconducting materials with respect to the redox potentials of H_2O (72). Among all these categories of semiconducting materials most of them are either not stable in an electrochemical environment or do not fit into the requirements for a water splitting electrode. The compound semiconductors such as p-InP with an efficiency of 12% (73) in the process of hydrogen evolution can be used for PEC device, but these materials are very prone to electrochemical corrosion as compared to oxides. On the other hand transition metal oxides such as TiO_2, Fe_2O_3, WO_3 etc. are very stable in an electrochemical environment but the band edge positions, and the band gaps are not favorable for efficient water splitting. Under these conditions, the combination of two semiconductors can be used in a tandem cell in PEC devices for water splitting. The semiconducting material silicon can be used in a tandem cell configuration for light induced water splitting.

1.3.1 Si as a photoelectrodes for PEC device

Silicon with its most established technology for a device preparation and processing has been very successful in the field of photovoltaics. With a band gap of 1.1eV and excellent electronic properties such as high mobilities and a change in conductivity by doping can also be used in photoelectrochemical systems for water splitting devices. Apart from the band gap for absorption of light, the band edge position of a Si electrode is one of the crucial factors for water splitting. The valence band edge of the Si is about 0.63eV more negative than the water oxidation potential and the conduction band about 0.5eV more negative of the reduction potential of hydrogen in solution at pH 0 as shown in Figure 6 using the electrochemical scale. Since p-Si has its CB above the reduction potential H_2/H^+, it can be used as photocathode in a half cell geometry to run the hydrogen evolution reaction. Therefore, it needs an external potential to split water electrochemically. Such a potential can be supplied using a p-n Si tandem cell.

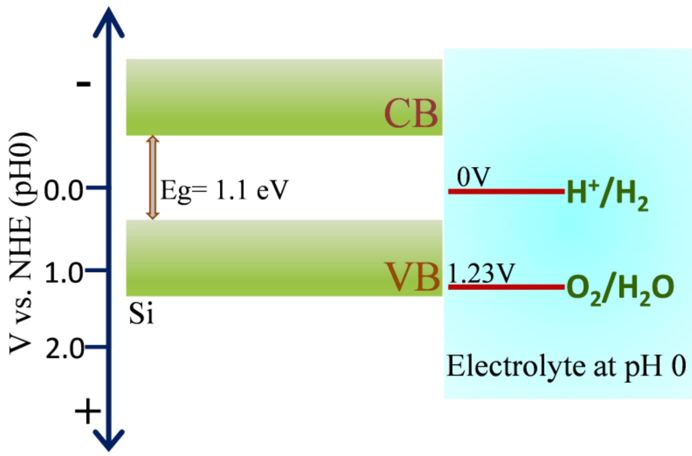

Figure 6: Schematic band edge positions of Si with respect to the redox potential of water splitting at pH 0 under equilibrium conditions.

As discussed above due to the small band gap of silicon, neither a p- nor an n- type Si photoelectrode can be used for water slitting alone. Moreover, to perform the oxidation reaction employing a semiconducting oxide higher pH values (~13) as found in KOH or NaOH electrolytes have to be used while for reduction reaction low pH electrolytes (e.g. 1M H_2SO_4) are frequently used. The electrolyte condition affects the performance of the Si photoelectrodes. In addition to this, Si has no catalytic effect, i.e the charge carriers migrating across the Si-electrolyte interface cannot perform chemical reactions efficiently. So for efficient electrical to chemical energy conversion, the Si surfaces must be covered with a co-catalyst.

The n-type Si in PEC device needs higher overpotentials and a co-catalyst to perform water splitting. Other than the photo-electrical problem, one of the most important challenges involved with Si photoanode is the photo corrosion. When n-type Si is illuminated with photons photo-generated electron-hole pairs get separated at the Si-electrolyte interface. The electrons move to the cathode via the back contact while the holes interact with electrolyte. The hole simultaneously interacts with both electrolyte and Si surface. As a result of oxidation both, the electrolyte and the Si surface, gets oxidized. Formation of SiO_2 on Si deteriorates the photoelectrochemical activity of Si over the period. To retain the photoelectrochemical activity of n-Si the surface oxidation in the photoelectrochemical medium needs to be checked. From early eighties till date, Si as photoanode has been studied and the performance and stability have been increased over the time. Various approaches have been made to protect the electrode of n-type Si against photoelectrochemical corrosion. Among these the distinguished works are chemical passivation introducing H-terminated (74)or a methylizated Si surface (75) but also the formation of a SiO_2 layer with Au nano emitters (73), coating of Si with various conducting materials such as graphene

(76) and TiO_2 is possible[(77), (78)]. The thin layer of conducting TiO_2 seems to be promising to check the photocorrosion of n-Si in PEC device whit out affecting the photo activity.

P-type Si has a better electrochemical stability than n-type Si but the charge transfer rate at the Si surface to the electrolyte is very small which leads to a low quantum yield (79). More over the band edge position of p-Si is such that it can generate only 550mV of photo-voltage. This amount of voltage is not enough to carry out redox reaction in electrolyte. Therefore, a p-type Si photocathode needs to be coupled with a catalyst to obtain efficient PEC water splitting. The catalyst such as noble metal Pt (80) or other metal based catalyst such as MoS_2 (81), Ni, NiMo (82) have been used to improve the catalytic properties of p-Si. The depositions of the catalyst on Si photocathodes are done by electrochemical, chemical or vapor deposition techniques. During the process of catalyst deposition on Si it gets oxidized and the photocatalytic activity decreases. In addition to the fabrication of Si photocathodes when the photocathode is merged in the electrochemical medium it gets oxidized over the time which limits the catalytic activity of Si photocathode.

The PEC device can be brought to day life use only when the stability of the device can be extended. For this the device need to be work self sufficiently, i.e., the PEC device must be able to produce ~2.0 V to perform water splitting and must be stable under acidic and/or alkaline condition. Nocera et al. developed an artificial leaf that can produce O_2 and H_2 without any external biased (83). But the stability of this device last for 12hours only. Moreover, this type of tandem PEC cell is not understood properly. Therefore the device technology needs to be developed for long term stability and understanding of PEC devices.

In the present study, we investigate the effect of TiO_2 on Si photocathode when the deposition is carried with the ALD method. The properties of the deposited TiO_2 over layer are studied by X-ray photoelectron spectroscopy and are correlated with the photoelectrochemical measurements from TiO_2/Si photocathodes.

Chapter 2

EXPERIMENTAL

This chapter is dedicated to the description of experimental techniques used in this thesis. The experimental part is divided into two parts: techniques used for preparing sample and techniques used for characterizing the samples. The technique involved in synthesis of TiO_2 is the atomic layer deposition (ALD). The grown samples are investigated with spectroscopic techniques such as x-ray photoelectron spectroscopy (XPS) using both laboratory and synchrotron sources, and X-ray absorption spectroscopy (XAS) using synchrotron radiation at the BESSY II beamline U49/2-PGM2. The functioning details about ALD will be given and will be followed by the spectroscopic experimental details.

2.1 Atomic Layer Deposition (ALD)

The idea for atomic layer deposition (ALD) of thin film was carried out by Prof. S.I. Kol'tsov in 1960s in USSR. Later on the experimental success of ALD deposition film was brought by Prof. V.B. Aleskovskii (84). But in 1970s the technique was rediscovered by Suntola et al. (85) and brought into the use in scientific research as well as industrial application. The research in this field of deposition techniques is intensified after 1990s and till today it is a major field for research due to its application in semiconductor industry.

The ALD process belongs to the family of vapor to solid deposition techniques used for deposition of thin films. The special features of ALD such as conformality coating of complex structures, control over the thickness in atomic scale and pinhole free thin film deposition, make it advantageous over the other deposition techniques such as chemical vapor depiction (CVD), physical vapor deposition (PVD) and molecular beam epitexy (MBE). ALD does not need very high temperature for the deposition and it can work under atmospheric pressure, so it can be used to deposit material on any kind of substrates.

The ALD process is a continuous cyclic deposition process. Each of these cycles consist of two half cycles and each of the cycles carry different precursors to the substrate. These half cycles does not allow the two precursors to interact with each other in the gaseous phase inside the reaction chamber. The half cycles can be divided into two parts mainly the first part carries the precursor to the substrate and the second part purges the unreacted and or byproducts of the gas. The working concept of the ALD process can be understood from Figure 7.

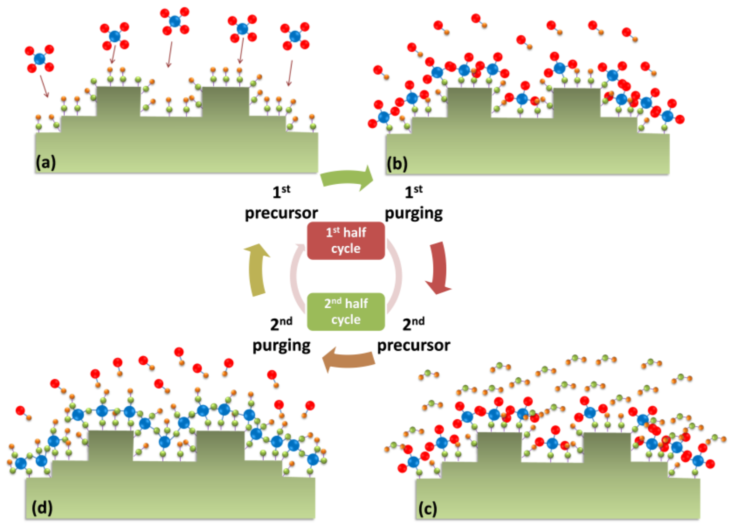

Figure 7: Schematic diagram of atomic layer deposition process: (a) the first precursor is inserted and chemisorbed on the surface, (b) purging with nitrogen to remove the remnants after chemisoprtion, (c) insertion of the second precursor to react with the first one on the substrate and (d) final purging to remove by products.

A schematic description of the ALD process is presented in the figure 3 and it consists of four steps with two half cycles. In the step 1 as shown in Figure 7(a) the gaseous species will be inserted into the reaction chamber. The gaseous precursor will be chemisorbed on the surface and this reactant species will perform self terminating reaction. This means that only a monolayer of the precursor can be absorbed on the substrate and the extra amount of precursor will not react with the absorbed species. In the second step the unabsorbed and un-reacted species need to be removed. So the reaction chamber is purged with nitrogen gas to remove the unreacted species. For the purging generally nitrogen or other inert gases are used, so during the purging the gas will not react with the absorbed species. After purging the second reaction species is inserted into the reaction chamber to react with the absorbed species in the third step. In this step the second reacting species will remove the blocking group in the first reactant that is responsible for self termination. This chemical reaction will give to a layer of desired material and this layer of desired material is also self terminated. After the completion of this process the reaction chamber need to be purged with nitrogen in the final step as shown in Figure 7(d) to remove the byproduct. This final step produces the desired material without any byproducts on it. For the growth of the desired thickness of a film these cycles are repeated in the sequential order.

The deposition of film starts in the first cycle of ALD, so the growth rate in this technique is calculated as growth per cycle (GPC). In this technique the sample is stabilized first by heating treatment. Each cycle in ALD is self limiting, so the growth rate cannot be changed changing the ALD parameters such as precursor pulse time, purging time and time between each pulses. The temperature or some other parameter that will change the reaction mechanism on the substrate can only change the growth rate. The growth is controlled by only the surface properties of the substrate and hence ALD is known as a surface controlled process.

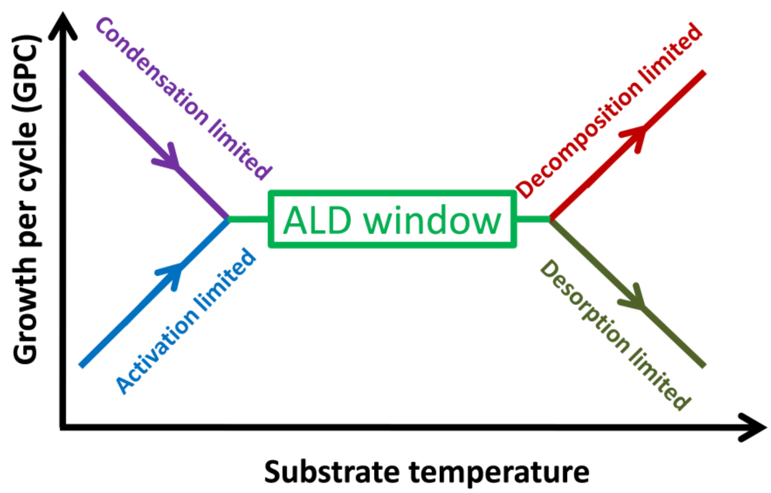

Figure 8: Schematic representation of ALD processing window growth rate vs. substrate temperature and different regions of ALD processing temperature.

The substrate temperature is a crucial parameter for growth rate and the quality of the films grown by ALD. The ALD process is successful in certain range of temperature and this temperature range is the ALD window. The schematic diagram of ALD window is shown in Figure 8 above. The growth rate and the film quality do not change in the operating window of ALD. Before the ALD window the precursor either condensed in the chamber or has not enough energy to react with the surface. When the precursor has not enough energy to react the GPS is lower than normal ALD and when the precursor condensate the GPC is higher than normal ALD. On the other side of the ALD window (higher temperature) the precursor may decompose or desorbed from the substrate. In this temperature range, the decomposition of precursor will lead to the increase in the growth rate of the material where as desorption of the precursor from the substrate results in slower growth of the material.

2.2 Characterization Techniques

The material prepared by ALD is characterized by X-ray photoelectron spectroscopy (XPS) and X-ray absorption spectroscopy (XAS). The growth process of TiO_2 is characterized by XPS with the laboratory X-ray source system where the detail study about the growth and the spectroscopic properties of TiO_2 is conducted by XPS and XAS using synchrotron radiation at BESSY II, Berlin with beamline U49/2-PGM2.

In this portion of the chapter a short description about the synchrotron radiation with specification of the beam line U49/2-PGM2 used for experiments will be given. It will be followed by details of different experimental methods like XPS, XAS, res-PES and data interpretation from respective methods.

2.2.1 Synchrotron radiation

The X-rays are highly energetic electromagnetic radiation discovered by Wilhelm Conrad Röntgen in 1895 in Würzburg (86). The X-rays are produced when the accelerated electrons collide with a target and the electrons lose their energy in the form of heat and radiation. In the process of collision 99% of energy is lost as heat and only 1% contributes to the radiation. The radiation coming out of this collision is highly energetic and these rays are known as X-rays. The wavelength of the X-ray ranges from 0.01 to 10 nm and that of energy ranges from 100 eV to 100 keV. X-ray tubes are the primary source of X-ray in the laboratory and these kinds of sources cannot change the energy of the X-ray.

In 1930's high-energy physicists studied the collision of subatomic particle where the particles have constant speed in the circular path. The constant speed of the particles in the circular path is maintained by accelerating in a fixed frequency electric field using magnetic field. During the circular motion the particles emit unwanted electromagnetic radiation which is generally known as cyclotron radiation. The x-ray radiation are realized when the velocity /energy of the electron are increased and this radiation is known as synchrotron radiation. The effect velocity of electron and synchrotron radiation was discovered by Elder, Gurewitch, Langmuir, and Pollock in 1946 (87).

Figure 9(a) shows the schematic diagram of a synchrotron radiation facility (88). In the first step the electron generated in the electron gun is accelerated to the speed near to the speed of light. The accelerated electron is inserted into the booster ring where the electrons are achieved the 99.9999985% of the velocity of light. The accelerated electron from the booster is inserted into the storage ring where it travels in a circular path speed equivalent to the velocity of light.

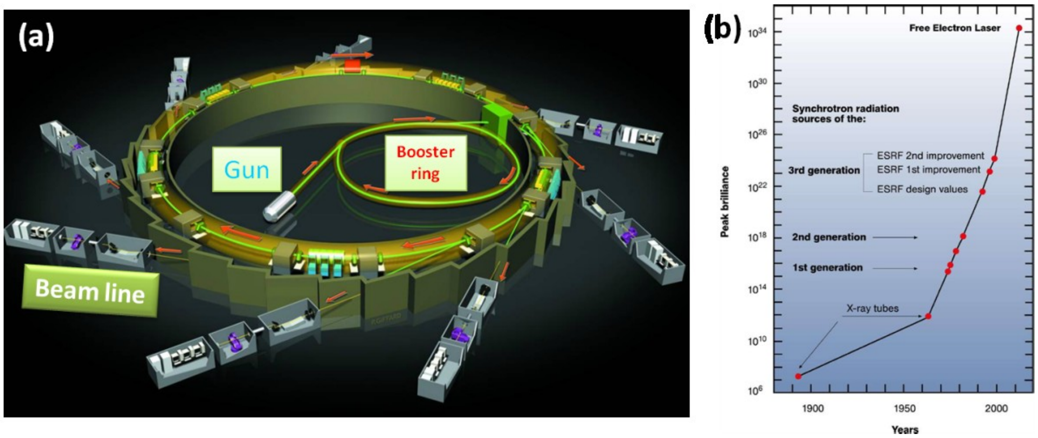

Figure 9: A schematic diagram of synchrotron a radiation facility (a) and curve of the advancement of X-ray light source over the years (b). The images are taken from (89) (a) and (90) (b).

When the highly energetic electrons move in the circular path of the storage ring they emit synchrotron radiation on changing of their trajectory. The trajectories of the moving electrons are changed by bending magnets and the wigglers and undulators known as insertion devices. The electron beam when changes its path due to the magnet the electron oscillate perpendicular to the magnetic field direction. The oscillations of the electron beam give rise to the emission of X-rays as synchrotron radiation. The opening angles of the magnets provide different spatial distribution in the radiation and the opening angle (1/γ) is defined as in equation 2.1:

$$\gamma = \frac{E}{m_0 C^2}, \tag{2.1}$$

where E is the energy of electron (in GeV), m_0 is the rest mass of the electron and C is the speed of light.

The beam lines carry the emitted radiation from the synchrotron ring to the experimental station. The X-ray radiation is monocromatized by using a grating monochromator and the desirable photon energy can be obtained with tuning of the monochromators. One of the interesting features of synchrotron based X-ray source is the photon flux. The photon flux is defined as the number of photons per time and relative energy width. On normalizing the photon flux to the angular divergence the brightness of the X-ray can be obtained. When the brightness is normalized to the area of the radiation source the brilliance of X-ray is obtained and the brilliance can be given as in equation 2.2. The brilliance of X-ray light source over the years is shown in Figure 9(b) [(89)]

$$Brilliance = \frac{number\ of\ photons}{sec.mrad^2.0.1\%\ energy\ band\ width} \tag{2.2}$$

2.2.2 Experimental setup at synchrotron

The experiments at BESSY II are carried out with the beam line U49/2 PGM2. The insertion device of this beam line is an undulator and it consists of 84 periods and is 49.4 mm long. The monochromator used in this beamline has a plane grating with 1000 and 300 lines per mm [(90)]. The photon energy from 85 to 1890 eV can be obtained with the accuracy higher than 0.1 eV. This range of energy is covered by three odd harmonics (1st, 3rd, and 5th) and with the change in energy the harmonics change automatically. For calibration of the beamline photon energy, N_2 gas phase 1s→π* edge absorption spectra is used. The brilliance at different photon energy of the beamline is shown in Figure 6 (a) with the three harmonics.

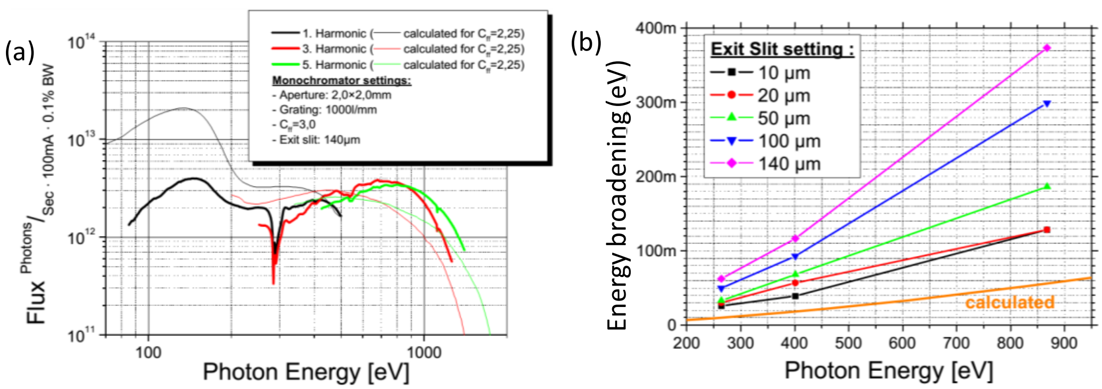

Figure 10: Brilliance of U49/2 PGM2 beam line at different photon energy (a) and the broadening of photon energy with different slit width for different photon energy (b).

The energy resolution of the photon energy depends on the exit slit width. Figure 10(b) shows the dependence of energy broadening with the exit slit width. The broadening here is from the photon energy not from the experimental resolution determined by the analyzer. For the experiment in multi bunch hybrid mode generally the 20 and 30 µm are used for XPS and XAS respectively, but at low α mode higher slit width such as 50 µm is used.

The end station of beamline has ASAM system with SPECS Phoibos 150 hemispherical electron analyzer for photoelectron spectroscopic (PES) measurements. For the XAS measurements two Keithley picoamperemeter devices are employed where one of these device used to measure the sample current to get the total electron yield (TEY) and another is used to measure the current (I_0) due to the photon flux on refocusing mirrors. The Specs Lab 2 software is used to control and to collect the data from measurements. The software is connected to the beam line computer to change the photon energy for X-ray absorption measurements. The ability of software to change the photon energy and measure the record data from analyzer and Keithley devices enable us to perform the experiments like PES, XAS, CIS, CFS and res-PES with the same instrument.

2.3 Experimental methods

2.3.1 X-ray photoelectron spectroscopy (XPS)

X-ray photoelectron spectroscopy (XPS) is a surface analyzing technique to study the elemental composition of the surface. Due to the elemental specific application of XPS, it is also known as electron spectroscopy for chemical analysis (ESCA). The XPS system was first developed by Siegbahn and coworker in mid 1960's at the University of Uppsala, Sweden (91). In this method of surface characterization, the surface is illuminated with monochromatic light which cause the emission of electrons from the illuminated surface. The monochromatic source of light can be the gas discharged lamp as source of UV light , or the commercial laboratory based X-ray sources such as Mg Kα (1253.6 eV) and Al Kα (1486.6 eV). Another source of monochromatic X-ray is synchrotron radiation where a range of monochromatic X-ray can be obtained according to the requirements. XPS techniques are very surface sensitive due to the low attenuation length of photoelectrons. The attenuation length depends on the photon energy hence the synchrotron radiation enables to get the electron from different depth from the surface of the material.

2.3.1.2 XPS theory

The electrons in the core level of molecules are localized to a specific atom like the electrons localized in atomic orbital. These core levels in the molecules are filled with the electronic density of states and these core levels are quantized in nature. This means the discrete core levels have discrete energy and the energy differences between each level are large enough to be distinguished. In the process of X-ray photoelectron spectroscopy the energy level of the electrons are determined to identify the element. In a simplified picture, when the surface is bombarded with monochromatic light (X-rays) of energy $h\upsilon$ (h is Plank's constant and υ is the frequency of the light) the electron from the surface will be ejected with certain kinetic energy (E_k). From this the binding energy (E_B) of the electrons (core levels) can be determined using the equation 2.3:

$$E_B = h\nu - E_k - \phi, \tag{2.3}$$

where, ϕ is the work function of the material.

The analyzer measure the kinetic energy of the emitted electrons and the accuracy of measurement depends on the calibration of the analyzer. When the analyzer and the sample are in electrical contact the Fermi level can be taken as the reference other than the work function. Since it is not always easy to determine the work function of the investigated materials, taking Fermi level as reference point for experiment is more convenient. In such case the equation 2.3 can be simplified as in equation 2.4.

$$E_B = h\nu - E_k \tag{2.4}$$

The binding energy is the finger print of the orbital as well as the material itself. Other than the core level binding energy of the electrons depends on the final state configuration of the core levels after the emission of electrons (relaxation/ screening of the core hole) (ΔE_{relax}), the chemical environment of the atoms ($\Delta E_{chem.}$) and also the electron correlation (ΔE_{corr}) and the relativistic energy (ΔE_{rel}).

$$E_B = \Delta E_{atomic} + \Delta E_{chem} + \Delta E_{relax} + \Delta E_{corr} + \Delta E_{rel} \tag{2.5}$$

There are more effects from the final state that affects the binding energy of the emitted electrons and the line shape of the spectra. One of the strong effects of final state is the spin-orbit coupling. Due to the spin-orbit coupling the XPS peaks for none zero angular momentum quantum number (p, d, and f sub shells) split into two peaks. The spin-orbit coupling gives rise to two possible states with two different values of spin s (parallel spin and anti parallel spin) and is given by $j = l \pm s$. For p-orbital core level with one electron out the j value will be 3/2 and 1/2 for spin s ½ and -½ respectively. The $p_{3/2}$ peak will be at lower binding energy where as $p_{1/2}$ will be at higher binding energy. The spin-orbit split peaks have branching ratio according to the multiplicity $m = 2j + 1$. For p-orbital core level the $p_{1/2}$ and $p_{3/2}$ have the branching ratio of 1:2. The final state effect also contributes to another peak which is called the shake-up satellite. In this process the emitting electrons on the way lose their energy to excite valence electrons in to the conduction band (unoccupied state). These emitted electrons with less kinetic energy than the core electrons have peak at higher binding energy and this peak is known as shake-up satellite.

In the final state the relaxation process can occur through two processes. In one case the core hole can be filled with the electron from the higher orbital and the extra amount of energy can be released as photons. In the second case the core hole can be filled with another electron from the higher sub shell and the difference amount of energy will knock out another electron. This ejection of electron due to relaxation process is known as Auger electron.

2.3.1.3 Application of XPS

The photoelectron spectroscopy can be used to get information about both the qualitative and quantitative properties of the material on the surface. In the qualitative analysis, binding energy of emitted electrons can be used to know the chemical composition and chemical status of the element in compound.

In the quantitative analysis, the information about the quantity of each component in a chemical compound (elemental ratio) and composition of a surface into the surface (depth profile) can be obtained.

- **Chemical composition and the oxidation state of element**

The photo emitted electrons from same orbital have different energy for different elements. The equation 2.5 offers a unique value for each element, which makes possible to have information about the elemental composition on the surface.

On the other hand the binding energy can shift due to the chemical environment or the chemical state of the element in the material. The shift in binding energy depends on number of electrons taking part in chemical bonding and as well as type of chemical bonding. Due to the chemical bonding when the population of electrons in the outermost shell decreases the effective charge experienced by the core electron increases and hence the binding energy shift to higher binding energy position. On the other way around when the population of electron in the outer most shell increases the effective charge experienced by the core electron decreases and hence the binding energy moves to lower energy. The shift in binding energy (ΔE_B) is given by equations 2.6 and 2.7.

$$\Delta E_B = \left(E_f^{A(N-1)} - E_i^{A(N)}\right) - \left(E_f^{B(N-1)} - E_i^{B(N)}\right) \tag{2.6}$$

$$\Delta E_B = \left(E_i^{B(N)} - E_i^{A(N)}\right) - \left(E_f^{B(N-1)} - E_f^{A(N-1)}\right) \tag{2.7}$$

where E_i is the initial state energy, E_f corresponds to final state energy, and A, B correspond to two different atoms.

- **Elemental ratio of the surface**

Photoelectron spectroscopy can also be used to determine the elemental ratio on the surface of the material. The intensity of the spectra depends on the concentration of the element present. More physically the intensity depends on certain factors like incident photon flux (φ), atomic density (*n*), atomic cross section for the transition to occur (σ), the inelastic mean free path at the desired photon energy (λ), the distance (*x*) and the angle (θ) at which the photoelectrons are collected. Mathematically the intensity of the PES (*I*) is given by the equation 2.8.

$$I = \varphi n \sigma \int_0^\infty e^{-x/\lambda cos\theta}\, dx$$

$$I_\infty = \varphi n \sigma \lambda cos\theta \tag{2.8}$$

For different elements the above factors are different and hence when the intensity of two elements is compared these factors must be taken into consideration. Considering two elements A and B on the surface the intensity of these two elements can be given as I_A and I_B. The physical parameters affecting the intensity of the PES can be defined as atomic sensitivity factor S. The values for inelastic mean free path and the atomic cross-section can be obtained from the data base [(92), (93)]. The ratio of the two elements present on the surface can be determined by taking the ratio of peak intensity after back ground correction as shown in the equation 2.9.

$$\frac{A}{B} = \frac{I_A/S_A}{I_B/S_B} \tag{2.9}$$

The same approach can be used to determine the ratio between oxidation states in the material by taking the intensity ratio of each peak due to the different oxidation states.

- **Depth profiling**

In the quantitative analysis the PES spectra can also give information about the composition of the material from the surface to deep into the material. The depth profiling can be done in two ways, destructive depth profiling and non destructive depth profiling. In the destructive depth profiling the ion beam is used to etch the surface layer by layer and after each layer the XPS spectra is recorded in order to determine the chemical composition. On the other hand the non destructive depth profiling can be done using different photon energies, which can only be done using synchrotron radiation. Since the emitted electrons have different inelastic mean free path at different photon energy the information from different depth of the sample is obtained.

With the concept of depth profiling the thickness of the over layer grown on a substrate can be determined with PES.

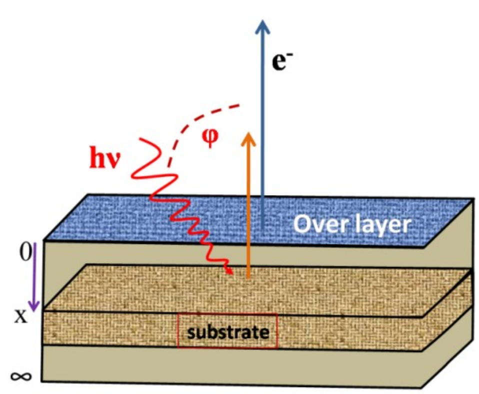

Figure 11: Schematic diagram of substrate and over layer for PES measurements.

Figure 11 shows a substrate covered with an over layer. The intensity of the substrate, I_s, is generally given by the equation 2.10.

The intensity of the substrate is given by

$$I_s = \emptyset \sigma n \lambda_s \cos\theta \exp\left(-x/_{\lambda_s \cos\theta}\right) \tag{2.10}$$

However, in this case, I_s will be attenuated by the extra mean free path offered by the over layer:

$$I_{sov} = \phi \sigma n \lambda_{sov} \cos\theta \left[1 - \exp\left(-x/_{\lambda_{sov} \cos\theta}\right)\right], \tag{2.11}$$

where λ_s, and λ_{sov} are the inelastic mean free paths of the substrate before and after adding an over layer.

On solving the equation the thickness of the over layer is obtained as following

$$x = \lambda_s \cos\theta \ln\left(\frac{\lambda_{so}}{\lambda_s} . \frac{I_s}{I_{so}} + 1\right) \tag{2.12}$$

Or with over simplification it can be given as

$$I_{sov} = I_s \exp\left(-x/_{\lambda_{sov}}\right) \tag{2.13}$$

2.3.2 X-ray absorption spectroscopy (XAS)

X-ray absorption spectroscopy (XAS) is another process of photon in electron out through the photo electric effect. In XAS process the X-ray of energy ranging from hundred eV to tens of KeV is absorbed by the material depending on their X-ray absorption cross section (σ). The absorption probability of the X-ray for specific material is given by Lambert Beer's law:

$$I = I_0 \exp(-\mu x) \tag{2.14}$$

Where I_0 and I are the incident and transmitted intensity of X-ray respectively, μ is the absorption coefficient and x is the thickness of the material. The absorption coefficient μ is the inverse of the penetration depth.

The X-ray excites the electrons belonging to the strongly bonded core level or weakly attracted electrons in valence band into the unoccupied state or continuum states. The XAS spectra are measured as the absorption intensity with the photon energy. The intensity of the XAS peak is proportional to the electron excitation probability from initial state to final state P_{if}. Hence the absorption cross section (σ_{if}) can be defined according to Fermi's golden rule,

$$\sigma_{if}(E) = \frac{P_{if}}{\emptyset} = \left(\frac{4\pi\hbar}{m}\right)^2 \frac{\alpha}{\hbar\omega} \left|\langle\psi_f\middle|e\hat{P}\middle|\psi_i\rangle\right|^2 \rho_f(E) \tag{2.15}$$

Where α is the fine structure constant (1/137), e is the direction of the electric field vector and P is the dipole moment operator. The total absorption cross section can be given by integrating over the σ_{if}.

$$\sigma(E) = \sum_{i,f} \sigma_{if} \tag{2.16}$$

The density of state $\rho_f(E)$ in the infinite final state life time will have definite contribution when the transition energy will be $E_{if} = E_f - E_i$.

Equation 2.15 implies, the absorption cross section will have a definite value when the electron from the core state (*i*) will move to the final state (*f*) upon excited by X-ray incident light. The possible transition from initial state to final state depends on the energy of the X-ray and the dipole selection rule. When the incident X-ray have lower energy than the binding energy of the initial state electron then the electron will not movie to the final state obtaining the absorption cross section value zero. When the photon energy is higher than the binding energy of the initial state electron then the x-ray will be absorbed and the electron will be transferred from initial to final state if the dipole selection rule will be satisfied. This transition will cause a definite value of absorption cross section and hence the XAS peak will be observed.

2.3.2.1 Dipole selection rule

The transition from initial state (ψ_i) to final state (ψ_f) occurs only when the transitions are dipole allowed with appropriate photon energy. In the equation 2.15 the dipole moment operator follows the dipole selection rule and when this rule is followed then only there will be absorption. Hence the dipole selection rules for allowed excitation are given as bellow:

i. Change in orbital angular momentum quantum number; $\Delta l = \pm1$
ii. Change in magnetic quantum number ; $\Delta m_l = 0, \pm1$
iii. Change in spin quantum number ; $\Delta m_s = 0$
iv. Change in total angular momentum ; $\Delta j = 0, \pm1$

The above mention selection rule can be applied to the single electron excitation process. For many electron processes the selection rule can be described taking the summation of individual quantum numbers. The total orbital angular momentum of the atomic system can be gives as the summation over the orbital angular momentum of electron ($\vec{L} = \sum_i \vec{l_i}$) and on the other hand the total spin quantum number can be given as summation over the spin quantum number of each electrons ($\vec{S} = \sum_i \vec{s_i}$). The total angular momentum is represented by J, but the total angular momentum can be defined in two different ways depending on the number of electrons in the atom.

For the light elements the total angular momentum of an atom can be given by the Russell-Saunders (L-S) coupling. The total angular momentum of an atom is the vector sum of the total orbital momentum and the total spin angular momentum, i.e. ($\vec{J} = \vec{L} + \vec{S}$). The value of J ranges from |L-S| to |L+S|.

To determine the total angular momentum for heavy element the L-S coupling is not valid for transition of electron core level to unoccupied level. In this case the spin-orbit interaction in individual electron is stronger than the spin-spin or orbital-orbital interaction of individual electrons. So to get the total angular momentum, *j-j* coupling is followed and is given by summation over the individual angular momentum (*l*) and spin momentum (s), i.e., ($J = \sum_i j_i = \sum_i l_i + S_i$) .

The quantum number of an atom with multiple electrons can be represented by the total spin quantum number S, angular momentum number L, total angular momentum J and the primary quantum number is n. The spectroscopic notation of an atom is given by quantum number $^{2S+1}L_J$.

For multiple electron transition the dipole selection rule is given as bellow:

i. Change in orbital angular momentum; $\Delta L = 0, \pm 1$
ii. L= 0↔0 is not allowed (S orbital to S orbital transition is not allowed)
iii. Change in spin quantum number ; $\Delta S = 0$
iv. Change in total angular momentum ; $\Delta J = 0, \pm 1$
v. J= 0↔0 transition is not allowed

The dipole operator has an odd parity and the parity also changes with an electric dipole transition. So for the allowed transition the parity of the wave function must change.

2.3.2.2 X-ray linear dichroism

The absorption of polarized light is dipole dependent. This means that the absorption of X-ray is different in different orientation of the dipoles in the materials. The equation 2.15 shows that the intensity of the absorption depends on dipole moment operator and this defines the polarization of the transition according to the relation

$$P = P_x + P_y + P_z = \sum_i e_i x_i + \sum_i e_i y_i + \sum_i e_i z_i \tag{2.17}$$

Where P_x, P_y, and P_z are the electric dipole moment operators along x, y, and z directions respectively. The constant e_i represents the charge on the i^{th} particle and x_i, y_i and z_i are the Cartesian coordinates.

The intensity of the X-ray absorption (dipole allowed transition) is the dot product of the incident electromagnetic wave (photon) and the transition dipole moment (94) and is given as bellow;

$$I \propto |E \cdot P_{if}|^2 = |E|^2 \, |P_{if}|^2 \, cos^2\theta \tag{2.18}$$

$$\text{Or } I = A \, cos^2\theta \tag{2.19}$$

Where E is the polarization of the electric field vector of electromagnetic wave (photon) and θ is the angle between electric dipole moment and the E.

Linear dichroism is the difference in absorption of horizontally polarized light ($I_{\parallel}$) and vertically polarized light ($I_{\perp}$). The X-ray linear dichroism (XLD) can be given as bellow

$$XLD = \frac{I_{\parallel} - I_{\perp}}{I_{\parallel} + I_{\perp}} \tag{2.20}$$

2.3.3 Resonant photoelectron spectroscopy (res-PES)

The X-ray absorption spectra (XAS) can be represented by the resonance photoelectron spectra with resolved energy of absorption. The XAS can be resolved into number of spectra scanned with different photon energy at resonance energy range collected over the valence band region.

At the resonance energy the elemental cross section for X-ray absorption increases and hence the number of emitted photoelectron for the element with resonating to the incident energy increases. So PES for a particular element has several order higher magnitude than the other elements in the same material at resonance energy. Generally the res-PES is taken over the VB region and due to the higher absorption cross section for particular element the PES has higher intensity at a define photon energy in the VB spectra. The res-PES is able to identify the contribution of each element to the VB of the materials and hence it enables to find the contribution of different elements in partial density of states (pDOS) at occupied states (valence band states). On the other hand, VB spectra taken with different photon energy of a core level absorption edge are summed up to define the conduction band. The XAS spectra at a certain absorption edge of the element can be considered as the partial density of states in the conduction band due to that element.

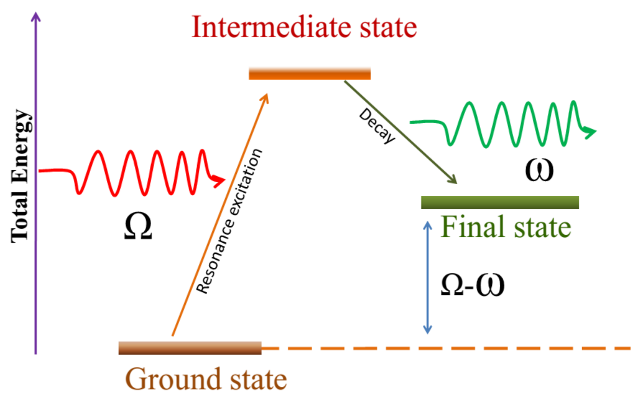

Figure 12: Schematic representation of Kramer-Heisenberg mechanism with ground, intermediate and final states presenting both excitation and de-excitation processes. The diagram is reproduced from **(95)**.

The res-PES is a second order photo electrical process consisting of excitation and de-excitation of electron upon photon incident. In the excitation process the core electron is excited to transfer into an intermediate state and there after the electron at the intermediate state decays with emission of electrons via Auger process to the final state as shown in Figure 12. The excitation and de-excitation processes can be described by second order quantum formula known as Kramers-Heisenberg formula (95).

In the process of res-PES the electron from the ground state $|g\rangle$ is excited into the intermediate state $\langle i|$ and the intensity of this transition is determined by the transition operator T_1. The full width of the resonance will determine the lifetime (Γ_i) of the intermediate state. The excited intermediate state $|i\rangle$ will decay through the photoemission process into the final state $\langle f|$ and the transition intensity will be given by the transition operator T_2. Since the final transition is the photoemission process the transition operator T_2 describes the resonant Auger decay process.

In this two steps process the emitted electron intensity will be the function of X-ray energy Ω and emitted photoelectron energy ω as well as energy $E_{g,i,f}$ (energy of ground, intermediate and final states) is given by Kramers-Heisenberg relation:

$$F(\Omega,\omega) = \sum_f \left|\sum_i \frac{\langle f|T_2|i\rangle\langle i|T_1|g\rangle}{E_g-E_i+\Omega-i\frac{\Gamma_i^2}{2}}\right|^2 \times \frac{\frac{\Gamma_f}{2\pi}}{(E_g-E_f+\Omega-\omega)^2+\frac{\Gamma_f^2}{4}} \tag{2.22}$$

The interference of the intermediate states that decay to the same final state can change the intensity of the decay but not the energy position, hence the equation 2.22 can be further simplified by ignoring the interference effect:

$$F(\Omega,\omega) = \sum_f \sum_i \frac{\langle f|T_2|i\rangle^2\langle i|T_1|g\rangle^2}{(E_g-E_i+\Omega)^2+\frac{\Gamma_i^2}{2}} \times \frac{\frac{\Gamma_f}{2\pi}}{(E_g-E_f+\Omega-\omega)^2+\frac{\Gamma_f^2}{4}} \tag{2.23}$$

2.3.3.1 De-excited process (decay of intermediate states)

The res-PES process is accompanied by one excitation process from ground state to the intermediate state and a de-excitation process intermediate state to the final state. The de-excitation process is more helpful to determine the lifetime, bonding hybridization and the arrangements of chemical bonding in the material. But the decay process can lead to the emission of photon and or emission of photoelectrons due to Auger decay.

The excitation process leaves behind core hole in the sub-shell of the atom, and the core hole can be filled by the electron from the next higher sub-shells. The filling of the core hole by the electron from the higher sub-shell will result in emission of photon due to the energy differences as shown in Figure 13 (a). On the other hand there is also possibility that the energy of due to the filling of core hole can be transfer to the valance state electron and will cause the emission of photoelectrons in the form of an Auger electron as shown in Figure 13(b).

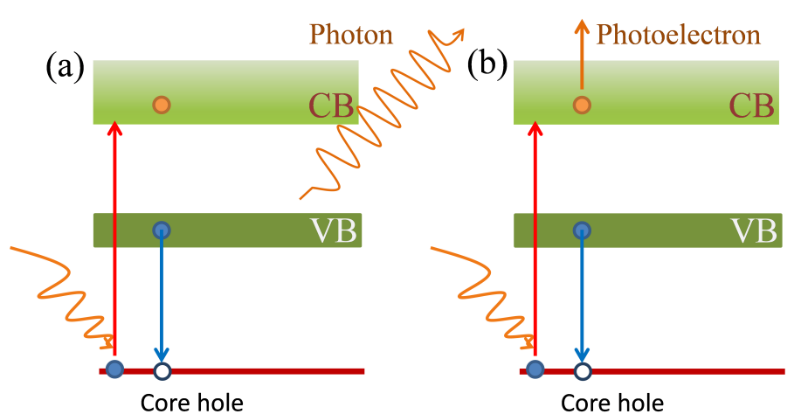

Figure 13: Schematic diagram of the de-excitation process showing two possible way of decay result, emission of photon (a) and emission of Auger electrons (b).

The photoemission process due to the core hole filling has to follow the dipole selection rule since this is an optical phenomenon. But when the core hole filling results in emission of photoelectron the Columbic operator becomes more important than that of the dipole moment operator. Hence the Auger decay process does not need to follow the dipole selection rule. The Auger decay can occur through spectator or participator or spectator and participator processes.

The above mentioned two final processes (photoemission and photoelectron emission) depend on the atomic number of the element (96). For the element below the atomic number 15 the Auger decay process is dominating and with the increase in atomic number the photoemission process increases. For elements with atomic number higher than 60 the photoemission process becomes dominating.

A part of this thesis work is dealing with the non radiative decay mechanism of TiO_2 in res-PES measurements. So in the present part of this chapter different Auger decay mechanism will be discussed.

2.3.3.2 Auger decay process

The core hole generated by core ionization or core-excitation is not in equilibrium energetically. The average life time of this kind of core hole is only few femtoseconds and hence the core hole decay quickly. The core hole is filled by the electron from the next higher sub shell and the extra amount of energy is transferred to another electron, subsequently the electron is knocked out from the orbital. This emitted electron is known as the Auger electron. The final state after the Auger decay is a two hole stable state. The Auger electron has a constant kinetic energy, therefore the binding energy is photon energy dependent and the kinetic energy (K.E) is given by

$$E_{K,Auger} = h\upsilon - E_{B,2h}, \tag{2.24}$$

where $E_{K,Auger}$, $E_{B,2h}$ and $h\nu$ are the kinetic energy of Auger electron, binding energy of the two holes final state and the incident energy.

For example, when a core hole for 1s (K-shell) level is formed by photoemission, then an electron from the 2p (L-shell) will fill the core hole and another electron from the 2p will be emitted as an Auger electron. This Auger transition will be named as $KL_{2,3}L_{2,3}$ Auger.

At non resonance energy excitation there can be other two decay processes namely Coster-Kronig (CK) and super Coster-Kronig (sCK) can also exist (97). In the CK Auger decay the core hole is filled by the next sub shell with same principal quantum number. When a core hole is created in L shell and the electron from the L shell fills the core hole emitting an electron from the M shell than the Auger transition is $L_2L_3M_{4,5}$ CK Auger decay. The ionization energy of the M shell electron must be less than the transferred energy from L_3 to L_2 than only the CK Auger decay would be possible. The CK Auger process is very fast compare to the normal Auger decay in 3d metals for L_2 shell and hence is dominating phenomena in de-excitation process (98). But due to the low kinetic energy the CK Auger peak is not clear detectable as it has the same intensity of the back ground.

In the super Coster-Kronig, the participating electrons filling the core hole and the emitted electrons have same principal quantum number. This means that the sCK Auger decay occurs inside a single shell.

The de-excitation process in case of resonant photoelectron spectroscopy is more complex than the non resonant one. The Auger process involved in res-PES is discussed here.

Upon resonant excitation the core electron excited into the intermediate unstable state and the transition for a 3d element can be written as bellow:

$$[2p^6 3d^n] + \hbar\omega \rightarrow [2p^5 3d^{(n+1)*}] \quad (2.25)$$

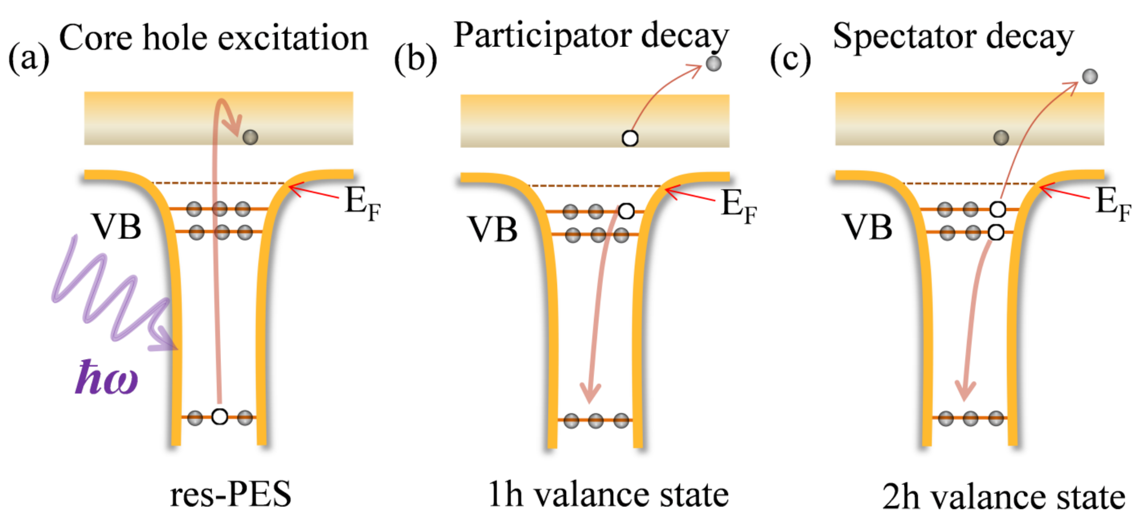

Figure 14: Schematic diagram of res-PES process (a) and the decay process via participator decay (b) and spectator decay (c).

The core hole will decay when the excited electron from the intermediate state will fill the core hole and as a consequence the decay process leaving behind single valence hole. The electron from the valence state will be emitted as a photoelectron and this process is known as spectator decay and is shown schematically in Figure 14(b). The intermediate decay process of participator decay can be given by the equation 2.26:

$$\left[2p^5 3d^{(n+1)*}\right] \rightarrow \left[2p^6 3d^{(n-1)}\right] + e^- \tag{2.26}$$

$$[2p^6 3d^n] + \hbar\omega \rightarrow \left[2p^6 3d^{(n-1)}\right] + e^- \tag{2.27}$$

The participator decay is like the normal photoemission and hence the kinetic energy of the emitted electron depends on the excited photon energy. The participator decay is accompanied by a one valence hole.

In another possible decay mechanism the core will be filled by the valence electron and another electron from the valence will be emitted as Auger process as shown in Figure 10(c). The electron emitted by this process is the spectator electrons and the Auger decay is the spectator Auger decay. The spectator decay can be expressed as in the equation 2.28.

$$[2p^6 3d^n] + \hbar\omega \rightarrow \left[2p^5 3d^{(n+1)*}\right] \rightarrow \left[2p^6 3d^{((n-2)+1)*}\right] + e^- \tag{2.28}$$

In spectator Auger decay the kinetic energy of the electron depends on the energy difference between the core level and the refilling electron. Hence the kinetic energy in this case is constant and is independent of excitation energy.

Different Auger decay transitions have different lifetimes. The life time of participator Auger decay is faster (τ = 500 fs) than spectator auger decay (τ = 1 fs). The involvement of two electrons in participator decay process makes it faster than the spectator decay. The lifetime and final hole state of the different Auger processes is given in the Table 4.

Table 4: Lifetime and final state hole of different decay processes.

Process	Final state hole	Lifetime (τ)	References
Excitation	-	<1 as	
Participator	1h	500 as	
Spectator	2h	1 fs	(99)
Croster-Kronig	2h	<spectator	
Super Coster-Kronig	2h	1/10 Coster Kronig	
Core hole	-	<6 fs	(100)

2.3.3.3 Measurement and Study of res-PES

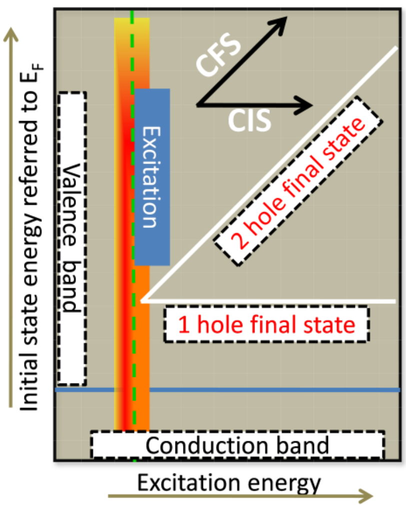

Figure 15: Schematic diagram of res-PES measurement. The X-axis is the excitation energy that represents the conduction band and the Y-axis the initials state energy (valence band). The vertical red region is the resonantly excited states (exciton). The intensity along the horizontal line is the participator auger decay (1 hole final state) and the intensity making an angle 45° with the horizontal is the spectator Auger decay (2 holes final state). The CIS and CFS can be obtained from res-PES by taking the cut along the constant binding energy and kinetic energy, respectively.

The res-PES measurement is equivalent to the normal photoelectron spectroscopy. In res-PES measurement a number of PES are taken across the valence band region with the photon energy around the absorption edge of the desired element. The monochromator connected to the controller automatically switch the photon energy by steps in energy. At each photon energy, the VB spectra are collected and then the photon energy changes after VB spectra. This cycle is continued for a range of photon energies along the absorption edge. The data collected for res-PES measurement are transferred to a matrix of data with X-axis as function of photon energy and Y-axis as binding energy of the VB by using the script written by Matthias et al. (101). The intensity of the photoelectrons are given in the color code in the logarithmic scale and the brightness of the point in res-PES related to the intensity. Figure 15 shows a schematic representation of the res-PES measurement. From the single res-PES measurement several information, such as content initial state (CIS), constant final state (CFS), and XAS can be obtained. The Auger decay profile can also be detected from the intensity in the res-PES measurements. The one hole final state corresponding to the participator decay has constant binding energy and is marked as zero degree with the X-axis. On the other hand the two holes final state (spectator decay) has the constant kinetic energy and this is observed at an angle of 45º to the photon energy axis. The integration of the res-PES along the energy will give rise to the XAS of the element at that edge.

2.3.3.4 Charge neutrality level (CNL)

The band alignment of semiconductors or semiconductor-metal depends on the interfacial state of the materials and hence also changes the electronic properties of the material overall. At the interface of metal-semiconductor a defect state is formed known as metal induced gap state (MIGS) and in semiconductor-semiconductor interface the defect state is the virtual gap states (ViGS) (102). The MIGS or ViGS have the branch points which change the charge density of the valence band of semiconductor. The net charge in the MIGS or ViGS depends on the position of the Fermi level with respect to the branch points. When the Fermi level is below, equal or above the branch point the charge of the MIGS is positive, zero or negative respectively. So the branch points are the levels that neutralize the charges at the inter face and hence called as charge neutrality level (CNL). The CNL play the role of and effective Fermi level at the interface of metal-semiconductor or semiconductor-semiconductor. The CNL is used to define the metal-semiconductor or semiconductor-semiconductor interface. In case of metal-semiconductor interface the CNL are pinned at the interface. On the other hand the interface of the semiconductors can be defined by aligning the CNL of each semiconductor. Unlike Fermi level the CNL of semiconductor does not change at the interface and it is an intrinsic property of the semiconductor.

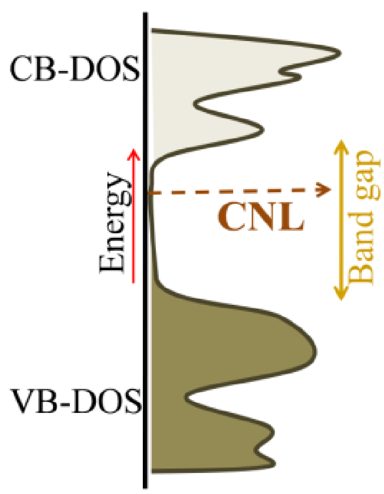

Figure 16: Schematic diagram showing the DOS of VB (dark shaded region), CB (lightly shaded region) and the determined CNL from VB and CB.

The averaged band structure of the Brillouin zone Greens function equaling to zero gives the CNL of the semiconductor [(103), (104)]. In other words the CNL is the averaged weight of the density of states in occupied and unoccupied states. This means the CNL is the mid gap of the bonding and anti bonding sates. Schematic representation of the CNL is given in Figure 16 where the CNL lies in the middle of the weight of the DOS in valence band and conduction band. It can be given as equation 2.29:

$$E_{CNL} = \frac{N_1 E_2 + N_2 E_1}{N_1 + N_2}, \tag{2.29}$$

where N_1 is the number of states at valence band energy E_1 and N_2 is the number of states in conduction band energy E_2.

2.3.4 Photoelectrochemical measurements

The photoelectrochemical measurements are performed using a VERSSTAT 4 potentiostat. A single compartment bottom cell made up of Tafelon is used to characterize the photoeletrodes. The Si, TiO_2/Si and TiO_2 coated Si micro pillars (SiMPs) are used working electrode (photoelectrodes). The back contacts of photoelectrodes are made by carefully removing the SiO_2 layer on the back and using InGa eutectic to form Ohmic contact. The Ag/AgCl electrode with 3M KCl is used as the reference electrode while that of Pt foil is used as counter electrode in the photoelectrochemical system. The potentials during the measurements are applied with respect to the Ag/AgCl reference electrode and then potential is converted into reverse hydrogen electrode (RHE) applying the equation 2.30.

$$E_{RHE} = E_{AgCl} + 0.059\,pH + E^0{}_{AgCl} \tag{2.30}$$

Where, $E^0{}_{AgCl}$= 0.197 V, E_{RHE} is the equivalent reverse hydrogen electrode potential, E_{AgCl} is the applied potential with respect to the Ag/AgCl electrode.

The photoelectrodes are tested by three electrochemical methods; cyclic voltammetry (CV), linear scan voltammetry (LSV) and the chronoamperometry. The CV and LSV are used to test the photoelectrochemical activity of the photoelectrodes while the chronoamperometry test is used to check the photocatalytic stability of the photoelectrodes. The scanning rate of 50 mV/s was used for the cyclic voltammetry and linear scan voltammetry experiments. The areas of working electrodes are always kept constant and are 0.38 cm^2. The current collected are normalized to the illumination area of the photoelectrodes to determine the current density. The 0.5 M phosphate buffer solutions of pH 7 and 0.1 M H_2SO_4 of pH 1 are employed to study the properties of the photocathode. The used electrolytes were purged for about 20 min. with N_2 in order to minimalized the oxygen gas content.

For the photoelctrochemical studies a tungsten lamp (Euromax fiber optic light source EK1) with light intensity of 40 $mWcm^{-2}$ at wavelength of 610 nm was used. The intensity of the lamp was always adjusted with a solar cell. The absorption of the light due to the electrolyte is neglected here.

Chapter 3

RESULTS AND DISCUSSION

In this chapter results regarding the deposition of TiO_2 films by ALD and their electronic properties studied by X-ray photoelectron spectroscopy are presented. This chapter is divided into three sub chapters depending on the results.

The first section of this chapter is dedicated to the detailed analysis of the growth of TiO_2 by the ALD technique using X-ray photoelectron spectroscopy. This mainly deals with the growth process of TiO_2 by ALD, the effect of growth parameters such as temperature, pressure, and the type of ALD processing, i.e. thermal and plasma.

In the second chapter the electronic properties of thin TiO_2 films grown by ALD are studied using synchrotron radiation and laboratory based X-ray spectroscopy. This is followed by the study of dichroism in TiO_2 ALD films by X-ray linear dichroism experiments.

The final section of this chapter deals with the application of TiO_2 film as a protecting layer for photoelectrodes used for photocatalytic water splitting. The PES is used to determine the role of protecting layer against photo corrosion.

3.1 Deposition of TiO_2 by ALD

The titanium dioxide is deposited using two non-corrosive and halide free precursors namely titanium tetra isopropoxide $Ti\{OCH(CH_3)_2\}_4$ (TTIP) and titanium tetra methoxide $Ti(OCH_3)_4$ (TiOMe) as source of Titanium in the ALD process. The melting point of TTIP is 17 °C and hence this precursor can have high vapor pressure at room temperature. On the other hand the TiOMe is a solid at room temperature (melting point is 200 °C). In both cases, H_2O is used as the source of oxygen. In the early stage of investigation, to get the standard films of TiO_2 by ALD, both depositions are carried out at only one temperature for each precursor used. A laboratory made ALD system is used to grow the TiO_2 and the base pressure of the system is kept at 10^{-6}mbar. The growth parameters are given in the Table 5.

Table 5: The growth parameters used in deposition of TiO_2 using TTIP and TiOMe in the ALD system.

Precursors	Precursor temp.	Chamber temp.	Precursor pulse time (s)	H_2O pulse time (s)	Time between two pulses (s)	Substrate temp.
TTIP	Room temp.	100 °C	4	0.5	15	250 °C
TiOMe	180 °C	100 °C	6	0.5	30	300 °C

The substrate temperature and the time interval between two pulses are different for each precursor. The substrate temperature for TTIP and TiOMe are 250 °C and 300 °C respectively. The growth temperature chosen here are the temperature region where the growth rate per cycle is constant for TTIP and TiOMe [(105), (106)]. The growth temperatures are well below the decomposition temperature 325 °C and 350 °C for TTIP and TiOMe respectively [(107), (106)] The time interval in the case of TiOMe (30 s) is higher than in the case of TTIP (15 s) in order to get the appropriate vapor pressure during deposition due to the fact that TiOMe is a solid precursor.

The mechanism of deposition of TiO_2 using metal alkoxide depends on the operating temperature for the deposition. In case of TTIP the reaction byproducts can be different species such as C_3H_6(g), $(CH_3)_2CHOH$ (g), CH_3COCH_3(g) and $((CH_3)_2CH)_2O$(g) in different ranges of the operating temperatures [(108). When the substrate temperature is above 347 °C the byproducts propane and hydrogen hinder the ALD process by removing the adsorption sites for self-limited growth (105). In the present experiment the deposition temperature chosen is 250 °C and at this temperature the growth mechanism can be described using the equation 3.1.

$$\mathrm{Ti(OCH(CH_3)_2)_4(g) + 2H_2O \rightarrow TiO_2 + 4(CH_3)_2CHOH(g)} \tag{3.1}$$

The solid precursor titanium tetra methoxide is the most table metal alkoxide used for deposition of TiO_2. Pore et al. (106) showed that the composition of the film is consisting of H:C in the ratio of 3:1 in the deposition temperature range of 200 °C to 350 °C. So the reaction mechanism for the deposition of TiO_2 using TiOMe can be described by the equation 3.2.

$$\mathrm{Ti(OCH_3)_4(g) + 2H_2O \rightarrow TiO_2 + 4\,CH_3OH} \tag{3.2}$$

The samples are grown in an in-situ ALD system at the U49/2-PGM beam line at BESSY-II, Berlin. The substrate temperature is maintained constant by placing the samples on a ceramic heater and the samples are kept for 10mins on the heating plate to realize equilibrium in temperature throughout the sample. After the deposition, the sample is transferred to the measuring chamber only after the base pressure of ALD chamber reaches 10^{-7} mbar, since the chamber is attached directly on the experimental chamber of PES experiments. The samples are irradiated with the X-rays having energy of 640 eV and the photoelectrons are collected with the hemispherical analyzer as explained in the experimental part (see chapter 2.2.2 Experimental setup at synchrotron). The data are collected with the pass energy of 20eV and with the scan rate of 0.1eV s^{-1}.

Two sets of samples are grown and characterized with in-situ XPS. A first sample set is grown using the TiOMe precursor for 10, 40, 100 and 200 ALD cycles. In another sample set TTIP precursor is used and the samples are grown for 50, 100, 150 and 200 ALD cycles. The growth parameters are given in Table 5.

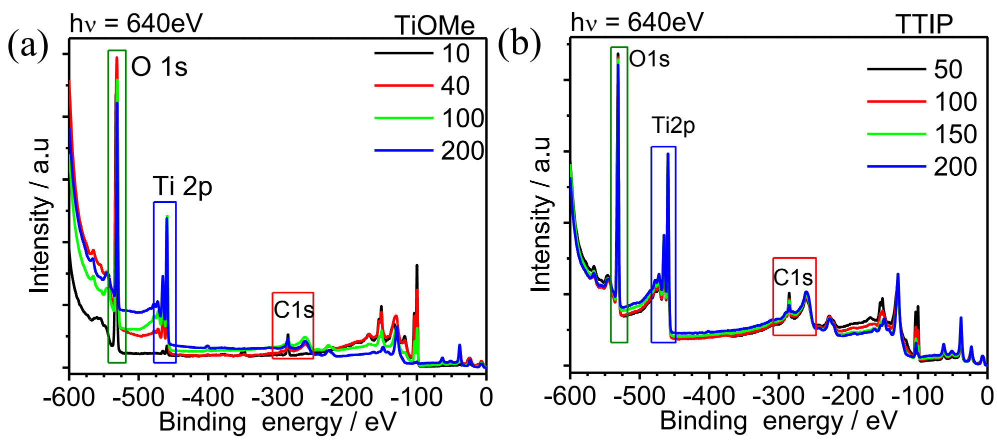

Figure 17: Overview spectra of TiO_2 deposited on Si/SiO_2 using TiOMe(a) and TTIP (b) recorded at 640 eV photon energy. The numbers in the labeling presents the number of ALD cycles. The red boxes in the plots show the position of C1s while blue and green boxes indicate the Ti2p and O1s respectively.

The quality of the film is of primary importance for study of fundamental properties of the material as well as its application in various fields. In the vapor deposition techniques using metal alkoxides, the films are mainly contaminated with carbon. Depending on the deposition conditions the amount of carbon in the film varies and it also affects the quality and properties of metal oxide films. The carbon contamination of the TiO_2 films deposited in this work is investigated by using the C1s region in the PES survey spectra. In Figure 17 the PES survey spectra of TiO_2 ALD films after different ALD cycles using TiOMe (Figure 17(a)) and TTIP (b) are shown. The peak at 285 eV (marked with red boxes) corresponds to the C1s contribution. The C1s intensity of TiO_2 films prepared by in-situ ALD is very less compared to the Ti2p (blue boxes) and O1s (green boxes) intensities. Moreover, the in-situ facility to measure XPS allows the measurement of the sample without contamination from outside. Therefore the carbon peak is due to the amount of carbon present in the sample. The intensity is a measure of the amount of elemental carbon within the material and here the lower intensity of the C1s peak suggests that the samples contain lower amount of carbon in them.

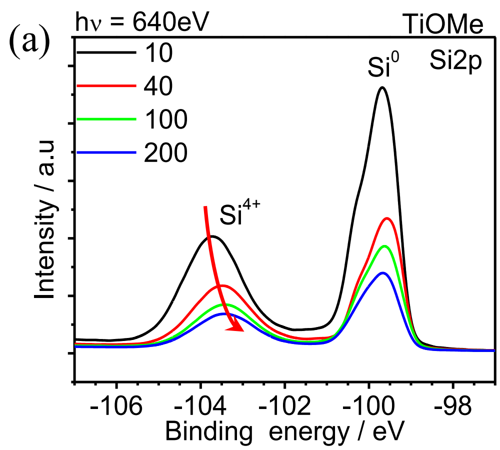

Figure 18: Photoelectron spectra of Si2p taken after deposition of TiO_2 using titanium tetra methoxide (a) and titanium tetra isopropoxide. These data are collected with the incident photon energy of 640eV at synchrotron radiation. The numbers in the labeling represent the number of ALD cycles used to grow TiO_2.

The XPS spectra of Si2p peak are shown in Figure 18 for TiO_2 grown using TiOMe (a) and TTIP (b). The peak at 99.5 eV corresponds to elemental Si where as the peak at higher energy of 103.7eV corresponds to the Si^{4+} states. The Si^{4+} is due to the presence of native oxide on the Si surface. In Figure 18 the peak intensities at 99.5 and 103.7 eV both are attenuated after each deposition cycles.

In Figure 18(a), it's visible that the decrease in peak intensity at 99.5 eV is nto linear with the number of cycles. It decreases sharply from 20 to 40 ALD cycles. In contrast, the change in intensity of the peak from 100 to 200 ALD cycles is less compared to the change from 10 to 40 ALD cycles. Nevertheless, the attenuation of intensity of Si2p peak with the number of ALD cycles confirms the deposition of TiO_2 by ALD using TiOMe. The attenuation of the Si2p peak intensity can be used to determine the thickness of the over-layer on Si.

The Si2p spectra after the deposition of TiO_2 using TTIP are shown in Figure 18(b). The attenuation of Si2p from the deposition can be observed by comparing the intensity after 50 cycles and 100 ALD cycles. The decrease in intensity from 50 to 200 ALD cycles is linear with the increasing cycle number. The linear decrease in the intensity is due to the increased thickness of TiO_2 by ALD growth.

In Figure 18 (a,b) the Si 2p peaks shift towards lower binding energy after deposition of TiO_2. The shift in binding energy of Si2p is due to the final state effect of emitted photoelectron when the Si is covered with metal oxide [(109), (110)]. The attenuation and the shift in peak position of Si2p confirms the deposition of TiO_2 using these two precursors. The XPS peak intensity of the under-layer material can be used to determine the thickness of the over-layer using equation 2.13. In the table below the determined thicknesses of the TiO_2 layer deposited using two precursors are given.

Table 6: Determination of thickness of deposited TiO_2 layer in dependence of the ALD cycle number for TiOMe and TTIP precursors.

ALD Cycles	Thickness of TiO_2 (nm) using TiOMe	ALD Cycles	Thickness of TiO_2 (nm) using TTIP
10	0.2	50	0.75
40	0.8	100	1.5
100	1.05	150	2.25
200	1.38	200	3.0

The Table 6 shows, that in case of TiOMe precursor the growth rate per cycle (GPC) is 0.02nm for the first 40 cycles. In the subsequent cycles the growth rate goes lower, for instance the GPC from 40 and 100 cycles is 0.005nm GPC which is far below the first 40 cycles. On the other hand the GPC is constant through the number of cycles for the TTIP precursor. Here the GPC is constantly 0.015 nm in the investigated cycle number range. The overall GPC for TiOMe is 0.006 nm and for TTIP it is 0.015 nm. The growth rate in case of TiOMe could be due to its lower vapor pressure as compared to the TTIP which has the highest vapor pressure among the titanium alkoxides (105).

In the previous works about the deposition of TiO_2 using TiOMe, the GPC is found to be 0.04 nm/cycles (111) and the present study shows a much lower growth rate. The ALD system used for the present experiments is home-built and dedicated to liquid/vapor based precursor. In the present study with the TiOMe the generation of vapor pressure was low so the growth rate is quite low compared to the literature data. For the TTIP precursor the growth rate per cycles is 0.015 nm at the substrate temperature of 250°C and this GPC is close to the literature value (0.03 nm) of TiO_2 growth rate using this precursor (105). In the literature there are some contradictory result regarding the GPC of TiO_2 using TTIP in the different temperature ranges. Doring et al. found that the growth rate of TiO_2 film is 0.15 nm/cycle at 150 °C (112). Later the literatures show more consistent values on the growth rate of TiO_2 using the precursor TTIP. In the temperature range 200-250 °C the GPC was found to be 0.05-0.06 nm/ cycles (113) and 0.068 nm/ cycle at the substrate temperature 150 °C (114).

Figure 19 shows the O1s spectra of TiO_2 on Si substrate deposited using TiOMe and TTIP by ALD method. In Figure 19 (a) and (b) the O1s peak is consisting of two peaks at 532.4 and 530.7 eV. The peak at 532.4 eV is the O1s peak signal from the substrate Si with native SiO_2; whereas the peak at lower binding energy at 530.7 eV corresponds to the O1s from the deposited TiO_2. The intensity of the peak at 532.4 eV decreases with the increase in ALD cycles. This decrease is faster in case of the TTIP precursor than in case of the TiOMe. After 200 ALD cycles the peak at higher binding energy (Si substrate related) is still visible for the TiOMe precursor but for TTIP it is not clearly visible and has only a small shoulder. For both the precursor the shift in the binding energy of the O1s towards the lower binding energy confirms the deposition of TiO_2, whereas the decrease in intensity of the peak at higher binding energy shows the deposition rate. The O1s spectra of TiO_2 on Si substrate are in agreement with the Si2p spectroscopic data in Figure 18.

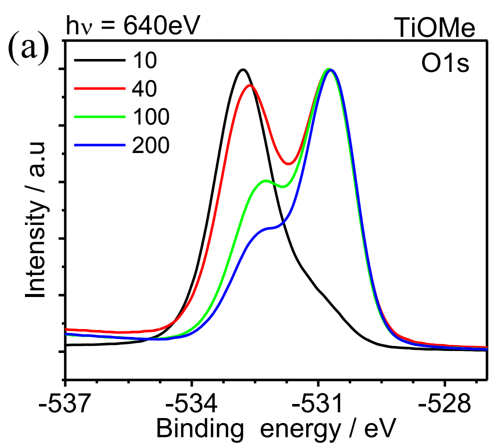

Figure 19: Photoelectron spectra of O1s taken after deposition of TiO_2 using titanium tetra methoxide (a) and titanium tetra isopropoxide. These data are collected with the incident photon energy of 640 eV at synchrotron radiation. The numbers in the leveling represents the number of ALD cycles used to grow TiO_2.

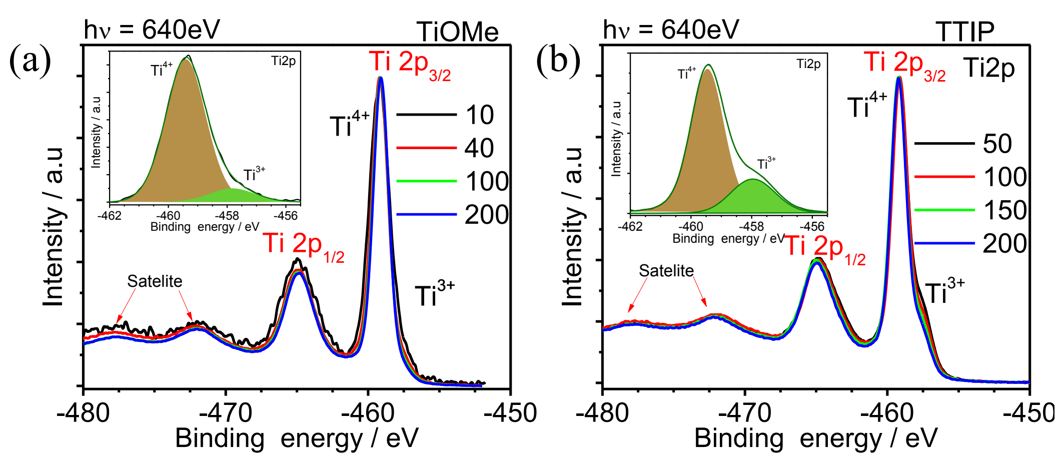

Figure 20: Ti2p spectra of TiO_2 deposited on Si/SiO_2 using TiOMe (a) and TTIP (b) by ALD method. The spectra are recorded after different ALD cycle numbers as labeled in the legend. In the inset of these figures the deconvolution of Ti^{4+} and Ti^{3+} states of Ti2p at $Ti2p_{3/2}$ edge are shown.

Titanium can stay in two oxidation states, Ti^{3+} and Ti^{4+}, forming Ti_2O_3 and TiO_2 respectively. The aim of the deposition is to form the pure TiO_2 without contamination and Ti^{3+} states. The PES of Ti2p can be used to examine the quality of the TiO_2 deposited by ALD using these two precursors. Figure 20 (a) and (b) show the Ti2p spectra for samples grown with TiOMe and TTIP respectively. The spectra are normalized to 1 at highest intensity and zero at lowest intensity. The spectra here cannot be used for the quantitative determination of TiO_2 on Si/SiO_2 substrate. The main peak at 459.2eV corresponds to the Ti2p with Ti^{4+} oxidation states. The highest peak intensity at 459.2 eV is due to the deposition of TiO_2 on Si. But under careful analysis it can be seen that the peak at the $Ti2p_{3/2}$ edge has a tail towards lower binding energy. This peak can be deconvoluted into two peaks as shown in the inset of Figure 20 (a) and (b). The fitting of the curves are done using the Fityk software (115). The peak at lower binding energy refers to the Ti^{3+} oxidation states and the higher binging energy peak is for Ti^{4+} states. The ratio of the Ti^{3+} to Ti^{4+} is tabulated in the Table **7**. The lower ratio of Ti^{3+}:Ti^{4+} indicates that the material deposited is mainly consisting of TiO_2 rather than Ti_2O_3.The Ti2p spectra are consisting of 3 more peaks; where the peak at 464.8 eV corresponds to $Ti2p_{1/2}$ while two satellite peaks at 472.2 and 477.8 eV can be observed.

Table 7: Ti^{3+} to Ti^{4+} ratio for TiO_2 deposited by ALD with TiOMe and TTIP. The determination is done using the fityk software to fit the Ti2p curve into two curves at the $Ti2p_{3/2}$ edge into two curves for Ti^{4+} and Ti^{3+} oxidation states.

ALD Cycles	Ti^{3+}:Ti^{4+} (TiOMe)	ALD Cycles	Ti^{3+}:Ti^{4+} (TTIP)
10	0.109	50	0.142
40	0.050	100	0.120
100	0.044	150	0.126
200	0.043	200	0.116

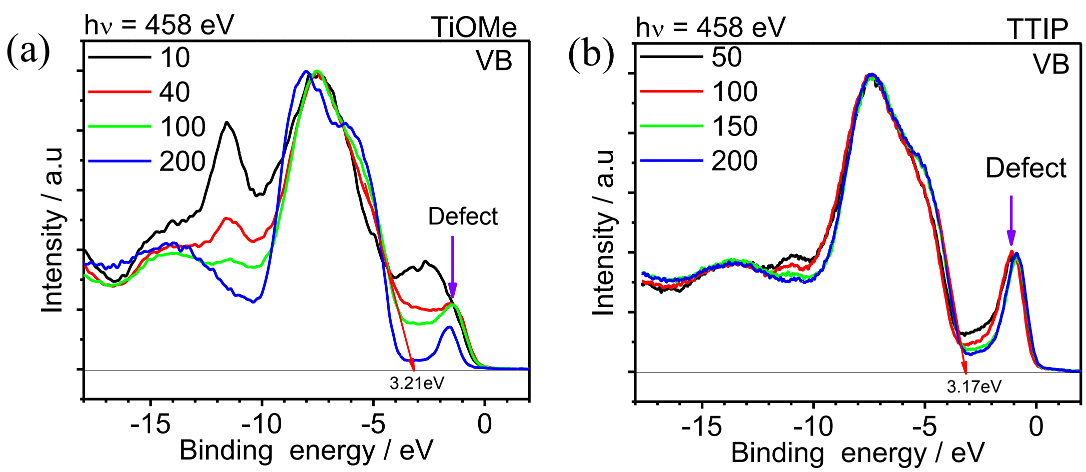

Figure 21: The valence band spectra measured with 458 eV photon energy for TiO_2 deposited for different ALD cycles as labeled using both the precursors TiOMe (a) and TTIP (b).

The low photon energy 458 eV is used to collect the valence band spectra of theTiO_2 films (Figure 21). Since the films are very thin the lower photon energy is used to get the information mostly from the surface rather than from the bulk (substrate). All the valence band spectra are normalized to one at 8 eV for better comparison of the spectra from different samples. In the VB spectra of 10 ALD cycles with

TiOMe the broad peak at that energy starts from zero binding energy and extends into the VB. This is due to the very thin film of TiO_2 and the signal is from the Si/SiO_2 substrate. With the increase in number of cycles the peak broadening decreases. On the other hand after 50 cycles of ALD with TTIP the VB of Si is not visible. The photoelectron spectra of all the elements such as Si2p, Ti2p and O1s are in good agreement that the growth rate in case of TTIP precursor is higher than in case of the TiOMe precursor.

The position of the valence band maximum is obtained by extrapolating the slope of the spectra to zero intensity. The VBM positions are found to be 3.21 and 3.17 eV for TiOMe and TTIP deposited TiO_2 films respectively. The TiO_2 films grown by TiOMe and TTIP have a state in the gap at binding energy around 1 eV below the Fermi level and generally this state is addressed to defect states. The defect states start right after the Fermi level and have a width of 2 eV. The origin of the defect state in TiO_2 is due to Ti3d states within the band gap (3), but there is also a debate on the origin of the defect states of TiO_2 in the literature. It is also believed that the defect state can arise due to oxygen vacancies in the TiO_2 lattice (116).

The photoelectron spectroscopy can be use to investigate the elemental ratio in the material. Combining the core level spectra of Ti2p, and O1s the elemental ratio in the grown TiO_2 films can be determined. The stoichiometry of grown TiO_2 films can be determined using the equation 2.9.

$$\frac{A}{B} = \frac{I_A/S_A}{I_B/S_B}, \tag{2.9}$$

where I_A is the intensity of Ti2p and I_B is the intensity of O1s.

S_A and S_B are the atomic sensitivity factors of Ti2p and O1s respectively but in this case we consider the sub-shell photo ionization cross-section since all other parameters are close to each other for these elements. The intensity of the core level spectra depends on the sub-shell photo ionization cross-section. In the present case the ionization cross-section for Ti2p and O1s are 1.202 Mb and 0.4119 Mb respectively [(93)]. The stoichiometry (O:Ti) of TiO_2 prepared by ALD with TiOMe and TTIP is given in Table 8.

In the perfect TiO_2, the stoichiometry or the O:Ti ratio is always 2. Table 8 shows that the TiO_2 prepared by TTIP precursor is more close to the stoichiometry ratio but the TiO_2 films from TiOMe have stoichiometry around 1.7 which is lower than the ideal ratio.

Table 8: Stoichiometry of TiO_2 films prepared using TiOMe and TTIP. The ratio O:Ti is determined by using the equation 2.9.

ALD Cycles	O:Ti (TiOMe)	ALD Cycles	O:Ti (TTIP)
10	0.47	50	2.2
40	1.6	100	2.2
100	1.67	150	1.97
200	1.7	200	1.97

In the spectroscopic data analysis of TiO_2 grown using two precursor TiOMe (solid) and TTIP (liquid), the characteristic of film and ALD system is studied. It is found that the growth rate in case of TiOMe is lower compared to the TTIP. The TTIP grown TiO_2 contains higher amount of Ti^{3+} states compared to TiO_2 grown using TiOMe. But on the other hand the stoichiometry of TiO_2 from TTIP is close to the ideal value 2 whereas in the first cycles of TiOMe the oxidation is low and an O:Ti ratio is of only 0.47 present in the film. Moreover, even after 200 ALD cycles the stoichiometry could not reach to the ideal value of 2 when the TiOMe precursor was used. One of the most important differences is that the TiOMe needs to be heated at 180 °C to get the appropriate vapor pressure. So comparing the growth parameters and quality of TiO_2, the TTIP is found to be the better precursor than the TiOMe. So the further studies including ALD characteristics and the electronic properties are carried out using TTIP as precursor.

3.1.1 Affect of substrate temperature on TiO_2 ALD growth using TTIP

The TTIP precursor has an ALD window between 200-250 °C (108). In this work the temperature range is extended at both ends of the ALD window (i.e. the temperature range of 150 °C to 315 °C is investigated) to check the growth rate as well as the quality of TiO_2 deposited. In this study of temperature dependence, the deposition is carried out with the in-situ ALD system at BESSY U49/2- PGM2 beam line. P-type Si with native SiO_2 is used as substrate for deposition.

The Si2p core level can be used to determine the thickness of the TiO_2 over-layer deposited on the Si/SiO_2 substrate. When the TiO_2 over-layer is deposited on Si the number of photo emitted electrons coming from the Si decreases due to the loss of kinetic energy of the electrons through the TiO_2 layer. At investigated the substrate temperatures 200 ALD cycles have been performed on the Si/SiO_2 substrate. Figure *22*(a) shows the signal of Si2p before and after deposition of TiO_2 at different temperatures. For comparison study the peak at higher energy due to the Si^{4+} state is normalized to one so that the decrease in intensity of Si^0 can be detected and the thickness of TiO_2 can be estimated. The signal to noise ratio gets worse when the TiO_2 is deposited at 250 °C or above as much smaller intensity is detected. Moreover, the shift in binding energy of the Si^{4+} peak suggests that the deposition at 250 °C and above has higher growth rate than the deposition at 150 °C. In addition, the O1s spectra in Figure *22* (b) show that the TiO_2 deposited at 150 °C carries a clear SiO_2 contribution at 532.7eV whereas with the increase in deposition temperature this peak diminishes. At the growth temperature of 200 °C a peak at higher binding energy is still observable but above 250 °C this peak is not visible at all. The thicknesses of the 200 ALD layers deposited at different temperature are tabulated in Table 9 and the thickness is calculated using equation 2.9.

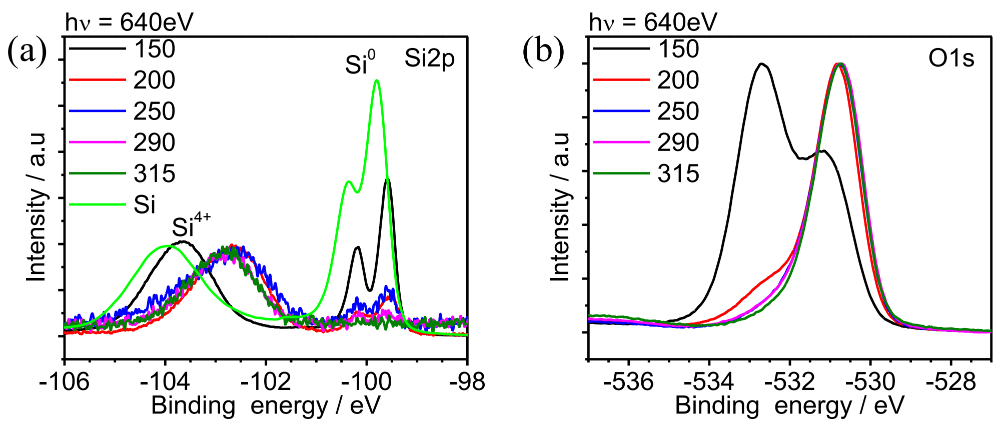

Figure 22: Si2p (a) and O1s (b) core level spectra of TiO_2 deposited at different substrate temperatures using TTIP. Photon energy of 640eV is used for PES measurements and the labeling in the figure corresponds to the respective temperatures.

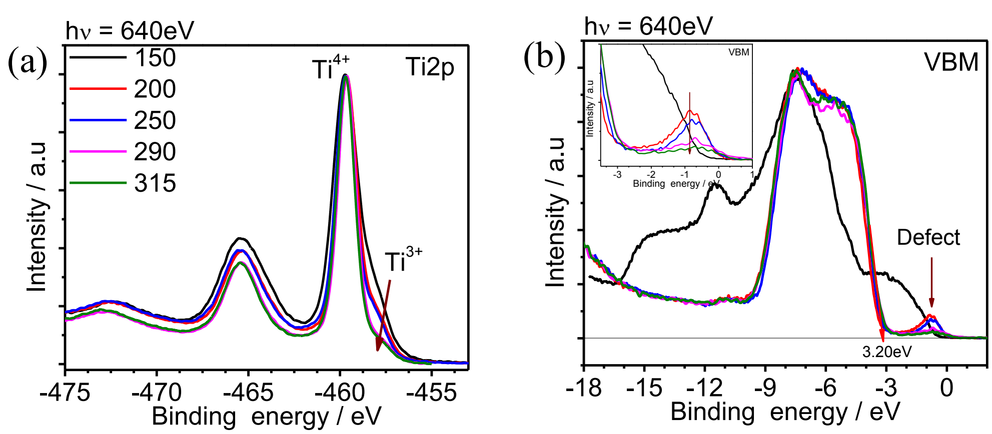

Figure 23: Core level spectra of Ti2p (a) and valence band spectra (b)of deposited TiO_2 films at different temperatures as labeled in part (a). The inset in figure (b) shows the in-gap (defect) states of the TiO_2 films.

The quality of the TiO_2 films can be evaluated from the Ti2p core level and valence band spectra of the TiO_2 films. In Figure 23 (a) the Ti2p core level has a peak at 459.5eV corresponding to the Ti^{4+}

states with a accompanying Ti^{3+} shoulder at lower binding energy. The film grown at 150 °C shows the highest amount of Ti^{3+} states, while The Ti^{3+} intensity goes on decrease with the increase in growth temperature. The Ti^{3+}:Ti^{4+} ratio is one of the most important factors to determine the quality of the TiO_2: therefore the $Ti2p_{3/2}$ peak is fitted into two curves to get the Ti^{3+}:Ti^{4+} ratio as shown in Figure 20. The valence band maxima of the films are determined form the VB spectra in Figure 23 (b) and the VBM is found to be 3.20 eV other than the film grown at substrate temperature 150 °C. In all films grown at different temperatures in-gap state around 1eV below the Fermi level are observed. This defect can be clearly seen in the inset figure of Figure 23(b). The films grown at 150 °C have no clear distinguishable defect states since the Si VB overlaps with the Ti defect states. Under careful analysis it can be seen that the intensity of the defect state decreases with the increase in substrate temperature. So, the increase in temperature causes the decrease of intensity of Ti^{3+} states as well as of defect states in TiO_2. From this a conclusion can be drawn that the Ti^{3+} states are corresponding to the defect states in TiO_2 can be studied to understand the affect of substrate temperature on growth and quality of the TiO_2 layer prepared by ALD method. The stoichiometry calculation states that the grown material has ideal stoichiometry when the substrate temperature is 200 °C or more. The growth rate is very low (0.75Å) but in the temperature range of 200 to 290 °C the growth rate is around 1.5 Å and this growth rate is in agreement with the literature (105). With temperature raising the growth rate increases but this increase can be due to the starting of the decomposition of the TTIP precursor, since the onset of its decomposition is around 250 °C (108). From the spectroscopic measurements and the data analysis it is evident that at substrate temperature of 150 °C the growth of TiO_2 is not favorable for this precursor by ALD methods. The correlation between the Ti^{3+} states in the film and the defect intensity can be also observed from Table 9. The intensity increase of Ti^{3+} states goes along with an increase of the intensity of the defect states and the correlation between these two parameters suggests that the defect (in-gap) states are due to the presence of Ti3d state in the valence band.

Table 9: Thickness, Ti^{3+}:Ti^{4+} ratio and the intensity of defect states of TiO_2 films deposited at different substrate temperature using TTIP precursor as Ti source and H_2O as O source.

Substrate temp. (°C)	**Thickness of TiO_2 film (GPC/nm)**	**Stoichiometry O:Ti**	**Ti^{3+}:Ti^{4+}**	**Intensity of the defect state**
150	1.5 (0.075)	1.7	0.161	-
200	2.9 (.0144)	1.96	0.135	0.08
250	2.9 (0.144)	2.0	0.088	0.068

290	3.5 (0.175)	2.0	0.047	0.039
315	3.5 (0.175)	2.05	0.051	0.023

The temperature dependent ALD growth and the spectroscopic analysis show that the growth is constant between 200 and 290 °C. In this temperature range not only the growth rate is constant but the film quality such as stoichiometry, and Ti^{3+} to Ti^{4+} ratio approaches the ideal value for TiO_2. Due to the constant growth rate (ALD characteristic) and good film quality the further studies are conducted with the substrate temperature of 250 °C.

3.1.2 Affect of heating procedure on TiO_2 ALD growth using TTIP

During the optimization of the deposition parameters we studied the affect of different heating processes like heat radiation (indirect heating) and resistive heating (direct heating by applying electrical power to the sample holder clips). In Figure 24 comparisons of the Ti2p, O1s and Si2p core level spectra of TiO_2 on Si/SiO_2 substrate are shown. In both types of substrate heating 200 ALD cycles are deposited using TTIP as Ti precursor and H_2O as oxygen precursor. The Ti^{3+} to Ti^{4+} ratio in these films can be evaluated from Figure 24(a). The Ti2p spectra show that the Ti^{3+} content is lower for the sample grown with direct heating compared to the sample grown with indirect heating. Figure 24(b) shows the O1s spectra and a shoulder at higher binding energy around 533 eV is visible for both films. This shoulder could be due to the absorbed –OH on the TiO_2 surface; due to the fact that the film deposited by direct heating is thick to get the O1s contribution from the SiO_2 substrate (117). The Si2p signal in Figure 24(c) suggests that the TiO_2 film is thicker with direct than the indirect heating. From the analysis of the Ti2p and Si2p spectra the ratio between Ti^{4+} and Ti^{3+} and the growth rate of the films can be determined as explained in previous sections. The growth rate per cycle is 0.015 and 0.025nm with a Ti^{3+}:Ti^{4+} ratio 0.077 and 0.045 for samples grown with indirect and direct heating respectively. In the direct heating process the higher growth rate can be addressed to the CVD type growth of TiO_2. The point of the substrate where the heating power is applied has higher temperature than the rest of the substrate surface. This inhomogeneous temperature distribution can contribute to CVD like growth mode due to local heating. Not only the growth process but also the electronic properties of the TiO_2 deposited using two different heating techniques are different and this will be discussed in the later part of this chapter on the basis of XAS measurements.

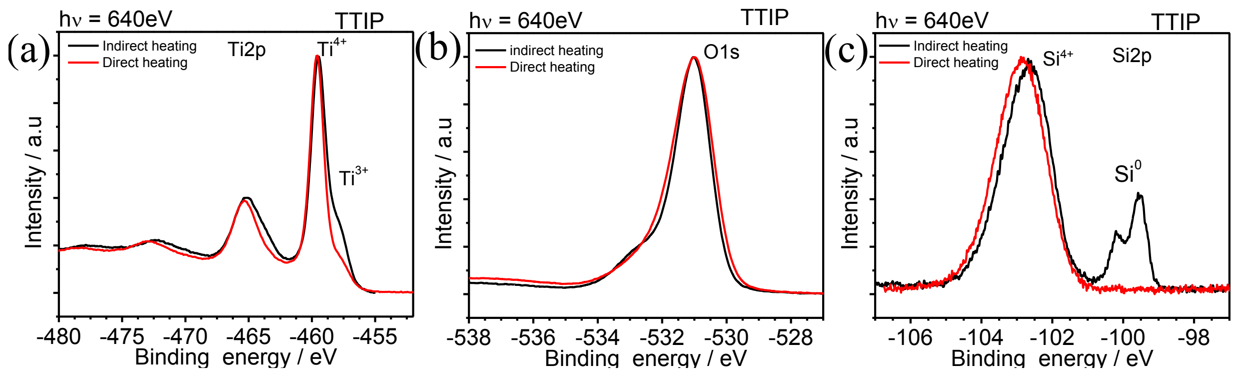

Figure 24: A comparison of core level spectra of Ti2p (a), O1s (b) and Si2p (c) core level spectra of TiO_2 deposited by two heating processes. In the indirect heating process the sample is heated by heat radiation and in direct heating process is heated resistively.

3.1.3 Affect of substrate on ALD TiO_2 growth using TTIP

The ALD being a low temperature deposition process is most important for the deposition on various substrates in the field of microelectronics as well as catalysis. When ALD is used to deposit TiO_2 on different substrates it has different interface as well as electronic properties [(111), (118)]. In the present study we also we investigated the growth of TiO_2 films and their spectroscopic properties on different substrates.

The XPS spectra of TiO_2 films deposited with 100 TTIP/H_2O cycles on different substrates namely Si, WO_3, RuOx, Cu_xO_y and AlON are shown in Figure 25. The O1s spectra (Fig. 25a) have a wide full width at half maximum (FWHM) due to the oxygen component from the substrate. In case of RuO_x substrate the O1s has a distinct shoulder at lower energy which corresponds to the oxidation of Ru (119). Along with the contribution of oxygen from the substrate there is also substrate –OH bonding at higher binding energy. The contamination and/or the substrate contribution will be eliminated during the calculation of oxygen to metal ratio. The Ti2p peak (Fig. 25b) is at 459.5 eV and it has a shoulder at lower binding energy which shows the amount of Ti^{3+} in the TiO_2 films. The VB (Fig. 25c) is measured with 458eV photon energy for higher surface sensitivity to get the information mostly from the TiO_2 over layer on different substrates. The VB spectra are used to determine the VBM of the TiO_2 films on different substrates and it is around 3.3 eV below the Fermi level for almost all the samples. But discrepancies are there for films grown on RuO_x and Cu_xO_y and these could be due to the lower thickness of TiO_2 on these substrates. In the VB spectra the in-gap (defect) state is around 1 eV below the Fermi level for all the samples. In case of RuOx substrate the VBM is visible and coincides with the defects state of TiO_2 due to the lower deposition rate on this substrate.

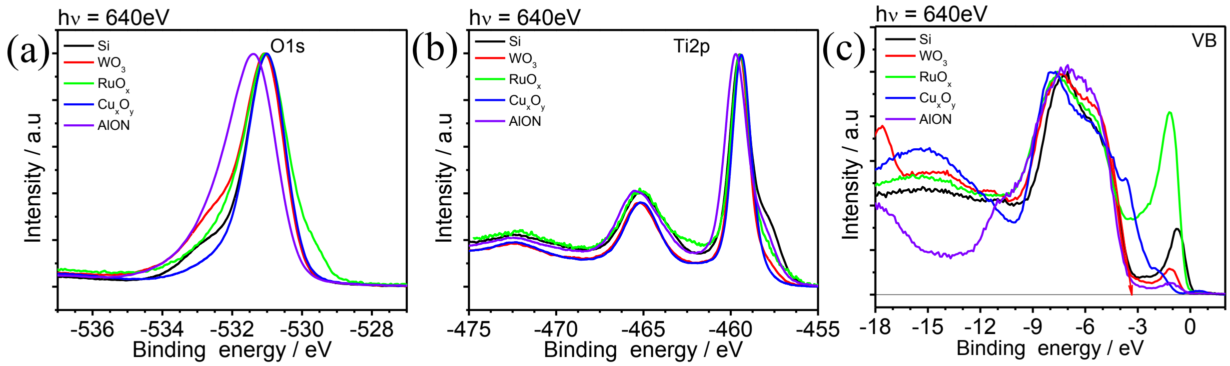

Figure 25: XPS spectra of TiO_2 deposited on different substrates at 250 °C using TTIP as precursor. The O1s core level (a), Ti2p core leve (b) and VB (c) are shown in this figure. The substrates used are Si, WO_3, RuO_x, Cu_xO_y and AlONas labeled within the diagram. 100 ALD cycles are performed on each substrate.

Table 10 overviews the stoichiometry, Ti^{4+}/Ti^{3+} ratio and VBM position of these TiO_2 layers on different substrates. All TiO_2 films grown on different surfaces show an O:Ti ratio of around 2. In the quality evaluation of the film the Ti^{4+} to Ti^{3+} ratio is one of the most important factors and from Table 10 it is clear that for the TiO_2 grown on WO_3 or Cu_xO_y this ratio is better compared to the Si and other substrates (AlON, RuOx).The determination of the VBM for these films is more crucial since the contribution of the substrate at the VB edge cannot be avoided even if the photon energy used here is more surface sensitive than the photon energy (640eV) used to measure the core levels. Therefore in the VB measurements a state from RuOx and Cu_xO_y are visible and cause a shift of the VBM of the TiO_2 over-layers on them. The TiO_2/RuO_x sample shows the in-gap states which extend into the Fermi level and this contribution shows that the interface of TiO_2-RuO_x has Ru metal like interface (119). The same effect is also seen for the TiO_2 grown on Cu_xO_y substrate where the VB is mostly consisting of substrate signals. An interesting feature is that the intensity of the in-gap sate varies with the substrate. The decrease in intensity of the in-gap state is in order Si> WO_3> AlON. The comparison of electronic properties of TiO_2 on different substrates will be discussed in the later part along with the XAS studies.

Table 10: Stoichiometry, Ti^{3+}:Ti^{4+} ratio and VBM position of TiO_2 grown on different substrates.

ALD layers	O:Ti ratio	Ti^{3+}:Ti^{4+}	VBM position
Si	2.2	0.116	3.3
WO_3	2.2	0.066	3.46
RuO_x	2.1	0.105	2.74
Cu_xO_y	1.9	0.054	2.36
AlON	2.1	0.135	3.69

3.1.4 X-ray absorption spectroscopy of TiO_2

X-ray absorption spectroscopy measures the absorption of the incident X-ray as function of its energy. The XAS measurements are carried out scanning over the metal (Ti) L-edge and O K-edge with simultaneously varying the photon energy and collecting the total electron yield (TEY) with the help of a KEITHLEY ampere meter. The data collected here are presented as the plot of absorption intensity as function of photon energy.

In XAS the X-ray is absorbed by the atom and the core level electron is excited into the conduction band in the resonance energy range. The unoccupied states of the material can be probed with the XAS measurements. In addition the XAS can provide information about structural, electronic and chemical environment of the material. When TiO_2 is excited with photon energy in the range of 452 to 480 eV electrons from the Ti2p ($2p_{1/2}$ and $2p_{3/2}$) will be excited into Ti3d states in the conduction band.

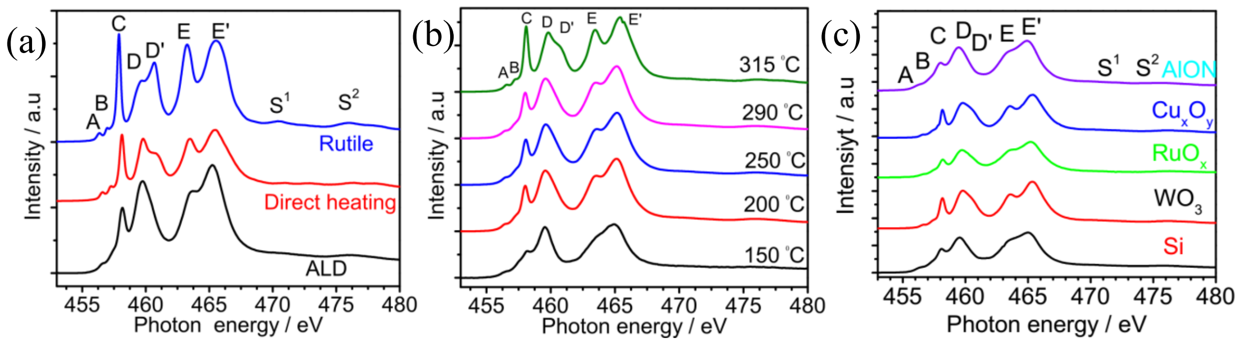

Figure 26: Ti $L_{2,3}$ edge XAS spectra of TiO_2 prepared by ALD, direct heating ALD and the single crystal rutile (a), as well as of ALD grown TiO_2 at different substrate temperatures (b) and on different substrates with normal ALD technique. The spectra shown here are collected with total electron yield from the sample.

In Figure 26(a) XAS spectra at the Ti $L_{2,3}$ edge for TiO_2 prepared by different ALD processes such as normal ALD (the samples are heated with using an indirect heating), direct heating ALD (samples are heated by resistive heating) are shown along with the XAS of rutile single crystal for comparison. In Figure 26(b and c) the Ti $L_{2,3}$ edge spectra for TiO_2 grown at different temperature on Si/SiO_2 substrate and TiO_2 grown on different substrates at 250 ºC substrate temperature are shown. All the spectra in the Figure 26 are normalized with the atomic absorption coefficient. In general the XAS spectra of titanate family appear to be rather similar. The Ti $L_{2,3}$ edge XAS signal has the same profile of spectra for orthorhombic TiO_2 [(120), (121)], $SrTiO_3$ (122), as well as amorphous and nano-crystalline TiO_2 (123). The XAS spectra can be characterized by two main regions namely $L_3(2p_{3/2})$ and $L_2(2p_{1/2})$ in the energy range 456-462 eV and 462-468 eV respectively (124). These two distinct regions appear due to the spin orbit splitting of $Ti2p_{1/2}$ and $Ti2p_{3/2}$ core levels. There are five main peaks and two low intense peaks at lower photon energy of the XAS spectra. The two low intense peaks are labeled as A and B and are known as pre-edge peaks. Next to the pre-edge peak the highest intense peak is labeled as C, the following double (broad) peak is named as D and D' at around 460 eV and finally there two higher energy peaks at around 463 and 465 eV are named as E and E'. Towards higher photon energy two satellites (S^1 and S^2) are visible at photon energies of 470.54 and 476.03 eV and these results are in accordance with the literature [(124), (125), (126)].

The characteristic peaks C, D and D' can provide information about the polymorphs of TiO_2. In Figure 26(a) the peak around 460 eV has a single broad peak for ALD TiO_2 samples , while that of direct heating ALD and the rutile reference samples have double peaks D and D'. One of the interesting fact is that the intensity of the peak D is higher than D' for direct heating ALD sample and for single crystal rutile sample the intensity ratio of these peak is reversed. Moreover the peaks E and E' are of equal intensities for direct heating ALD and rutile samples while the indirect heating ALD samples exhibits a higher E' than E intensity. In case of rutile and direct heating ALD samples the intensity of peak C is higher or comparable to the doublet peaks at D and D' but in case of indirect heating ALD samples it is reversed. In the present study, the sample prepared by direct heating ALD resembles with the XAS spectra of anatase TiO_2 (123). However, the films prepared by indirect heating ALD have neither antase nor rutile polymorphs. In case of $SrTiO_3$ the peak at around 460 eV appears as a single peak but in case of ALD layers this absorption band is more broadened as in case of nano-crystalline or amorphous TiO_2 (127). In the literature no detail about the single broad D peak is given and it is found that this single peak is observed for nano-crystalline or amorphous TiO_2 layers. So we believe that our ALD grown TiO_2 layers are lacked of long range crystalline ordering and these layers can be amorphous or nano-crystalline. The direct heating ALD samples have anatase polymorphs and this phase is only visible with direct heating. In the process of direct heating the sample has higher temperature than 250 ºC (around 300 ºC) at the touch point of the electric finger used to apply electrical power to the samples. On deposition of TiO_2 the film gets crystallized at the touch point of electric finger and the crystallization continues over the whole surface.

The XAS spectra of Ti $L_{2,3}$ edge for TiO_2 films deposited at different substrate temperatures are shown in Figure 26(b). The samples grown in the temperature range from 200 to 290 ºC have similar XAS spectra. The sample grown at 150 ºC has only one broad signal at L_3 edge without strong C peak (only shoulder-like) compared to the other samples. The main peak at L_3 edge is at 458.5eV and the shoulder is at lower photon energy. This kind of spectral profile at Ti $L_{2,3}$ edge is due to the lower oxidation states of the titanium such as in Ti_2O_3 and Ti_5O_9 [(128) (129)]. The peak D of the sample grown at 150 ºC is shifted by 100meV due to the higher screening effect of conduction band electrons to the core holes (128). The Ti^{4+}:Ti^{3+} ratio of this sample is (6) lower than for the other samples grown at higher temperatures as given in Table 9. On the other hand the TiO_2 deposited at 315 ºC shows two distinct peaks at D and D' in the XAS spectrum. This signature corresponds to the anatase phase of TiO_2. Due to the higher substrate temperature the growth rate is also higher and at this temperature the TTIP starts to decompose. The higher growth rate and anatase phase like spectrum signature of TiO_2 films deposited at 315 ºC are due to the CVD like growth while in the temperature range of 200-290 ºC the normal ALD growth is observed. From these data it can be concluded that the TTIP precursor has the ALD window in the temperature region between 200 to 290 ºC and the films of TiO_2 grown within this temperature window are amorphous or nano-crystalline without long range crystalline ordering.

The affect of the kind of substrate on TiO_2 can be observed from Figure 26(c) in the XAS spectra at the Ti $L_{2,3}$ edge. The TiO_2 deposited on Si, AlON and RuO_x substrates have similar features. This indicates that the growth of the TiO_2 is same on AlON and RuOx surfaces as on the Si surface. In case TiO_2 growth on copper oxide and tungsten trioxide the TiO_2 grown XAS spectra have a different profile than the other substrates. In these two substrates the peak C and D are of equivalent intensity and has a shoulder D' at higher energy. In addition the L_2 edge peaks E and E' are well separated from each other and weak lower energy pre-edge peaks (A and B) are also visible. The characteristic peaks of TiO_2 when grown on Cu_xO_y and WO_3 are seen in anatase TiO_2. But the peak D is not completely developed rather it is a shoulder at higher photon energy. So it can be concluded that the TiO_2 layers grown on Si, AlON and RuO_x are amorphous films while the TiO_2 grown on WO_3 and Cu_xO_y have partial amounts of antase phase in these films.

From the XPS analysis of TiO_2 deposited using TTIP and TiOMe precursors growth rates per cycle of 0.015 and 0.006 nm respectively were determined (see chapter 3.1 Deposition of TiO2 by ALD). The growth rate is lower due to the lower vapor pressure generated by TiOMe solid precursor. Also with different ALD processes the polymorphs of TiO_2 films can be modified. From the XAS analysis it is observed that with the direct heating ALD TiO_2 films with anatase phase and with the indirect heating ALD amorphous TiO_2 films can be obtained. The substrates have only a little effect on the polymorphs of TiO_2 when it is deposited by ALD method. A little amount of anatase phase is found in TiO_2 films deposited on Cu_xO_y and WO_3 while on Si, AlON and RuO_x substrates amorphous or nano-crystalline films are formed. By the use of the easy processing of ALD using TTIP precursor and by changing kind of the heating process the properties of the grown TiO_2 layers can be modified and different polymorphs like amorphous and anatase can be obtained. So for further study of the electronic properties of TiO_2, TTIP precursor is used in ALD process. Both amorphous and anatase films can be realized on Si/SiO_2 substrates by selecting the according substrate heating procedure. For comparison the single crystal rutile sample is used to study the electronic properties by X-ray spectroscopic methods.

In the section 3.2 a detailed analysis of XAS at the Ti $L_{2,3}$ edge of amorphous, anatase and rutile will be preformed. The XAS will be addressed with the res-PES study at the Ti $L_{2,3}$ edge. In another section 3.2.2.4 the band gap determination of TiO_2 combining both XSP and res-PES will be performed. In that section the partial density of states will be determined by using res-PES at both Ti $L_{2,3}$ and O K edges.

3.2 Investigation of electronic properties of TiO_2

The TiO_2 has different polymorphs and the polymorphs can be produced with different synthesis techniques. Depending on the polymorphs and different interfaces the electronic properties and hence the functionality of TiO_2 layer change too. In the previous section the growth of TiO_2 deposited by ALD has been investigated with XPS and XAS measurements and a change in growth profile as well as in the quality of the films have been observed. In this section the electronic properties of TiO_2 will be studied using XAS and res-PES measurements. Firstly, the XAS of TiO_2 will be extended regarding the previous chapter and afterwards the res-PES data analysis for electronic studies.

3.2.1 X-ray absorption spectroscopy of TiO_2 at Ti and O edge.

In the previous section the XAS was mainly discussed in terms of polymorph discrimination. In this chapter a closer look to the XAS data regarding the electronic properties will be done. The XAS spectra of TiO_2 as shown in Figure 26 can be divided into two main regions namely L_3(455 to 462eV) and L_2 (462 to 467 eV) where as introduced above the L_3 edge peaks are named as C, D and D' and in L_2 edge E and E' are labeled; and along with the main peaks a pair of pre-edge peaks A and B and a pair of satellites S^1 and S^2 at higher photon energy appear. The characteristic peaks D and D' are used as a fingerprint to identify the polymorphs of TiO_2 (123) as discussed in the previous chapter. In general the peaks are assigned to as t_{2g}(C), e_g(D-D') at the L_3 edge and t_{2g}(E) and e_g(E') at the L_2 edge. The assignment is done on the basis of atomic crystal field theory [(124), (130)].

The origin of the different peaks in the absorption spectra at the Ti $L_{2,3}$ edge is a matter of debate in the literature. Thereby, one of the most widely accepted explanation of XAS spectra is the atomic crystal filed explanation proposed by de Groot (130). Over the time many other theoretical works have tried to explain the XAS spectra at the $TiL_{2,3}$ edge. Among them the inter particle approximation (IPA) (131), many body perturbation theory solving Bethe-Salpeter (132) and most recently multichannel multiple –scattering calculation (MMSC)method (133) have been applied.

In the following the results of these theoretical approaches are shortly described. The XAS spectra at the$TiL_{2,3}$ edge appear due to the excitation of electrons from $Ti2p_{3/2}(L_3)$ and $Ti2p_{1/2}(L_2)$ to the unoccupied Ti3d states. In the atomic-multiplet calculation $TiL_{2,3}$ edge XAs spectra consist of four peaks containing two strong peaks for the L_3 edge and one strong and one weak peak for the L_2 edge (65). In contrast, in the IPA calculation only three peaks appear at the $TiL_{2,3}$ edge. On the other hand the BSE approach gives more exact spectral information of the Ti $L_{2,3}$ edge XAS. In this calculation method the Coulomb interactions of core hole-excited electrons are included. The theoretical calculation involving the BSE approach is in agreement with the experimental XAS data. The separation between the L_2 and L_3 edge arises as result of spin-orbit splitting and amounts in the experimental data to 5.2 eV, 5.26 eV and 4.88 eV for ALD layers, anatase and rutile TiO_2 respectively, while in the BSE calculation it is about 5.65 eV. In Figure 26(a) the branching ratio of L_3 to L_2 is about 1:1 and the separation between the main peaks at L_2 and L_3 edge is around 2 eV. The theoretical calculation of XAS spectra using BSE method (66) also matches to these experimental values. The detail about the peak separation and the spin obit splitting energy are given in Table 11.

Table 11: Crystal field and spin orbital splitting of ALD layers, anatase films and rutile TiO_2. The values are determined from the XAS spectra presented in the Figure 26a.

		ALD layers(eV)	**Anatase(eV)**	**Rutile(eV)**
Crystal field splitting	L_3(C-DD')	1.56	1.96	2.30
	L_2(E-E')	2.15	2.36	2.50
Spin-orbit splitting		5.2	5.26	4.88

The pre-edge peaks A and B are clearly visible for anatase and rutile samples while in case of ALD sample only one broad peak A is visible in Figure 26(a). The pre-edge peaks are of the spin-forbidden transition and it can be associated with the structural defects. The crystal field theory proposed by de Groot shows that the pre-edge peaks appear as the result of octahedral crystal field splitting (130). The origins of these peaks are associated with the excitonic transitions within the band gap as suggested by Brydson et al. (134). These states can act like bands where the charge due to the core hole can be screened by the Bloch like wave functions. The theoretical work of Krüger et al. showed that using MMSC with the partial screening potential between the core hole and excited electron, delivered the pre-edge peak appearance in agreement with the experimental data (65). Here the partial screening potential was taken as 10%.

The most intense peak in the XAS profiles of anatase and rutile samples at the Ti $L_{2,3}$ edge is C but for the ALD sample the peak is less intense than the D-D' peaks. By the theory of crystal filed splitting the C peak at the L_3 edge can be explained as the transition of Ti2p core electron to the t_{2g} orbitals (130). Herby, the excitation of electrons into Ti3d states can result the formation of an exciton, where an interaction between the core hole and the excited electron is necessary. The core level can be stabilized by the formation of excitons if there are not enough electrons in the conduction band to screen the Coulomb interaction.

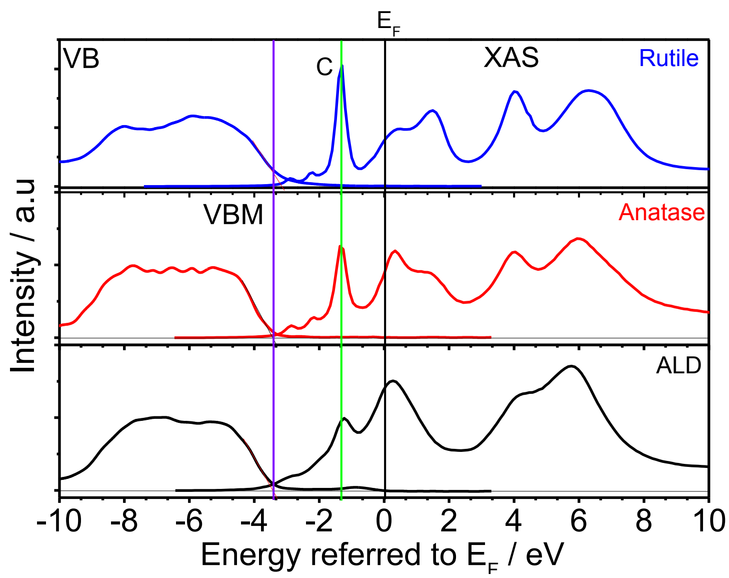

Figure 27: The VB and XAS (TEY) are aligned with respect to the Fermi level for ALD, anatase and rutile TiO_2.

Figure 27 shows the VB and XAS (TEY) spectra aligned with respect to the Fermi level. The XAS peak C lies below the Fermi level. The dipole allowed transition which gives the electronic band gap is 4.2 eV (45). When the peak C is from Ti2p to t_{2g} then the position of C peak will carry band like character but it appears within the band gap. The gap state C can be due to the pure excitonic transition. In the present analysis it is difficult to identify the nature of the excitonic states as stated by Letizia et al. that the anatase and rutile have localized and delocalized excitonic states (46). In our XAS measurement the excitonic band width is around 1.3 eV for all the three kinds of TiO_2 investigated. The experimental absorption spectra show excitonic band edges at 3.7-3.9 eV for rutile and 3.9 eV for anatase with respect to VB (46). But in XAS measurements the excitonic states are found to be at 2.2 eV with respect to the

VB. The res-PES measurement at O1s edge is able to get the quantification of polaronic contribution to the electronic properties of TiO_2. The relative polaronic intensity is given in the Table 17 and is around 25%. The existence of polarons increases the screening potential between the core hole and excited electrons. Indeed polarons (135), i.e. the electron phonon coupling, and oxygen vacancies can decrease the excitonic edge stronger than direct excitons (46).

The L_3 e_g (D-D') peak and L_2 t_{2g} (E) and e_g (E') peaks can be discussed using the atomic crystal field theory since these peaks have band like features. The broad peak at 460 eV (Figure 26a) is originated from the transition of electrons from Ti2p to e_g at the L_3 edge while the E and E' peaks are originated due to the transition from Ti2p to t_{2g} and e_g orbitals respectively. The splitting of the e_g peak at the L_3 edge which is used as a fingerprint to identify the polymorphs of TiO_2 (see previous chapter) is a matter of debate in the literature. The explanation of splitting of Ti L_3 e_g peak was proposed by de Groot et al. using crystal field theory in the distorted octahedron of TiO_6 [(130), (61)]. This approached was strongly questioned by Crocombette et al. (136) who declared the theory of ligand splitting at octahedron TiO_6 as responsible for e_g splitting. In the recent studies Krüger et al. used multichannel multiple scattering theory that resembles with the measured XAS patterns [(65), (137)]. According to this not only the TiO_6 octahedron but also a long range ordering is necessary for the splitting of the e_g peak at the L_3 edge. When the cluster size is of 60 atoms and the diameter of the cluster becomes 1.1 nm then the splitting of the e_g appears (65). Generally, the e_g orbital can be splitted into two sub orbitals a_g and b_{1g} and the difference in absorptions in these sub orbitals splits the e_g peak into two peaks. On the other hand Krüger et al. (65) showed that the absorptions at this two sub orbitals are very similar so these cannot lead to the splitting of the e_g peak at the L_3 edge of TiO_2. The splitting of the e_g peak is a combined effect of long range ordering of TiO_6 octahedrons with a small contribution from the distortion of the octahedrons. In the XAS spectra of our samples in Figure 26(a) the ALD sample has not splitting at the e_g peak and from this it might be inferred that the TiO_2 grown by ALD is lack of long range ordering.

3.2.1.1 Res-PES of ALD, anatase and rutile TiO_2 at the Ti2p edge

The res-PES measurements at the Ti2p edge are taken by collecting the photoelectron spectra at the VB region with incident photon energies below resonance (450 eV) to the far resonance (485 eV). In the process of res-PES measurements the electrons from the Ti2p core levels will be excited into the unoccupied CB and then the excited electron in the CB will decay via emitted photoelectrons. The res-PES measurement is helpful to determine the unoccupied states as well as intermediate Ti 3d states. Figure 28 shows the res-PES data of ALD (a), anatase (b) and rutile (c). The res-PES measurements are taken for initial state energies from VB region to -75 eV in the photon energy range 450 eV to 485 eV. Along the initial state energy region the increase in intensity shows the different contributions to the res-PES map. The photoelectron emission lines are shown by horizontal lines in the res-PES map. In the binding energy range -5 to -8 eV and increase in intensity is visible and is due to the emission in the VB. At higher binding energies other states such as O2s, Ti3p, and Ti3s states are visible at -23, -38 and -63 eV respectively with a Ti3p satellite at -51.5 eV (marked as 'Ti3p St.' in the figure). Near the resonance energy region an increase in intensity in the initial state energy region of -42 to -52eV is observed and this increase is accompanied by the change in the photon energy. The increase in photon energy and the change in position of the intensity along the initial state energy correspond to Auger like decay profile and will be discussed in the next paragraph in detail.

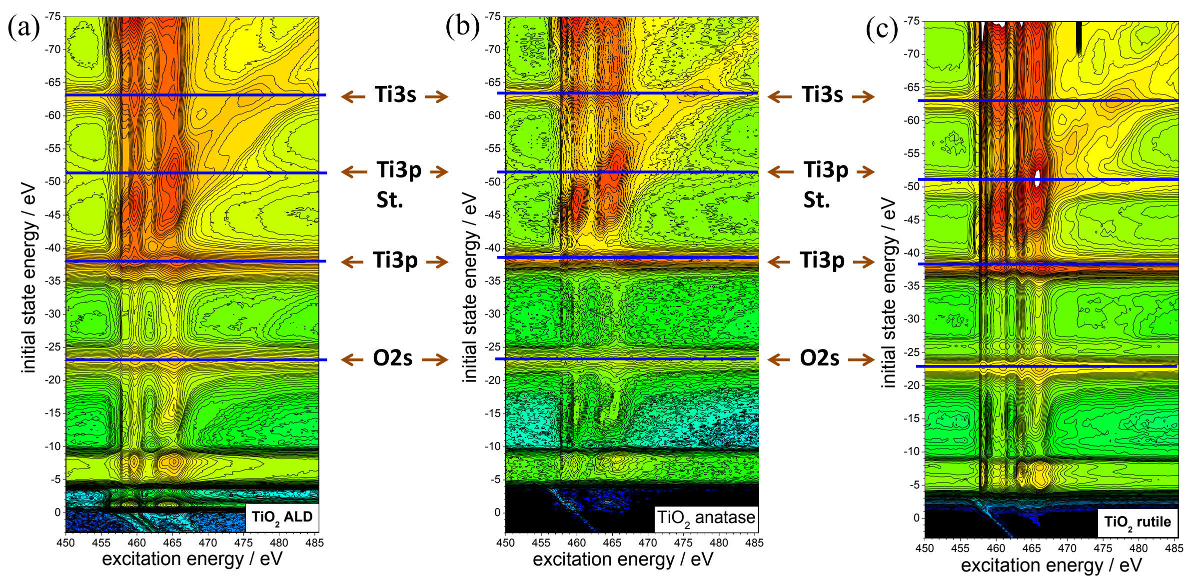

Figure 28: res-PES map of ALD (a), anatase (b) and rutile (c) TiO_2 at Ti2p edge in the energy range of 0 to 65 eV (VB) regions. The photoelectron spectra are collected with step of photon energy of 0.25 eV.

Figure 29 shows the res-PES measurement of ALD TiO_2 layers divided into two binding energy ranges from 3 to -32 eV (a) and from -32 to -70 eV (b) keeping the same photon energy range. The Partial Electron Yield (PEY) spectrum of the ALD TiO_2 films is obtained by integrating the res-PES map over the whole initial state energy range measured and is added into the res-PES aligning the photon energy equal to each other. Looking to the res-PES map it is clearly visible that before the resonance energy there is no increase in intensity and when it approaches towards the resonance energy the increase in intensity is observed for the whole initial state energy range. The res-PES near the resonance photon energy can be divided into two parts of energy ranging from 456 to 462 eV and 462 to 467 eV. In the range of 456 to 462 eV the transition from $Ti2p_{3/2}$ to unoccupied Ti 3d states occurs and it is known as transition from the L_3

edge while in the energy range of 462 to 467 eV the Ti2p$_{1/2}$ (L_2 edge) electrons will be excited into CB. By aligning the PEY spectra to the res-PES data it is very clear that the high intensities at around 460 and 465 eV within the res-PES maps corresponds to the L_3 and L_2 edge regions. In the XAS spectra two pre-edge peaks (A, B) are visible in the energy range from 456 to 458eV (refer to Figure 26) but in the res-PES data these two peaks are not visible in any of the TiO_2 samples. The intensity of the pre-edge peaks in the XAS spectra is very low and the res-PES measurements are taken with energy steps of 0.25 eV. So the lower intensity and the measurement resolution might not be good enough to detect the pre-edge states. Moreover, below the resonance no decay mechanism is observed in the res-PES map.

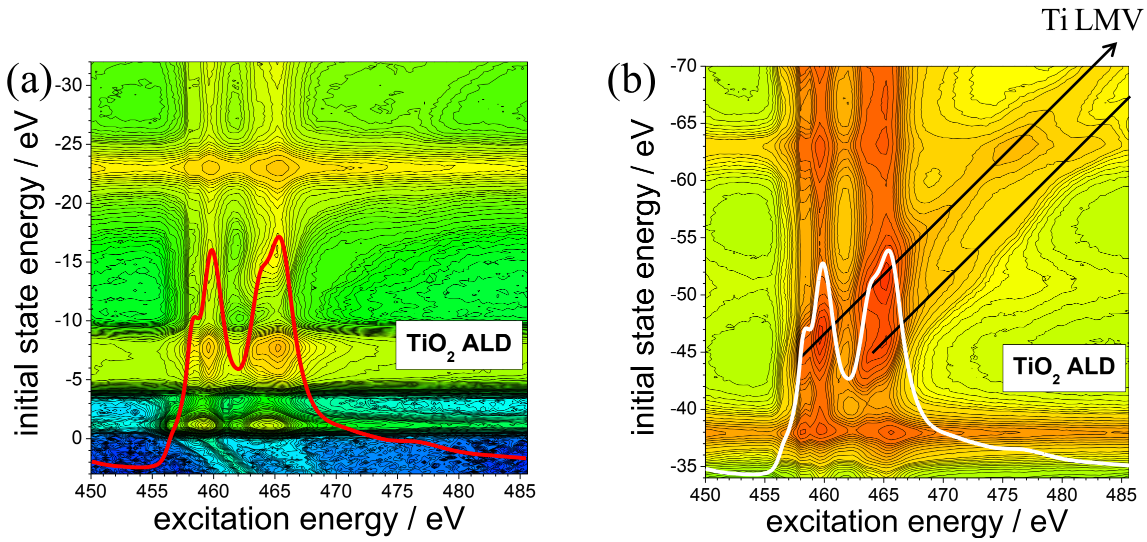

Figure 29: Res-PES map of ALD TiO_2 at the Ti2p edge in the energy range of 0 to 65 eV (VB) regions. The photoelectron spectra are collected with photon energy steps of 0.25 eV. The initial state energy region is divided into two plots; one is from 3 to -32eV (a) and the other one represents the range from -32 to -70eV keeping the photon energy range identical in both the plots. The red (a) and white (b) spectra are the PEY determined from the res-PES map by integrating over the whole initial state energy range. The arrows in (b) illustrate the Auger decay channels.

The higher intensity in the res-PES map can be seen at the energy of 459 eV which is just near the resonance energy. At this photon energy, the electron from the Ti2p$_{3/2}$ will be excited into the excitonic states near the CBM forming an exciton. In Figure 27 we found the highest peak at the L_3 edge is in the gap and is localized, therefore the higher intensity at 459 eV is from the excitonic transition. In the photon energy range of 459 to 462eV (L_3 region) the highest intensity changes with the photon energy are observed towards the initial state energy region between -41.7 eV and -49 eV. The increases in the initial state energy with the photon energy in this res-PES reflect the Auger decay of excited electrons. The emitted photoelectrons in these initial state and photon energy ranges will have a kinetic energy (KE) of around 414 eV and this KE of electron for the Ti atom corresponds to the Ti $L_3M_{23}V$ Auger decay. The exact KE of the emitted electrons in this region is difficult to predict since the excitonic state at 459 eV and the Ti2p$_{3/2}$-e$_g$ band transition at 460 eV are very close to each other at the L$_3$ edge.

The evidence of the Auger decay is clearer at the L$_2$ edge and it extends into far resonance photon energy region till 485 eV. At the L$_2$ edge two intensity profiles are visible as marked in Figure 29(b) by arrows. As marked here these two Auger intensity profiles start at the low energy edge (463 eV) of the L$_2$ edge and the corresponding KEs are 414 and 420 eV. The difference in the two Auger lines is 6 eV which is equivalent to the spin orbit splitting energy of Ti2p (Table 11). The first Auger line (L$_3$M$_{23}$V) has the highest intensity at the photon energy around 460 eV, afterwards the intensity decreases but increases again and gains the higher intensity around 465eV photon energy at initial state energy of -51 eV. The increase of the intensity at this point is due to the combination of photoemission of the Ti3p satellite and the Auger decay. The horizontal line along the photon energy at -51eV initial state energy in Figure 28 shows the Ti3p satellite emission peak and it combines with the Auger decay at 465 eV to give rise to the highest intensity of L$_3$M$_{23}$V decay. From the resonance energy measurements at the Ti L edge we found that the transitions at the L$_2$ and L$_3$ edges are accompanied by Auger decay processes.

In Figure 30 the comparison of the PEY obtained from integrating the res-PES data and the CIS at different VB positions such as -1, -5.8 and -7.8 eV initial state energies deduced also from the res-PES data are shown. The CIS taken at VB states of -5.8 and -7.8 eV show the same transition peaks as that of the PEY for all measured samples shown in Figure 31. The transition peaks at the L$_3$ and L$_2$ edges in the XAS data are well reproduced in the PEY curve as well as in the CIS data at -5.8 and -7.8 eV. In the ALD and rutile samples there is no difference in the peak patterns of PEY and CIS at different VB energies (-5.8, 7.8 eV) but in case of the anatase samples the CIS at -5.8eV has a broad peak with a shoulder at the L$_2$ edge. On the other hand the most visible difference is that the CIS data at -1eV initial state energy is not matching with the spectra profiles obtained in XAS or PEY data for all the three samples.

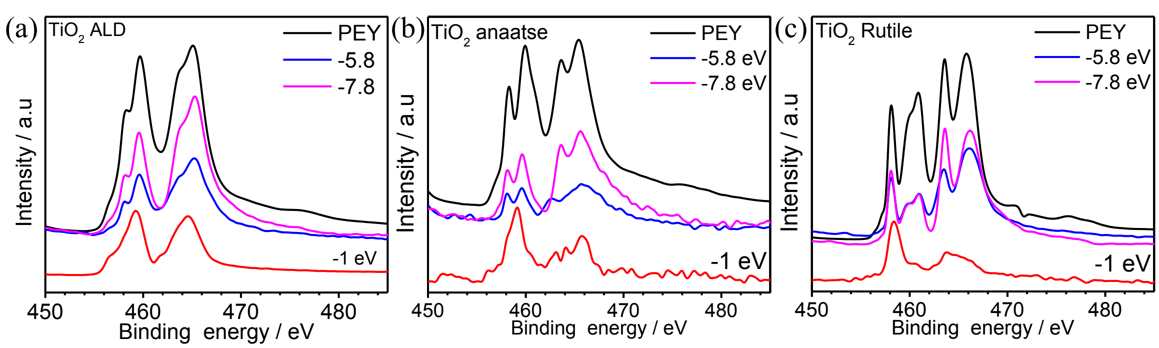

Figure 30: The PEY obtained from the res-PES map is shown along with the CIS at -1 eV and at two valence band states at binding energies of -5.8 and -7.8 eV for the ALD (a), anatase (b) and rutile (c).

The two VB CIS spectra at -5.8 and -7.8 eV differ from each other only in intensity and are also clearly recognizable in the PEY data. The intensities of the -5.8 and -7.8 eV CIS data differ in the same way at the L_3 and L_2 edges respectively for the ALD sample; while in anatase the difference is more pronounced at the L_2 edge and in rutile there is no difference at the L_3 edge at all. The CIS taken at -1eV has only two broad peaks with one peak at each edge in the ALD sample where the two peaks are of equal intensity. In contrast, in anatase and rutile the L_3:L_2 edge peak ratio goes on increasing. Moreover, the L_3 e_g edge peak in ALD TiO_2 is at 459.3 eV while it is at 459.1 eV in anatase and at 458.5 eV in rutile for CIS at -1 eV.

3.2.1.2 X-ray linear dichroism in TiO_2

The X-ray linear dichroism in TiO_2 was determined by collecting two XAS measurements at two different sample positions with respect to the linearly polarized incident beam. The sample was placed 45º to the incident beam and then rotated to a position (grazing angle) where the incident beam is nearly parallel to the surface of the sample. A schematic diagram of the measurements is shown in Figure 31 and the XLD is determined by taking the difference in absorption intensities of XAS at grazing and 45º angles. The percentage of XLD can be determined by using equation 3.3 which is a modified version of equation 2.20.

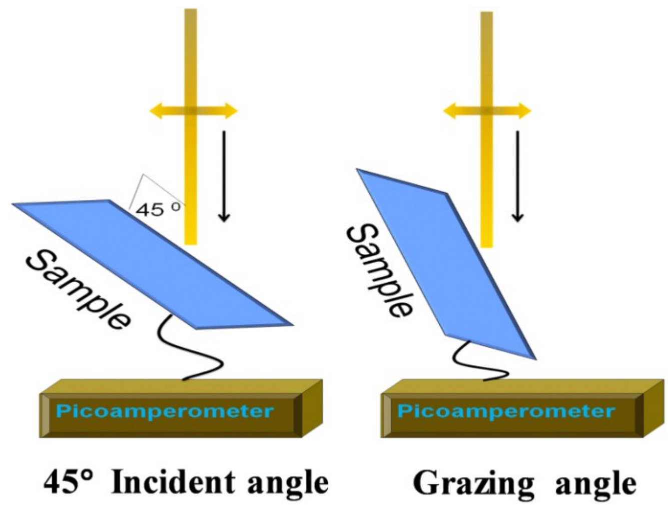

Figure 31: Schematic diagram of the tow different incident angles of X-ray beam with respect to the sample for XLD measurements.

$$\mathrm{XLD}(\%) = \frac{(I_{grazing} - I_{45})}{(I_{grazing} + I_{45})} \tag{3.3}$$

Here, we set ($I_{grazing}$+I_{45}) as the atomic absorption coefficient (AAC). The XLD is given as the percentage of the AAC. There by the XLD intensity values are in percentage of the absolute absorption intensity.

The XLD measurements are conducted on ALD samples and the anatase sample prepared by ALD. The XLD for 200 ALD layers and the anatase layer of TiO_2 are shown in Figure 32. The arrows in this figure indicate the individual XLD transition 1–6. Comparing the XLD intensities in Figure 32, it seems that anatase sample has very less XLD effect compared to the 200 ALD layers sample. The main XLD effects at the different transition energy are shown in Table 12 and Table 13. For the ALD grown TiO_2 sample, the highest positive XLD effect is at 466.16 eV (peak 6) with XLD 54 % in the L_2 edge and the highest negative XLD is at 458.82 eV (peak 4) with XLD -62.0 %at L_3 edge, whereas the anatase sample has the highest positive and negative XLD values of 23 and -4.0 % at 458.02 (L_3 edge, peak 3) and 466.32 eV (L_2 edge, peak 6), respectively. All XLD transitions at the L_3 and L_2 edges are summarized in Table 12 shown in Figure 33.

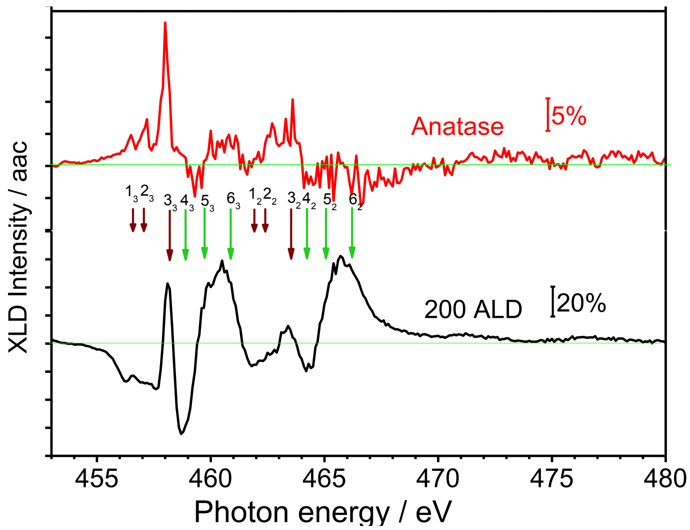

Figure 32: XLD of 200 ALD layers of TiO_2 and anatase phase of TiO_2 at Ti-$L_{2,3}$ edge.

Table 12: Energy positions of the main XLD and their corresponding intensities for the 200 ALD layers TiO_2 and anatase TiO_2 layers. The main transitions in Figure 32 are marked from 1 to 6 at L_2 and L_3 edges. The subscripts 3 and 2 with number 1-6 represent the L_3 and L_2 edge transition respectively. The individual peak position in this table is given in eV.

Peak positions			200 ALD layer	XLD intensity (%)	Anatase	XLD intensity (%)
L_3	pre-edge	1_3	456.4	-24	456.46	7
		2_3	457.09	-27	457.2	23
	defect	3_3	458.08	43	458.02	-4
	t_{2g}	4_3	458.82	-62	459.24	-3
	e_g	5_3	459.68	37	459.7	4
		6_3	460.83	43	460.9	2
L_2	pre-edge	1_2	461.94	-15	462.07	6
		2_2	462.42	-6	462.7	5
	defect	3_2	463.53	10	463.63	-2
	t_{2g}	4_2	464.17	-18	464.44	-3
	e_g	5_2	465.01	30	465.25	-4
		6_2	466.16	54	466.32	5

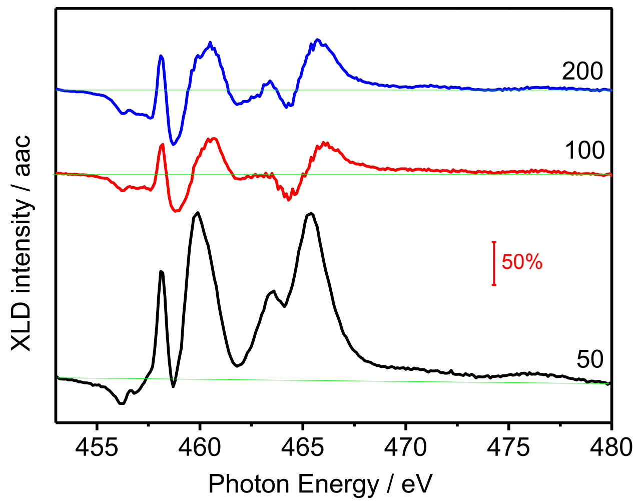

Figure 33: XLD of TiO_2 ALD films at Ti-$L_{2,3}$ edge after 50, 100, and 200 ALD cycles.

Table 13: XLD intensities at the Ti $L_{2,3}$ edge in percentage for 50, and 100 ALD layers along with the XLD intensity of anatase TiO_2 layers.

XLD transition position		**ALD layers**		
L_3		***Energy/eV***	***50 layers***	***100 layers***
	1_3	456.4	-11	-15
	2_3	457.09	-13	-16
	3_3	458.08	131	33
	4_3	458.82	-2	-44
	5_3	459.68	195	7
	6_3	460.83	105	39
L_2	1_2	461.94	19	-5
	2_2	462.42	39	-3
	3_2	463.53	108	-0.8
	4_2	464.17	92	-27
	5_2	465.01	179	-2
	6_2	466.16	131	36

For different thicknesses of TiO_2 layers grown by ALD, the XLD effect was studied and for all three samples prepared with 50, 100 and 200 ALD cycles there is found a prominent XLD behavior with very similar XLD patterns as shown in Figure 33. The XLD after 50 ALD cycles looks more like the XAS spectra itself, but with higher thickness the XLD signal changes and carry similar curve shapes for the samples grown with 100 and 200 ALD cycles The XLD percentages in dependence of the ALD cycle number are given in

Table ***13***. For the 50 ALD layers sample, the XLD intensity at 458.08 (peak 3_3), 459.68 (peak 5_3), 460.83 (peak 6_3), 463.53 (peak 3_2), 465.01 (peak 5_2), and 466.16 eV (peak 6_2) have values higher than 100 %. This is a consequence of the fact that the XLD percentage was calculated with respect to the AAC in order to make a reasonable comparison between the XAS and the XLD data of different thick ALD and anatase layers of TiO_2.

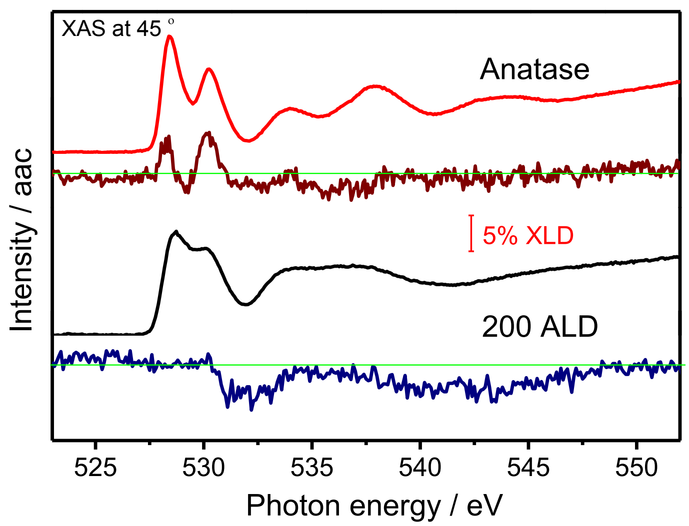

Figure 34: XAS of ALD and anatase layers of TiO_2 and their corresponding XLD at the O K edge.

The XLD at the O K was also determined for the ALD and anatase TiO_2 layers which are shown along with the corresponding XAS measured at 45°angle in

Figure *34*. We find for the anatase layer the characteristic split in the O1s signal while the 200 ALD layers sample just shows a broad absorption band. For both samples, the XLD signals are very weak (5 %), but it can be clearly seen that the XLD is only observed for the first absorption bands; whereas there are no signals for higher transition energies.

Considering the different preparation conditions of TiO_2 films, the XLD signals observed are different, indeed. Consequently, this means that for the different preparation conditions we are able to identify the strength of the local distortion. The main findings are the appearance of the XLD signal in the ALD layers, the particular shape of the XLD for the anatase polymorph, and the assignment of the first transitions of the XLD/XAS signals. In our XLD data at the Ti2p edge, we find a characteristic pattern shown in Figure 32 and Figure 33. There, we labeled the individual features with integer numbers of 1–6. We might be able to differentiate the individual multiplet branches by their individual contributions to the XLD signal. XLD thereby can contribute in understanding the XAS transitions in more detail.

For the Ti-L edge signals, we expect detailed information as the five 3d atomic levels are split by excitonic states, the band like transition. In the different samples, the local dipole momenta do not affect the characteristic splitting; instead the dipole momenta modify the intensity of the individual transitions. This reflects the fact that a change in the orbital overlap (caused by a local distortion) reduces/enhances the transition probability and not the eigenvalue of individual transitions (as long as we consider only weak perturbations). We may be able to learn about positive (enhancement) or negative (reduction) intensity changes of the regular XAS signals depending on whether the local dipoles are in line with the electrical field vector or not.

The XLD at O1s-edge seems to be very weak for both, the 200 ALD and the anatase TiO_2 layers. At the oxygen edge, the weak XLD effect could be due to the cancelation of dipole momenta. But in case of anatase, the XLD signal is a bit higher than for the amorphous ALD-grown TiO_2, the significant XLD intensity in anatase TiO_2 is contributed by the lower cancelation of dipole momenta of non-orthogonal bonding angles. The XLD signal in anatase informs about distorted Ti–O bonds but still the layer remains in its anatase polymorphism.

To understand the cause of XLD in the ALD and anatase TiO_2 layers we compare the experimental XAS and XLD curves with charge-transfer atomic multiplets calculation using CTM4XAS program by Stavitski and de Groot (138). The comparison between the calculated and the measured XLD is given in Figure 35. The octahedral symmetry O_h for the Ti^{4+} with a CFS (10Dq) is used to calculate the XAS of the ALD layers. The calculated XLD spectrum has been broadened; its intensity is arbitrarily scaled for comparison with the experimental XLD data. The arrows in the diagram represent the individual XLD components as determined from our experiments as listed in Table 13.

From this comparison we find that the transitions 1, 2, and 3 show no XLD signal in the calculation in both the L_3 and L_2 edges. The only contributions to the XLD signal come from transitions 4 5 and 6 (e_g). It is notable that the t_{2g} signal leads to a negative XLD signal while the e_g transitions cause a positive contribution. Insofar, our experimental data agree quite reasonable with these calculations except the contributions of the transitions 1 to 3. This assignment can now be used for the interpretation of the XLD signals of our ALD samples. There is less agreement considering the relative intensities of the individual contributions. At the L_2 edge, for example the negative contribution of the t_{2g} is much more pronounced in the calculations compared to the experiment. This gives some evidence that not only the atomic multiplets have to be considered but there are covalent interactions between O2p and Ti3d states. It should be mentioned that this finding could only be derived from the XLD data and would not be detectable from an analysis of the XAS data alone.

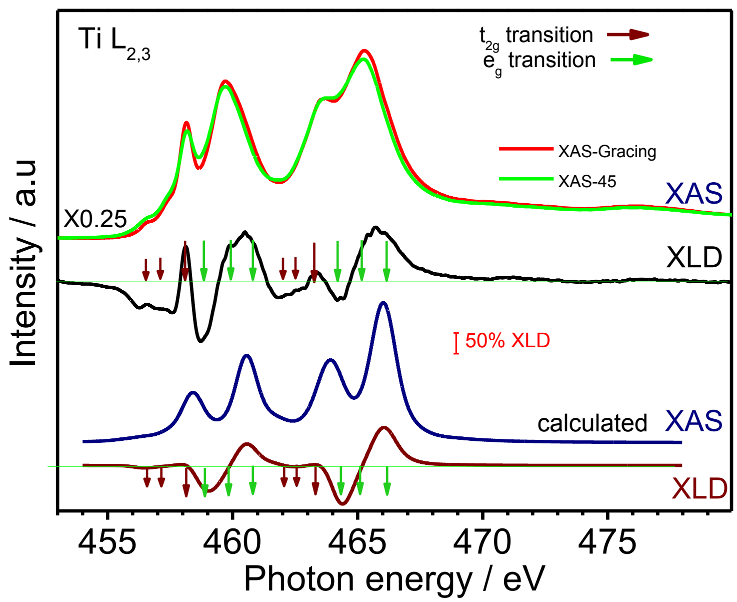

Figure 35: XAS and XLD of 200 ALD layers of TiO_2 at the Ti $L_{2,3}$ edge. The lower part shows the calculated spectra using CTM4XASwith labeling of main peaks. The individual transitions are marked by arrows (brown excitonic state/t_{2g}, green e_g).

A point must be cleared here, that the anatase has no natural dichroism as the rutile has. While in rutile the oxygen planes perpendicular to the c-axis are aligned in parallel planes causing an intrinsic dipole moment, the irregular Ti-O bond lengths in anatase disturb this kind of symmetry. Still there might be some distortions in the direct neighborhood of the Ti atoms also because of the irregular bond lengths and bonding angles but this seems to be not the case. However, the observed XLD effect at the Ti $L_{2,3}$ edge in anatase is very weak and almost negligible as it is much weaker when compared to the XLD signals of the ALD layers of TiO_2. The transitions associated to 4, 5, and 6 appear very weak with an intensity below 2%. Even more surprising is the fact that the transitions at the L_2 edge appear even weaker and are at the detection limit of our measurements. Very remarkable are the details of that anatase XLD signal. Here we identify primarily the transitions 1, 2, and 3, where the latter is the most prominent with an absolute intensity of around 5% (Table 13). There are two different explanations for that observation.

First, there might be electronic modifications in that polymorph based on the fact that in anatase the content of Ti^{3+} is extremely low (< 5%) while in the ALD films it is around 10%. However, these facts must be observable in the XAS data, and not in the XLD data. As a second explanation we argue that the dipole moments might cancel out almost perfectly as the nano-crystalline particles have a small size and a homogeneous distribution. May be we cannot conclusively decide on the origin of the XLD signal in anatase but we favor the explanation given in terms of the defect states (hole polaron) which we discuss in the section below.

Following this argumentation the sharp peak around 458eV in the absorption spectra of Ti $L_{2,3}$ edge is attributed to the transition into excitonic states which are within the electronic band gap. This assignment is supported by the compilation of the pDOS shown in Figure 42 of the section 3.2.2.4. There the first transitions of the Ti2p XAS spectrum are positioned within the gap. In addition they coincide with the photoelectron emission of gap states; this agreement is almost perfect and yields a defect state located about 1eV below the Fermi energy.

From the res-PES measurements, the polaronic band gap of TiO_2 is determined as shown in Figure 42. The polaronic band starts in the VB and extends into the band gap of the TiO_2 and the polarons in TiO_2 can change the Ti-O and O-O bond lengths. The details of the bond length in different polymorphs are given in the Table 2. Valentin et al. (139) showed in their theoretical calculation that the Ti-O bond length changes due to the formation of polarons, where the Ti-O bond length along the equatorial changes from 1.94 to 2.005 Å while along the axial the change in bond length is from 2.014 to 2.040Å. For amorphous TiO_2 such data are not available in the literature but our res-PES measurement shows that the ALD layers (amorphous) TiO_2 have polarons and that may result in the distortion of the octahedral due to the change in bond lengths of the Ti-O bonds. So it can be concluded, that the formation of polarons in anatase and amorphous TiO_2 may results in XLD due to the change in bond length of Ti-O bonds in both axial and equatorial directions.

This assignment is consistent with our calculations for the amorphous ALD layers shown in Figure 35, where the t_{2g} states cause a negative XLD signal while the e_g cause a positive XLD signal. The pre-edge features are not reproduced by the calculation at all. The assignment of the anatase XLD features is also consistent with this interpretation. Here, there is no natural dichroism in ALD as well as in anatase TiO_2, i.e. there are no octahedral distortions or their induced dipole moments average out by the random distribution of the nano-scaled crystallites. Consequently we observe just the polaronic defect levels within the gap. As such states can carry only a single spin moment, the transition probability at the L_3 edge is much higher. This explains why we observe smaller XLD in ALD layers and almost negligible intensity in anatase layers at the Ti L_2 edge.

3.2.2 Auger decay and polarons in TiO_2 films investigated by res-PES

3.2.2.1 Analysis of core level and VB spectra of three kind of TiO_2

In this chapter the differences in the electronic properties of the ALD layers, Anatase layers and single crystal rutile TiO_2 will be investigated and compared. The analysis will be done from the XPS, XAS and res-PES measurements performed on these samples.

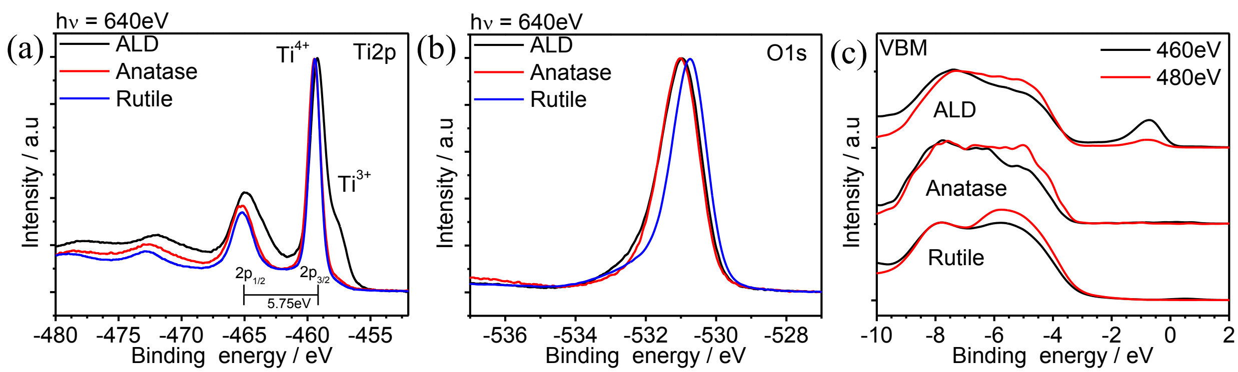

Figure 36: Ti2p (a) and O1s (b) core level and VB spectra (c) for ALD, anatase and rutile TiO_2 as labeled in the diagrams. The core level spectra were recorded with 640 eV of photon energy while the VB spectra are taken at two different photon energies (460 and 480eV) at and above the Ti2p resonance energy, respectively.

In Figure 36(a,b) PES spectra of Ti2p and O1s for ALD, anatase and rutile samples are compared. The $Ti2p_{3/2}$ peak intensities of respective TiO_2 films are normalized to one for better comparison. The Ti2p core level spectra show the same characteristic shape for all the three samples measured. But in case of ALD samples a distinct shoulder at lower binding energy is appeared which corresponds to Ti^{3+} states (see paragraph 3.1 and subsections). This shoulder shows that the ALD TiO_2 film has higher amount Ti^{3+} states compared to anatase and rutile single crystal samples. The $Ti2p_{3/2}$ peak is fitted with two sub-peaks to determine the Ti^{3+}:Ti^{4+} ratio in the TiO_2 samples. In the O1s spectra there is no visible difference in all the three samples excepting that the rutile spectra is shifted to lower binding energy by 200 meV. The O1s spectra have a tail toward the higher binding energy and this is due to adsorbed–OH ions on the TiO_2 surface. The Ti2p and O1s can be used in combination to determine the stoichiometry of the TiO_2 films and rutile single crystal. For the determination of the O:Ti ratio the contribution of –OH bonds to TiO_2 is avoided by fitting the O1s peak with two sub-peaks and neglecting the corresponding –OH sub-peak in the calculation. The quantitative values of Ti^{3+}:Ti^{4+} and the stoichiometry ratio of ALD, anatase and rutile TiO_2 are given in the Table 14.

The VB spectra of ALD, anatase and rutile samples are taken at 460 and 480 eV (Ti2p on and off resonance) photon energies and are shown in Figure 36(c). The on and off resonance energy are taken to examine the contribution of Ti3d states in the valence band. All VB spectra in Figure 36(c) are normalized to the intensity at 8 eV. The VBM of the three samples are determined extrapolating the slope of VB to zero and it is found to be around 3 eV. The details about the VBM positions are given in the Table 14. The widths of the VB in our measurements are found to be 5.5 eV which is in agreement with the literature values [(140), (141)]. In general it is considered that the VB is consisting of O2p states in metal oxides. The theoretical studies have been demonstrated that there are certain contributions of Ti3d states in the VB of TiO_2 having the highest contribution around 4 eV below the VBM [(140) (16)]. The VB at on (460 eV) and off (480 eV) resonance shows an appreciable difference. At the Ti2p resonance energy, the VB spectra show the contribution of Ti3d states. It can be seen in all these three samples that near the VBM the intensity of the VB spectrum taken with photon energy of 460 eV is lower and gradually increases deep into the VB. As found in theoretical studies the Ti3d states are negligible near the VBM region (140) but in our study we demonstrated that the 3d contribution already starts at the VBM edge. Nevertheless the Ti3d contribution near the VBM is less compared to the O2p contribution. The VB spectra are normalized at 8 eV bellow the Fermi level in order to check the contribution of O2p and Ti3d states in VB since recent theoretical calculations showed that Ti3d and O2p states far below the VBM have equal contributions [(43), (142)]. When the photon energy moves away from the Ti2p resonance energy the intensity of the VB near the VBM increases as seen for the spectra recorded with photon energy of 480 eV and this informs about the contributions of O2p states in the VB. Therefore the availability of both the Ti3d and O2p states suggests that the VB is consisting of hybridizations of both of these states (143).

Table 14: VBM, O:Ti ratio and Ti^{3+}:Ti^{4+} ratio of ALD, anatase and rutile samples.

	ALD	**Anatase**	**Rutile**
VBM (eV)	3.22	3.31	3.05
O:Ti Stoichiometry	1.97	1.96	2
Ti^{3+}:Ti^{4+}	0.08	0.04	0.027

In the VB spectra a peak in the forbidden gap is visible for ALD samples while in anatase and single crystal rutile samples this peak is absent. The in-gap state in the ALD sample is found around -0.9 eV with respect to the Fermi level. This position corresponds to the Ti3d defect states found in the band gap of TiO_2 [(56) (58)]. In the upper panel in Figure 36(c) the intensity of the in-gap state is higher when the VB is recorded at the Ti2p resonance energy. The intensity of the in-gap state decreases from 0.36 to 0.11 when the photon energy used is moved from 460 to 480 eV. The intensity increase of the in-gap state at resonance energy shows that the in-gap is due to Ti3d states. In the analysis of the Ti2p spectra, the ALD films show highest amount of Ti^{3+} states compared to the anatase and rutile samples. The exact amount of Ti^{3+}:Ti^{4+} ratio is given in the Table 14. The in-gap state intensity is proportional to the amount of Ti^{3+} states (144). In literature the appearance of the in-gap states is discussed as reduced TiO_2 (145).

3.2.2.2 Comparison of XAS of three polymorphs of TiO_2 at the O K-edge.

The XAS of TiO_2 ALD, anatase films and rutile single crystal at O K-edge are measured scanning over the photon energy range of 525 to 570 eV and collecting the current from the sample (total electron yield -TEY). The energy step here used is of 0.1 eV. For better comparison the XAS spectra are normalized to zero and one as atomic absorption coefficient.

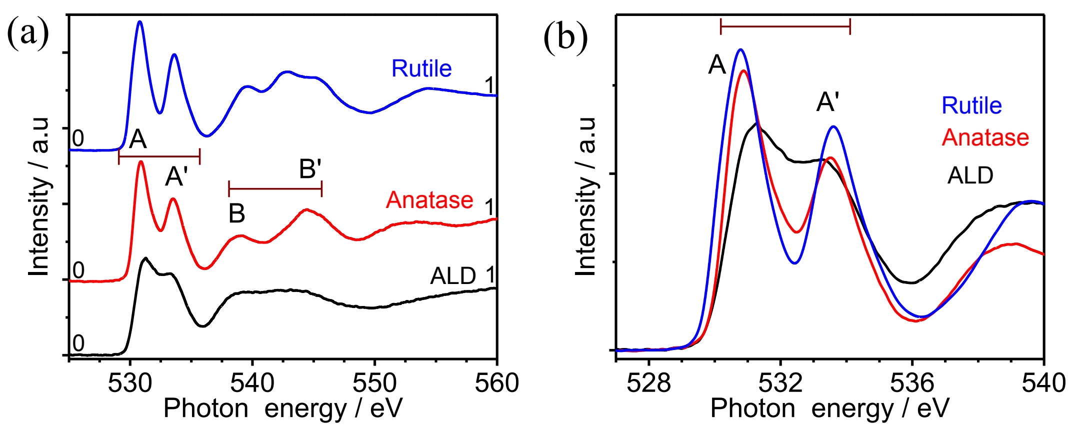

Figure 37: XAS spectra of ALD, Anatase and Rutile TiO_2 samples in the energy range of 525 to 560 eV (a) and the enlarged part of these spectra in the energy range of 525 to 540 eV (b). The spectra shown here are collected with total electron yield from the sample.

The X-ray absorption at the OK-edge reveals the density of unoccupied states of O2p states in the metal oxides (143), where electrons from the O1s orbital are excited into the unoccupied O2p states. The intensity of the XAS spectra depends on the available unoccupied states, or in other words the intensity can inform about the hybridization between O2p and Ti3d4s4p orbitals (143). The XAS spectra can be divided into two main regions, from 528 to 535 eV (peak A and A') and 536 to 548 eV (B and B') as shown in Figure 37(a). The peaks A and A' have different intensities for the ALD, anatase and rutile TiO_2 samples. These two peaks are not very distinct in the ALD samples while in the anatase and rutile samples these peaks are well separated. Moreover the higher photon energy region has more characteristic differences in all these three samples. The ALD sample has equal intense B and B' peaks while in the anatase sample the peak B has a lower intensity in comparison to the B'. The rutile TiO_2 has lower intense B peak and B' peak is divided into two more peaks.

The peaks A and A' at lower photon energy are addressed to the hybridization strength of O2p with the metal 3d states in the transition metal oxides (146), while the broad region (peaks B and B') at higher photon energies allows to determine the strength of hybridization between O2p and metal 4s4p states (147). The broadness of about 15 eV in the higher photon energy range indicates strengthens of the covalent bonding in TiO_2 polymorphs (148). The relative intensity of the A and A' region with respect to the B and B' region provides information about the bond strength of Ti3d-O2p and Ti4s4p-O2p hybridizations. In the ALD films the A and A' peaks have relative lower intensity with respect to B and B' than in the anatase and rutile TiO_2. This could lead to the conclusion that the Ti4s4p-O2p hybridization is stronger in ALD than in the other polymorphs. This fact is supported by the comparison of the peaks A and A' between the ALD, anatase and rutile samples shown in Figure 37(b). Here, the ALD sample has lower intensity than the anatase and rutile samples. Generally, stronger intensity corresponds to stronger hybridization between Ti3d-O2p states. So, the comparison of the O K-edge XAS spectra near the resonance energy show that the anatase and rutile polymorphs have stronger Ti3-O2p hybridization than the ALD layers but it's difficult to determine the amount of hybridization in each case. The XAS at the O K-edge of ALD films has a different profile than the anatase and rutile TiO_2 polymorphs. In addition, it owns ~~has~~ weak Ti3d-O2p and strong Ti 4s4p-O2p hybridization while in anatase and rutile it is the other way around. Vayssieres et al. have shown that TiO_2 nanoparticles have higher Ti4s4p-O2p than Ti3d-O2p hybridization due to the higher surface area (148). In case of the ALD sample the resulting XAS spectra can be due to the missing of a long range ordering of TiO_2 atoms in the thin films. As discussed above, the XAS spectra at the Ti $L_{2,3}$ edge also support this fact (149).

3.2.2.3 Res-PES of TiO_2 films at O 1s edge

In res-PES measurements at the O1s edge the photoelectron spectra are collected over a range of photon energy starting below the resonance and finishing at far resonance energy to investigate the oxygen-derived states in TiO_2. Near the resonance energy electrons from the O1s core level are excited into empty CB states. In this excitation process intermediate states are created and these intermediate excited states are involved in the oxygen derived states (150). In Figure 38 the res-PES measurements are taken with excitation energy scanned from 525 to 565 eV with step width of 0.25 eV over the initial state energy range of 0 to -60 eV for ALD TiO_2 film. This res-PES measurement gives information about the auger decay (constant kinetic energy), constant initial state (CIS), constant final state (CFS) and the XAS.

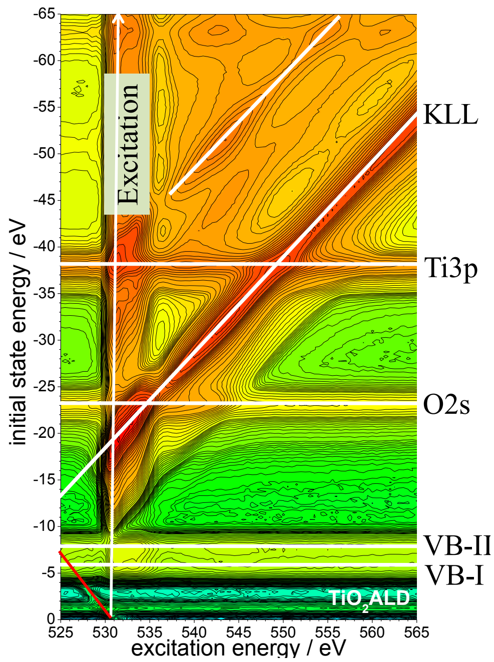

Figure 38: Res-PES of TiO_2 ALD films at the O 1s edge in the energy range of 0 to 65 eV (VB) regions. The photoelectron spectra are collected with step width of photon of energy 0.25 eV.

The two dimensional plot of the res-PES data at the O1s resonance photon energy allows us to study the different features at specific energies. With the increase in photon energy the intensity in the plot changes due to the emission of photoelectrons. The change in intensity diagonally near the resonance energy is resulted from the excited O1s core level electrons by the second order light from the monochromator illustrated by the red line in Figure 38. Significant increases in the intensity due to the spectral features are marked with white color lines. The increase in intensity in the range of -4 to -8 eV initial state energy (labeled with VB-I and VB-II) over the whole range of photon energy is due to the VB. The increase in intensity observed at -23 and -38 eV initial state energy corresponds to photo emitted electrons of O2s and Ti3p orbitals. At the photon energy of 530 eV, an increase in emission intensity is observed over the whole initial state energy region. This increase in intensity corresponds to the transition of electrons from O1s to the O2p states and is known as excitation states. Above the resonance energy edge the intensity increases with the increase in photon energy but at the same time the maximum intensity also shifts to the higher initial state energy with the increase in photon energy. This means that the emission line has a constant kinetic energy which is the feature of Auger lines. Two inclined white lines making an angle with the horizontal axis of 45º are the Auger decay lines. Such kind of Auger process is observed above the photon energy of 535 eV and more. The white line having a constant kinetic energy of 512 eV is addressed to the O-KLL Auger line. Under careful analysis other trends of increase in intensity can be observed in the photon energy range of 530 to 535 eV too. This is discussed in more detail in the following paragraph.

3.2.2.4 Multiple Auger decay at the O 1s edge.

Detailed res-PES intensity profiles are shown in Figure 39; here the res-PES data of anatase and rutile TiO_2 are shown also. With both the increase in photon energy as well as in initial state energy higher intensity is clearly visible correlating this intensity profiles to Auger processes. Apart from the main Auger line (KLL Auger) along 45° with respect to the horizontal axis, two more intensity profiles are observed. These two high intensity profiles are found in the photon range from 530 to 535 eV and marked with two white lines at angles of 56º and 67.5º with the horizontal axis. These lines correspond neither to constant initial state energy nor to constant kinetic energy. Based on this fact the idea that these higher intensity contributions are due to normal photoelectron emissions or normal Auger processes can be discarded. In addition, some other intensity profiles can be observed in the res-PES maps. In particular two broad Auger lines appear in the higher photon energy range between 532 and 542 eV having angles of 51º and 34º with the horizontal axis. The Auger lines with different angles than 45º inform that there are involved processes other than the normal KLL Auger.

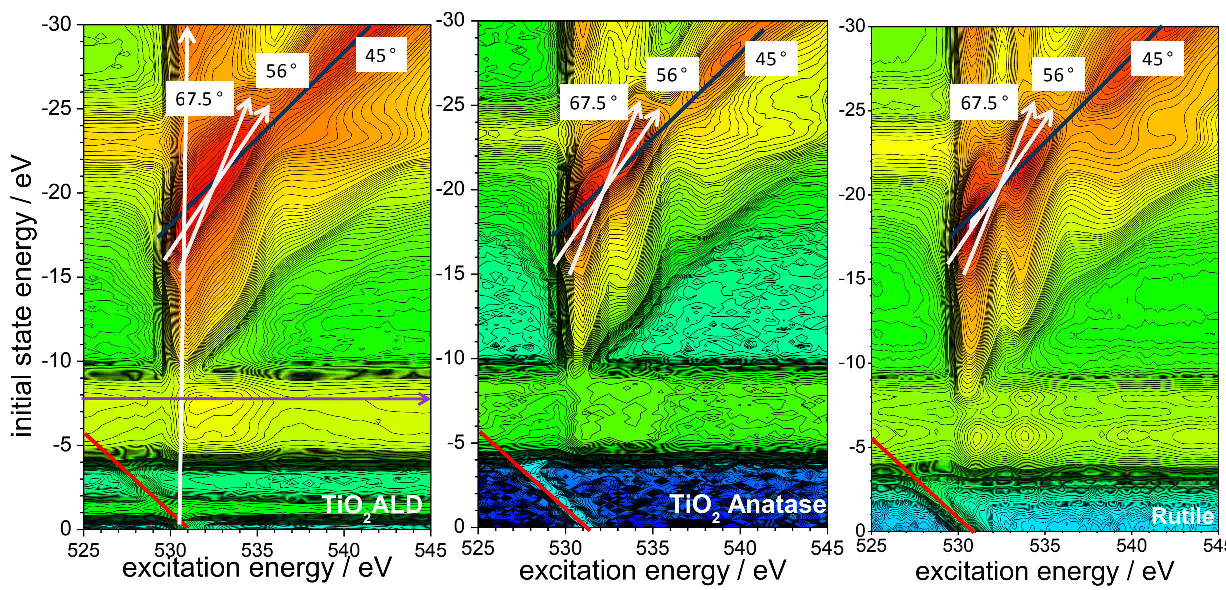

Figure 39: Res-PES map of TiO_2 (ALD (left), anatase (middle) and rutile (right) samples) taken at the O 1s edge. The intensity profiles in the res-PES map are denoted by the lines and have different angles with respect to the horizontal axis.

The different Auger lines observed in the res-PES map at the O1s edge can be explained on the basis of multiple hole Auger decay processes as suggested by M. Richter in his Ph.D work (101). The identification of different Auger processes can be determined from the angle of the intensity profile in the res-PES map. The angle α can be defined as given in equation (3.1).

$$\pm\Delta = \pm\frac{\Delta_{initial}}{\Delta_{exc.}} = \tan(\pm\alpha) = \cot\left(\pm\frac{\pi}{2^n}\right), \tag{3.1}$$

where n is the number of holes in the final state, Δ_{intial} is the change in initial state energy and $\Delta_{exc.}$ is the change in excitation energy for the intensity profile in the res-PES map.

When the n=1,2 (one hole and two holes final state) the α values are 0º and 45º corresponding to the participator and spectator decay respectively. For higher values of n (3,4) the Auger process will be consisting of both the participator and spectator decay (151). For different n values the respective α and their decay processes are given in Table 15.

Table 15: Multiple Auger decay processes with the number of final state hole (n), angle of the intensity profile in res-PES map and the respective decay process via participator (P) or spectator (S) electrons.

Final state hole (n)	Angle of inclination (α)	Decay process
1	0°	Participator
2	45°	Spectator
3	67.5°	Participator + Spectator
4	78.75°	Spectator + Spectator

In the res-PES maps of the ALD and anatase samples the Auger lines have the same profiles near the Fermi level. In the rutile single crystal the intensity profiles are different. In the rutile sample there is only a slope in the intensity profile near the resonance excitation energy with an angle of 78.5º which corresponds to the 4 hole Auger decay, but the 4hole auger process is also accompanied by the 101.5 º and this feature is absent here. So in rutile TiO_2 there are no 4 hole Auger decay process. The intensity profile near the excitonic transition in rutile is due to the onset of the transition, while this feature is absent in the data of the ALD and anatase samples. The intensity profile of the ALD and anatase samples in this range (energy range 530 to 532 eV) are broad. Apart the from above mentioned angles in Table 15, there are other intensity profiles in the res-PES maps making different angles with the horizontal axis like 34°, 51° and 56° as mentioned above. Here other processes than listed in Table 15 might be running.

The concept of resonance photoelectron spectroscopy resulting in participator (P) and spectator (S) Auger decay processes has been described in the previous section 3.2.2.3. In this section multiple Auger processes involving combinations of spectator and participator Augers decays will be described. The decay process involving (S+P) can be seen in the res-PES map with an angle of inclination of 67.5º and results in three holes in the final (valance) state. On the other hand the intensity profile with 78.75º inclinations has four holes in the final state and is due to the combination of two spectator (S+ S) processes.

The three hole (S+P) Auger process have been investigated in metal oxide as well as in carbon systems [(152), (153)]. This phenomenon needs higher density of core holes and this can be obtained near the resonance energy edge. The three hole auger process occurs within 2 eV from the Fermi energy. Moreover the res-PES measurements are done with synchrotron light; so due to the high intensity of light the decay process can be observed clearly. Apart from the experimental needs the material property should satisfy three more requirements.

i) The material should have localized states in the band gap so that photo excited electrons at resonance can relax via these states from the excited conduction band states.

ii) The resonantly excited electrons which relaxed via the localized states must have higher life time than the spectroscopic decay.

iii) The third requirement is the availability of highly mobile and delocalized electrons (Bloch wave function) in the valence band. These electrons will recombine with the excited holes in the core state. Generally these kinds of valence electrons are observed in covalent materials.

The three hole final state Auger process can be described using the schematic diagram in Figure 40. In step (i) the O1s core electron is excited by the resonating photon energy into an unoccupied state in the conduction band. The excited electron in the conduction band relaxes into the localized state in the band gap as shown in the step (ii). The electron in the localized state is stabilized by the valence band hole forming an exciton. Generally, the excitonic electrons have higher life time than the excited electrons in the conduction band.

In the next step the electron from the valence band fills the core hole and the hole V_1 is formed in the VB (step iii). The energy due to the transition of the valence electron to the core hole is transferred to the next electron in the VB. The electron from the VB is then emitted as KLL auger decay resulting in the hole V_2 (step iv). This phenomenon leads to the emission of a spectator electron (spectator Auger decay) leaving behind two electrons in the final state (valence band). The spectator Auger decay can be seen under an angle of 45º in the intensity profile of the res-PES map at the O1s edge.

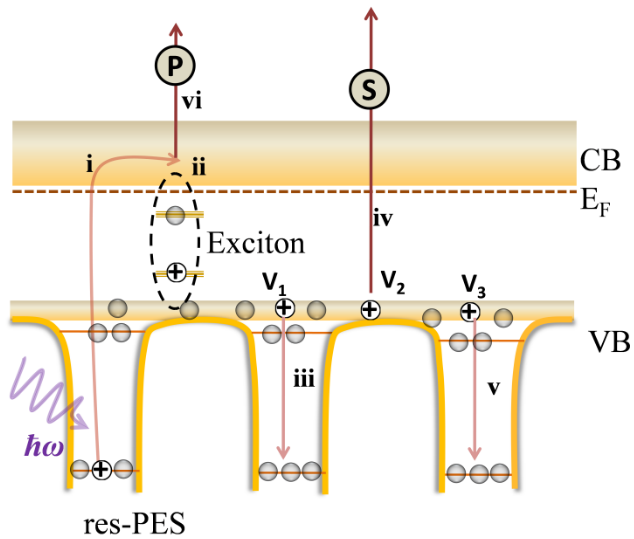

Figure 40: Schematic representation of the (S+P) Auger process at the O 1s edge in TiO_2 layers. The steps i-vi explain the process of resonant photoelectron emission and the three hole (S+P) auger decay. The V_1,V_2,V_3 are the final state holes in the valence band. The resultant excitonic state is a trap states. The excitation of the core electron and the formation of excitons are shown in steps (i, ii). The second process leads to the normal KLL decay in the steps (iii and iv). Finally the steps (v and vi) show the emission of the participator electron from trap level.

In the next process the excited trapped electron is emitted as participator. Since the initial core level hole is filled by the electron from the VB, the trapped electron is emitted by forming another hole in the VB. Here, the VB electron will fill one of the core holes created by another resonant photoemission and forms the hole (V_3) in the VB. The energy due to this transition is transferred to the electron in the excitonic state and the excitonic electron will be emitted as participator decay with lower kinetic energy than then KLL Auger electron. This process is illustrated as steps (v and vi) in Figure 40 .

All the above described processes occur simultaneously to result in an Auger decay emitting both spectator and participator electrons. So the whole process of (S+P) electron emission involves the resonantly excitation of core holes and their refilling by VB electrons.

The res-PES measurements at the O1s edge are used to identify different Auger decay processes in ALD, anatase and rutile TiO_2. We identify the 2h (S) and 3h (S+P) Auger decay processes having angles of inclination of 45º and 67.5º respectively in different polymorphs of TiO_2. Another intensity profile observed near the resonance photon energy under an angle of inclination of 56º cannot be explained by 2h or 3h Auger decay processes. There are more intensity profiles found in carbon systems having angles more than 90º and these are corresponding to the 'negative' Auger process like in graphene system the -4h Auger process is attributed to an angle of 101.25º (154). The Auger process making an angle 56º can be defined as the -3h Auger process involving a two photon system (-3h/2photon). The Auger decay process depends on the strength of hybridization as well as on the in-gap states in TiO_2. The -3h Auger decay start after resonance energy and extend into 5eV away from the resonance.

From the res-PES map the amount of different auger decay processes can be estimated by careful analysis. For quantification we use curve fitting technique for VB spectra at different photon energies and identify the 2h, 3h and -3h/2photon Auger decay processes. In the res-PES map it can be noticed that the 3h and -3h/2 photon Auger processes occur near the resonance energy while the 2h Auger process is continued to the far resonance energy. So, to determine the different contributions the following methodology is used:

- The Auger decay far above the resonance energy is mostly due to the 2 hole decay process.
- The spectrum at the photon energy 563eV is taken and is drawn against the KE.
- This spectrum is normalized by subtracting the VB spectrum well below the resonance energy.
- The peak due to the 2 hole decay is fitted with multiple peaks and the ratio of the individual peak areas to the main peak is determined.
- Another spectrum near the resonance energy is taken and the VB contribution is subtracted from this spectrum too.
- The remaining spectrum is again fitted including the 2h Auger spectrum obtained at the photon energy of 563 eV. Here we assume that the 2h Auger intensity is same throughout the whole photon energy range.
- The rest of this spectrum is fitted with 3 more peaks, which will show finally the relative contributions of 3h, -3h/2 photon and the excitonic emission.
- Above resonance energy 6 spectra are taken with 1 eV interval of photon energy and the whole above described procedure is repeated to determine the different Auger contributions in the resonance energy range.

In Figure 41 an example spectrum near resonance (531 eV) for the illustration of the above described procedure is shown. The Auger peak is fitted into four peaks to identify the 2h, -3h/2photon, 3h and excitonic contributions in the Auger decay processes. The quantifications of different Auger processes are given in Table 16 for ALD and anatase TiO_2 samples. It shows that the contribution of 2h Auger decay is highest among all others in all these three polymorphs ALD, anatase and rutile. Near the resonance energy the 2h Auger process contribute 35-40% of total Auger decay while the -3h/2photon has contribution around 30% and 3h has contribution around 15%. From the table it can be marked that the when the photon energy moves away from the resonance energy the 2h Auger contribution increases and while that of 3h and -3h/2photon sharply decrease. This confirms that the multiple Auger decay process only occurs near the resonance energy due to the formation of excitons and their prolonged life time. In addition the -3h/2ph Auger intensity near the resonance energy is higher for ALD layers than the anatase layers. The -3h/2ph is strongly related to the in gap state (defect state) in the TiO_2 and the higher amount of this Auger intensity implies the higher amount of defect states. The quantification of Auger process from res-PES and the VB study in Figure 36 shows that the ALD layers has higher amount of defect states in comparison to the anatase and rutile TiO_2.

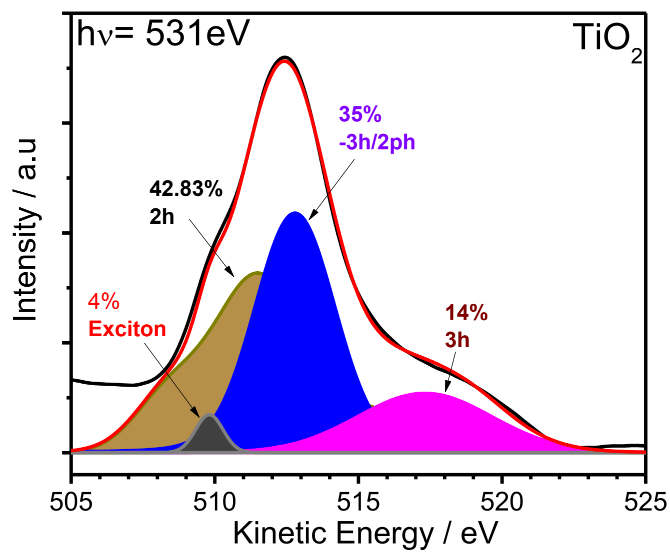

Figure 41: Determination of the Auger decay contributions proceeded by the procedure described above. The spectrum taken at 531 eV photon energy from the res-PES map at the O1s edge is fitted into 3 peaks and a non-uniform peak showing only the contribution of the 2h Auger decay while the other 3 peaks contribute to exciton, -3h/2ph and 3h Auger decay. Here a curve for an ALD sample is shown exemplarily.

Table 16: Quantification of multiple Auger decays in ALD and anatase samples. The values are determined by fitting the individual curves at the given photon energy as described in text.

Photon energy (eV)	**ALD**			**Anatase**			**Rutile**		
	2h%	-3h/2ph %	3h%	2h%	-3h/2ph %	3h%	2h%	-3h/2ph%	3h%
530	35.4	34.5	12.3	44	24.8	16	42	25	17.5
531	42.8	35	14	39.5	30.5	15.5	35	24.6	18
534	71.8	12.5	8.7	47.6	26.2	15	61.5	25.3	13
536	67.4	15	7	71.2	18	9	68	26.5	12.4

3.2.2.5 Partial density of state (pDOS) and band gap determination

In Figure 42 the partial electron yield (PEY) of oxygen and titanium and the valence band (VB) at 455.2 and 526 eV are plotted with reference to the Fermi level for the ALD, anatase and rutile TiO_2 samples. The combination of the normalized VB and the PEY in the CB can deliver the band edge position and the band gap of TiO_2 layers when plotted with reference to Fermi level. In Figure 42 the upper panels show the occupied VB and unoccupied CB and the lower panels depict the CIS spectra to get information about defect states. The CIS is taken at the highest intense VB peak (at -5 eV initial state energy) in order to probe the in-gap defects which are considered in literature as oxygen vacancy (155). Another CIS at -10 eV of initial state energy is taken to investigate the charge transfer state between O2p-Ti3d4s. The CIS data are taken from the res-PES measurements at the O1s edge.

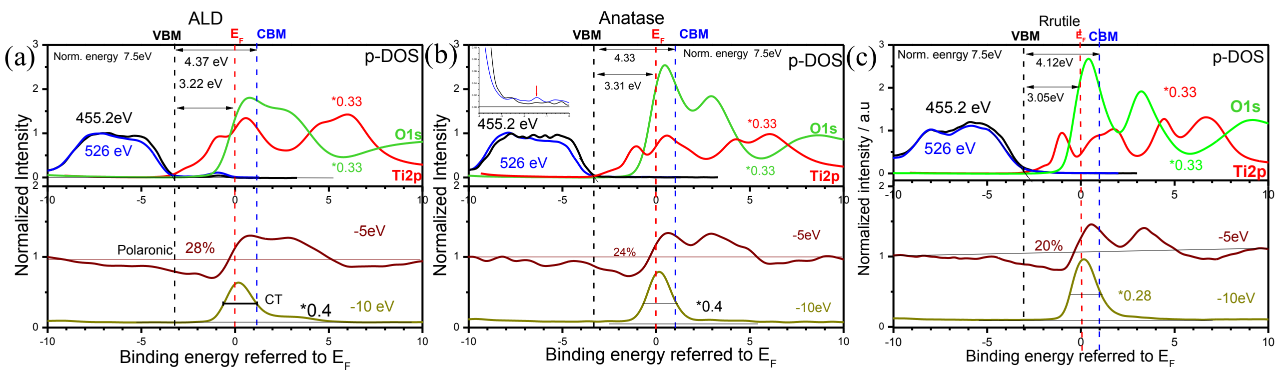

Figure 42: Partial density of states (p-DOS) of O and Ti in VB and CB for ALD (a), anatase (b) and rutile (c) TiO_2 samples. The p-Dos of O and Ti in CB are deduced from the integrated res-PES measurements over the whole photon energy. For the VB p-DOS the VB are taken below the O 1s and Ti 2p resonances, respectively, and normalized to one at -7.5 eV. The same scaling factor is then used to normalize the PEY of O1s and Ti2p, however these data are multiplied by 0.33 in each case for better illustration. The VB and the CB are aligned by taking the core level and aligning with the Fermi level. The lower panel shows the CIS spectra taken at -5 eV and -10 eV.

The PEY at the Ti2p and O1s edges are determined from the res-PES measurements for three different kinds of TiO_2 samples (ALD, anatase and rutile). The PEY is obtained by the summation of VB spectra over the resonance photon energy range. Since the resonant photon electron spectroscopy operated through an intermediate state (unoccupied state of CB) (95), the intensity of the photo-emitted electrons will be proportional to the number of electrons residing in the intermediate state after excitation from the core level to the unoccupied state. Therefore the integration of res-PES map over the total photon energy provides the PEY of the Ti2p and O1s edges. Consequently, the PEY from the res-PES maps are the replica of the partial density of states (p-DOS) of Ti and O in the unoccupied states.

The VB spectra are taken at two photon energies below the resonance energy of Ti2p (460 eV) and O1s (531 eV) to exclude the contributions from the excitons at resonance. For the quantification and better comparison purpose, the VB is normalized to 1 at -7.5 eV. The PEY data are normalized by the same normalizing factor as used for the VB and then multiplied by a factor of 0.33 in order to put the CB and VB in the same scale. The combination of PES at off resonance energy and the PEY can be helpful to deduce the VBM and CBM along with the contribution of pDOS due to O and Ti in VB and CB respectively. The CIS spectra at -5 and -10 eV are also normalized by the same factor as used in case of VB and are also aligned with respect to the Fermi level.

The VBM of ALD, anatase layers and rutile TiO_2 can be determined from the extrapolation of the VB to the horizontal binding energy scale at zero intensity. The VBMs are found to be at -3.22, -3.31 and -3.05 eV below the Fermi energy for ALD, anatase and rutile TiO_2 samples respectively. In the ALD films the in-gap peak appearing at -0.9 eV corresponds to defect states and this in-gap state in anatase layer is very negligible small (as shown in the inset of Figure 42(b)) while in rutile it is not visible at all. The CBM is determined by considering the FWHM of the CIS spectrum taken at -10 eV initial state energy and is found to be at 1.15, 1.02 and 1.07 eV with reference above the Fermi level for the ALD, anatase and rutile samples respectively. Hence the band gap of ALD, anatase and rutile layers is found to be 4.37, 4.33 and 4.12 eV respectively as listed in Table 17.

Table 17: VBM, band gap, O/Ti ratio, pDOS of O1s and Ti2p in CB, relative intensity of polarons, and relative intensity of charge transfer (CT) states for ALD, anatase and rutile TiO_2 samples. All these data are collected from the res-PES measurements at the Ti2p and O1s edges.

		ALD	Anatase	Rutile
VBM (eV)		3.22	3.31	3.05
Band gap (eV)		4.37	4.33	4.12
O-Ti elemental ratio		1.97	1.96	2
pDOS	*O1s*	7.62	9.25	7.8
	Ti2p	6.64	4.17	4.10
Relative intensity of Polarons		28%	24%	20%
Relative intensity of CT states		64%	81%	97%

The VB intensities at two different photon energies of 455.2 and 526 eV close to the Ti2p and O1s resonances of respectively, are the same but show a small difference near the VB edge (near VBM region). The VB spectra taken with photon energy of 526eV have lower intensity compared to the 455.2eV data and show the influence of polaronic states. This can be seen in the lower panels of Figure 42. The polaronic states starts at around -7.5 eV and extend up to the Fermi level. The polaronic state intensity also increases towards the VBM and therefore the VB intensity decreases when excited with the O1s near-resonance photon energy. The equal intensities in the VB spectra recorded with Ti2p and O1s edge photon energies show the availability of both the Ti3d and O2p states. This suggests that the VB is consisting of the hybridizations of both of these states. The VB spectra at the Ti2p resonance (460 eV) and off resonance (480 eV) in Figure 36(c) show the presence of Ti3d states in the VB. It already starts at the VBM edge and has equal intensity like the O2p spectra about 4 eV below VBM edge. The equal contribution of Ti3d and O2p states far below the VBM is also shown in recent theoretical studies [(43), (142)].

The CB information is obtained from the pDOS of the O1s and Ti2p. The Ti-derived pDOS starts right from the edge of the VBM; that means at around 3 to 3.2 eV below the Fermi level (depending on the kind of TiO_2 sample) and extend into the conduction band. The Ti2p XAS (PEY) spectra are due to the occupation of photo-excited electrons from the Ti2p core level to the hybridized O2p-Ti3d4s states in the conduction band. The in-gap states of the Ti2p XAS are due to the emission of photoelectron from the Ti3d4s state to the $Ti3d^14s^1$ in the gap. The evidence of $Ti3d^14s^1$ can be drawn from the LMV Auger decay at the Ti L edge in the Ti2p res-PES map (refer to Figure 29). The Coulomb interaction between the localized $O2p^5$ sates and the $Ti3d^14s^1$ may be the stabilization factor for this in-gap state. Jakub et.al, also observed the localized Ti3d state in the band gap of TiO_2 in their experiments based on hard X-ray RIXS (142). The Ti3d states in the gap are stabilized by the Coulomb interaction from the Ti3p hole (95). In the present case the electrons are excited from the Ti2p level leaving holes in the core. The core hole may be filled by the valence electron and form localized $O2p^5$ states. As a result of the Auger decay the localized hole at O2p stabilizes the in-gap state $Ti3d^14s^1$. The same effect is also found in ZnO (156). Along with the localized $Ti3d^14s^1$ in-gap states we also observed a peak at around 1eV below the Fermi level in the VB spectra in particular for the ALD sample. This in-gap state shown in the VB spectra corresponds to the Ti3d states. In the ALD samples the Ti3d state and the localized $Ti3d^14s^1$ states have the same position in the gap while in anatase and rutile samples the Ti3d state is not detected. The appearance of the Ti3d states in the ALD sample could be due to the presence of higher amount of Ti^{3+} states compare to the antase and rutile samples (refer to Table 14).

The pDOS of the O2p contribution in the CB can be determined from the res-PES measurement at the O1 edge. The O1s PEY spectra start around 1eV below the Fermi level and the intensity increases into the conduction band in all three samples of TiO_2. From the existence of O2p states within the band gap the presence of both localized and delocalized O2p states can be inferred. The presence of a localized O2p band in the band gap is associated with the $O2p^5$-$Ti(3d4s)^1$ hybridization. The stabilization of this state could be due to the Coulomb interaction between the VB hole (O2p band) and the electron in the Ti3d4s band. The presence of O2p5 state in the VB refers to the presence of unoccupied O states in the conduction band.

The lower panels in Figure 42 include the polaronic and charge transfer (CT) states taken at CIS of -5 and -10 eV respectively. In the CIS spectrum at -5 eV resonance and anti-resonance profile are observed over the scanned photon range. The anti-resonance stars already in the VB region and its intensity increases in the band gap. The process of anti-resonance can be explained on the basis of interaction between two similar kind of outgoing electron wave functions and is known as Fano process [(157), (158)]. In the previous section we discussed the local formation of the $O2p^5$ state by the removal of one electron. The $O2p^5$ state forms the polaronic state and can decay to $O2p^4$ by direct photoemission. The final $O2p^4$ state can also be achieved by an indirect photoemission channel where an $O2p^6$ intermediate state is formed by filling up an $O2p^5$ state followed by decay into the final state by auto-ionization process. These two resulting electrons have wave functions with different phases and their interaction gives rise to the Fano like profile. The Fano profile can have different q values. In the present case the samples show a 3h Auger decay; so their Fano profile has a q value greater than 1 (>1). The relative intensity of the polaronic states is defined by normalization of the CIS curve with the intensity at -7.5 eV in the BV. The minimum of anti-resonance in the CIS is taken as the intensity of the polaronic states in each sample measured and is presented in Table 17.

The CIS taken at -10eV shows a peak at the O1s resonance (at the Fermi level). This represents a charge transfer (CT) of an electron from an O2p states to an empty metal state. The analysis of the res-PES map shows that the 3h Auger decay starts just above the -10eV. The 3h Auger decay takes place with the presence of unoccupied metal states in the band gap. The VB electrons of the O2p states is transferred to the unoccupied TI3d4s states in the bad gap and decays with 3h final states. The Ti derived pDOS is found to be in the band gap about 1eV below the Fermi level to which the electrons move from the $O2p^5$ in the VB state. Indeed the CT states are commonly observed in transition metal oxides as well as in other metal oxide systems like Ga_2O_3 [(150), (159)]. The transfer of electrons from O2p states into Ti3d4s unoccupied states forms a band through which the electrons transfer. From the CIS at -10 eV the width of the CT can be determined by taking the FWHM of the CT peak and the upper end of the FWHM is considered as the CBM in this analysis. The relative intensities of the CT states for ALD, anatase and rutile TiO_2 are given in the Table 17.

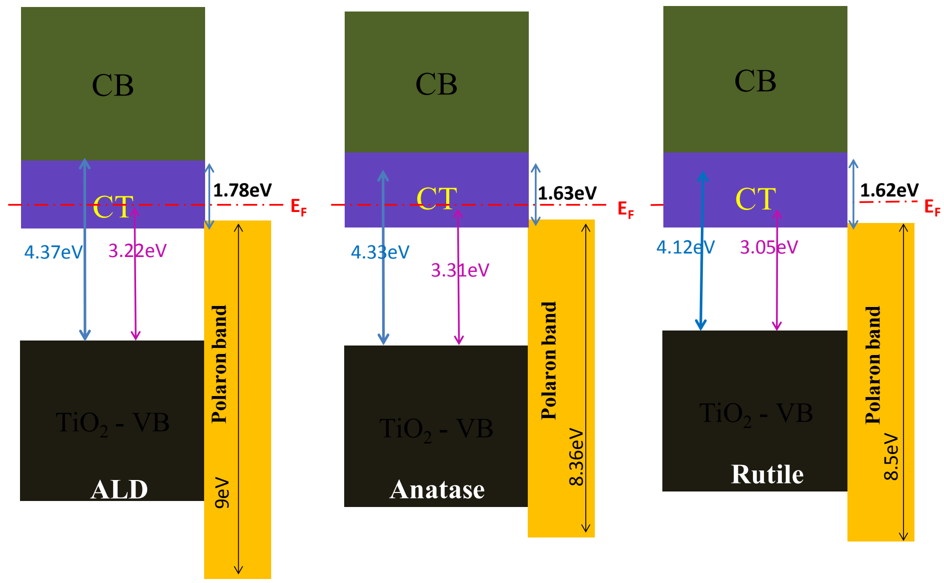

Figure 43: Schematic band diagrams of ALD (left), anatase (middle) and rutile (right) TiO_2. The VBM, CBM, CT and Polaron bands are determined from the res-PES map. The respective poisitions are aligned with respect to the Fermi level.

The information about the VB and the contributions of Ti and O derived states in the CB are obtained from the res-PES measurements. The pDOS of O1s and Ti2p show the contributions of both the metal and oxygen states in the conduction band while the contributions in the VB are calculated from the PES. The VB and the pDOS are aligned with respect to the Fermi level to determine the band gap of TiO_2. The VBM position is clear but the CBM location determination by photoemission spectroscopy is a matter of debate. In the present case the FWHM of the charge transfer is used to identify the CBM of TiO_2 since the charge transfer takes place between the O2p states and the unoccupied metal states in the gap. So the FWHM can be considered as a point where the CBM is loacated. A schematic presentation of the band edge positions and the band gap including the CT and polaron bands obtained from the analysis of VB and pDOS shown in Figure 42 is given in Figure 43.

3.2.2.6 Determination of CNL in TiO_2

The CNL energies for TiO_2 are calculated by the weighted oxygen and metal density of states in the valence and conduction bands [(103), (104)]. In our analysis we obtained the pDOS from the res-PES measurements at the O1s and Ti2p edges. From the VB spectra we determine the DOS of Ti and O contributions to the VB. Since the analysis suggests that the VB is consisting of O2p-Ti3d hybridization states, the contributions of the Ti and O are consider as equal to each other in VB. The determination of the weight of Ti and O DOS in the conduction band is rather trivial. The PEY from the res-PES measurements can be used to quantify the Ti and O contributions in the CB. To determine the CNL we used values such as band gap, Ti and O pDOS in VB and CB resolved form our analysis of the res-PES measurements. The width of the CB is determined by taking the ionization potential (IP) from the literature since the electron affinity has different values ranging from 4-6 eV in the literature. The IP of anatase and rutile is 8.30 and 7.83 eV respectively (160). In addition our ALD samples do not have any defined polymorphs so we consider the I.P of ALD TiO_2 layers as 8 eV. The CNLs are calculated using equation 2.29 and are presented with respect to the vacuum level.

Table 18: CNL of the ALD, anatase and rutile TiO_2 samples with respect to the vacuum level determined from the res-PES measurement data.

	ALD (eV)	**Anatase (eV)**	**Rutile (eV)**
CNL without CT	7.2	6.77	7.06
CNL_{CBM}	7.61	7.56	7.2
CNL_{EF}	7.48	7.44	7.14
$CNL_{CBM}^{(only\ Ti)}$	6.37	6.00	5.95
$CNL_{EF}^{(only\ Ti)}$	6.73	6.33	6.17

Table 18 shows the CNLs for ALD, anatase and rutile TiO_2 samples calculated using the VB, CB states from the res-PES data and the IP from literature as mentioned above. In our study we found that the CNL is around 7.5 eV below the vacuum level while in theoretical work the CNL of TiO_2 is located around 6.1 eV (2.2 eV w.r.t VBM) (104). In the theoretical work the band gap of TiO_2 is considered as 3.2 eV and the electron affinity was taken as 4 eV while in our measurement the band gap is around 4.3 eV. Other than the band gap the density of states is an important factor to determine the CNL in metal oxides. In our analysis TiO_2 have both Ti and O unoccupied states in the gap around the Fermi level. However, the unoccupied localized states observed in our res-PES data are not considered in theoretical calculations. So, to determine the extent of density of states in the CB we took the pDOS starting from different energy positions considering the same CBM. On considering the CB states starting from the Fermi level (CNL_{EF}) the CNL shifts by 150 meV towards the vacuum level in comparison to the CLN_{CBM}, where the CB states taken into consideration start at the CBM. When the CT band is excluded in calculation (CNL without CT) the CNL further approaches the theoretical value.

It is a general practice that the CB of metal oxides is considered to be based on the metal derived states, so in the CNL calculations of metal oxides only contributions of metal states are considered. When we only include the Ti pDOS contribution in the determination of the CNL ($CNL_{*}^{(only\ Ti)}$) the values are much closer to the theoretical values of 6.1 eV for the anatase and rutile TiO_2. In contrast, in the ALD sample the analysis shows that it contains higher amount of titanium derived states in the CB. With the help of res-PES measurements we can probe into self trapped polaronic states and this creates O2p empty states in the CB.

The res-PES measurements and analysis can provide different qualitative and quantitative electronic properties of TiO_2. This method is useful to determine the electronic band gap of any material systems where the optical spectroscopy cannot be used. The positions of defect or in-gap states are identified by res-PES measurements. A single measurement is used to determine the pDOS in VB as well as in CB with the quantitative contribution of oxygen and titanium derived states. The observation and quantification of the polaronic as well as the CT bands are possible. The identification of individual O and Ti pDOS in the VB and CB enables us to calculate the CNL experimentally. Furthermore, we point out that the theoretical calculation of the CNL does not consider the oxygen derived localized unoccupied states that contribute to the pDOS of the CB.

3.3 TiO_2 protective layer for Si photocathodes

In this chapter the ALD grown TiO_2 films are used as protective layer against photoelectrochemical corrosion. The relation between the spectroscopic properties of TiO_2 and their effect on TiO_2/Si photo cathodes are established. Firstly, the effect of TiO_2 on the stability is examined under photoelectrochemical environment. Then the TiO_2 is used to control the interfacial SiO_2 thickness and the effect of SiO_2 thickness onto the photoelectrochemical performance is checked. Finally, the spectroscopic properties of ALD grown TiO_2 will be related to the photoelectrochemical properties of TiO_2/Si photoelectrodes.

Silicon as a photocathode itself presents lower photo to current conversion ability due to the lower quantum efficiency, i.e. the photogenerated electrons which react with the electrolyte cannot compete with the recombination of the photogenerated electron hole (e^-/h^+) pairs at the interface of the p-Si / electrolyte (161). Due to the higher recombination of photo-generated e^-/h^+ pairs the output photovoltage of the p-Si photocathode is lower and has a higher over potential to generate hydrogen. Though the p-Si photocathode is thermodynamically more stable against reductive photocorrosion the formation of SiO_2 at the interface to Si cannot be avoided which cause a higher recombination rate of e^-/h^+ pairs (162). Therefore, the combination of a large band gap semiconductor with a small band gap semiconductor in one photocathode system may allow overcoming the drawbacks of each material. Hence we introduced here heterojunctions of silicon (band gap of 1.12eV) and titanium dioxide (~ 4.3eV) which will allow achieving higher stability and separation of charge carriers.

The TiO_2 ALD layers are grown using TTIP as described before in section 3.1 on p-type Si of resistivity 10-20 Ωcm. The (photo) electrochemical measurements were performed using a VERSSTAT 4 potentiostat with a bottom cell as the electrochemical cell, Ag/AgCl reference electrode, a Pt counter electrode and the silicon based working electrodes. For all presented figures the potential scale was converted into the reverse hydrogen electrode (RHE) according to eq. 2.30.

$$E_{RHE} = E_{AgCl} + 0.059pH + E^0{}_{AgCl}\,, \tag{3.2}$$

where $E^0{}_{AgCl}$= 0.197 V.

The scanning rate of 50mV/s was used for the cyclic voltammetry experiments; the area of working electrode was always kept at $0.38cm^{-2}$. The 0.5M phosphate buffer solutions of pH 7 and 0.1M H_2SO_4 of pH 1 are employed to study the properties of the photocathode. The used electrolytes were purged for about 20 minutes with N_2 in order to minimize the oxygen gas content. For the photoelectrochemical studies a visible light source (Euromax fiber optic light source EK1) with light intensity of 40 $mWcm^{-2}$ and 610 nm wavelength was used.

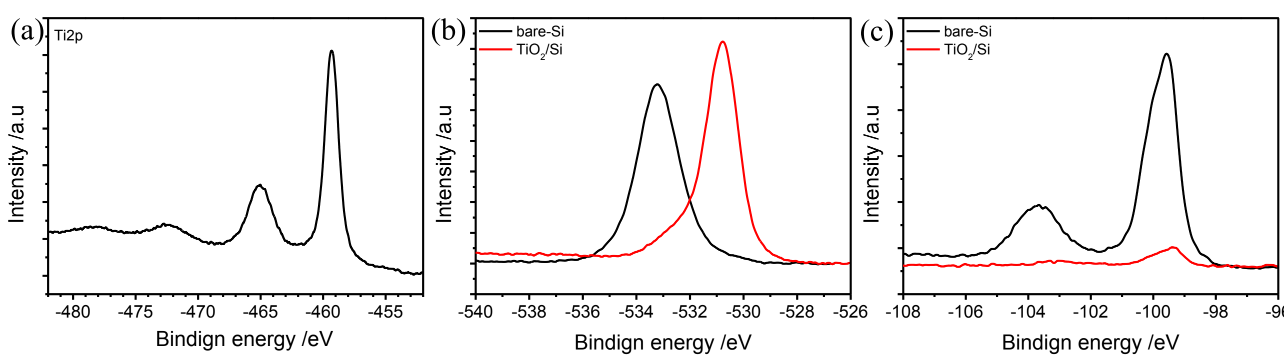

Figure 44: Deposition of TiO_2 on Si by ALD using TTI precursor. The PES spectra are recorded for the Ti2p (a), O1s (b) and Si2p (c) core levels. In part (b) and (c) the spectra of the Si substrate and the TiO_2 covered Si are shown.

Figure 44 shows the successful deposition of TiO_2 on Si substrate. The shift in O1s in Figure 44(b) and the decreases in intensity of Si2p peak in Figure 44 (c) show the deposition of TiO_2 and the thickness of the film. In the previous section on ALD deposition of TiO_2, the thickness of TiO_2 layer deposited on Si for 200ALD cycles is found to be 3 nm.

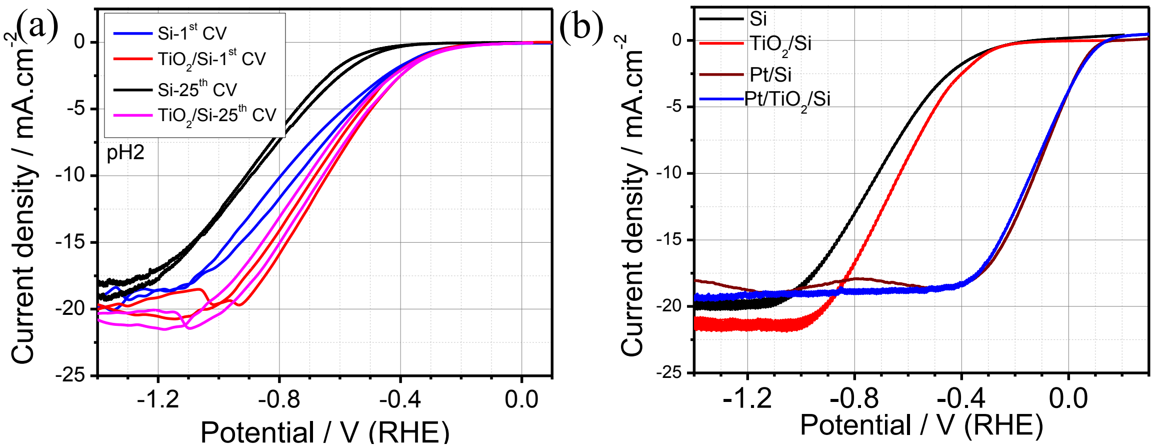

Figure 45: Cyclic voltammetry (CV) of Si and TiO_2/Si (a) and the Linear scan voltammetry (LSV) of Si, TiO_2/Si , Pt/Si and Pt/TiO_2/Si (b) under visible light irradiation in 0.1M H_2SO_4. In (a) the CV plot of the 1^{st} and 25^{th} cycles are shown for bare Si and TiO_2/Si.

In Figure 45(a) a comparison of 1^{st} and 25^{th} CV of Si and TiO_2/Si under illumination in 0.1M H_2SO_4 is shown. As can be seen the onset potentials for bare-Si and TiO_2/Si shift towards more cathodic direction with increasing number of CV cycles. The shifts in onset potential after 25 CV cycles for bare-Si and TiO_2/Si are from -340 to -574 mV vs. RHE and from -311 to -335 mV vs. RHE respectively. Moreover the saturation current remains unchanged for both electrodes. This indicates that with the cycle number the catalytic activity of the bare-Si photocathode change is more prominent compared to TiO_2/Si electrode.

Linear scan voltammetry (LSV) was used to measure the photocurrent density against applied potential. The LSV data for bare-Si and TiO_2/Si, Platinum nano-particle on Si (Pt/Si) and Pt nano-particle on TiO_2 coated Si (Pt/TiO_2/Si) photocathodes are shown in Figure 45(b). The onset potentials of the photocathodes at -1 mA/cm^2 are -340, and -311 mV vs. RHE for bare-Si and TiO_2/Si respectively. The onset potential of Pt/Si shifts towards more anodic direction and the shift is around 400 mV vs. RHE compared to Si. The saturation current of about -20 mA/cm^2 starting at -1.1 eV vs. RHE is observed for bare-Si. The saturation current starts at -1 V vs RHE and reaches about -21 mA/cm^2 for the TiO_2/Si photocathode. The saturation current in Pt/Si photocathode is -18 mA/cm^2 and starts at -400 mV vs. RHE. Among these photoelectrodes the TiO_2/Si has highest saturation current.

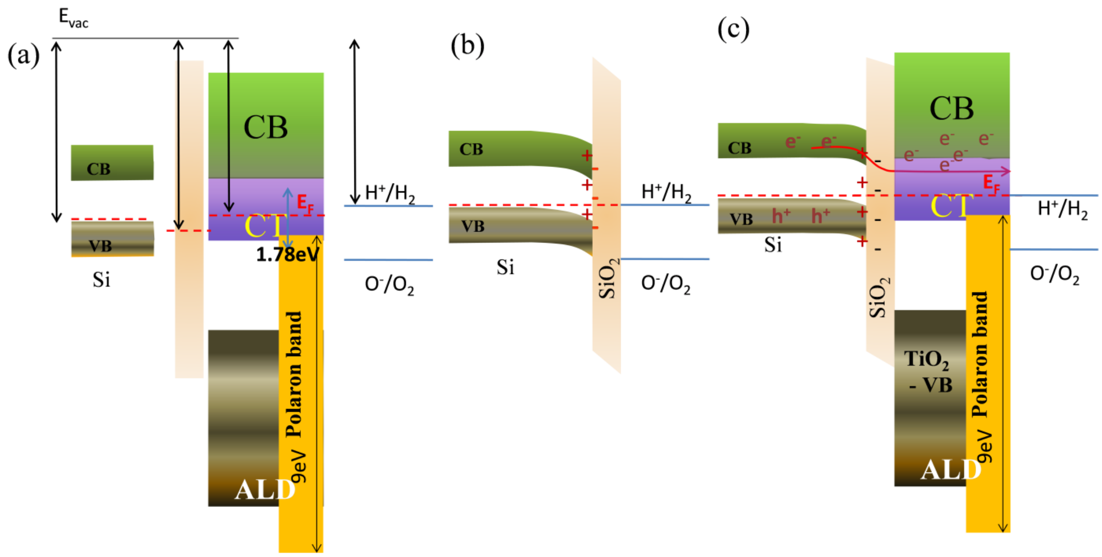

Figure 46: Schematic band diagram of Si, SiO_2 and TiO_2 separately (a), of Si/SiO_2 interface (b) and Si/SiO_2/TiO_2 interfaces in the equilibrium condition (c).

The increase in photocurrent density and the shift in onset potential for the TiO_2/Si can be understood by the band diagram of the p-Si/n-TiO_2 heterojunction. The schematic band diagrams of Si/SiO_2 interface and Si/SiO_2/TiO_2 interfaces are shown in Figure 46. In this diagram all the band edge position are shown with respect to the vacuum level. The p-Si photocathode is always covered with a native oxide and its thickness is about 1 nm, as obtained from the XPS Si 2p spectra (Figure 44c). The photogenerated charge carriers can tunnel through the insulating SiO_2 layer of thickness ~1 nm. In case of TiO_2/Si photo cathode the interfacial SiO_2 layer is also about 1nm thick and hence the charge carriers can tunnel thought this thin insulating layer too. The band alignments of p-Si (-5.05 eV), SiO_2 (-5.4 eV), TiO_2 (-4.9 eV) are done considering the electron affinity and aligning the respective Fermi levels with the redox potential ($E^0_{H2/H+}$= -4.7eV at pH=0) in Figure 46(a). Figure 46(b) shows the band alignment of Si/SiO_2 with the electrolyte. At the SiO_2/electrolyte interface there will be a band bending of 0.7eV towards the electrolyte. The band bending at the interface between p-Si and SiO_2 will be around 0.35 eV and this band bending will form electron accumulation layer at the p-S/SiO_2 interface. On illumination and under applied potential the photogenerated electrons will move through the SiO_2 layer to the electrolyte to perform the reduction reaction.

On the deposition of the TiO_2 layer at 250 ºC by ALD a very small (0.1 to 0.2nm) increase in the thickness of SiO_2 is observed. But the p-Si photo cathode becomes more stable under photoelectrochemical environment. The TiO_2 layer with an electronic band gap of 4.37eV does not decrease the photo catalytic performance of the photocathode and on the other hand the TiO_2 layer shifts the onset potential around 40 mV towards anodic direction. Figure 46(c) shows the schematic diagram of

$Si/SiO_2/TiO_2$/electrolyte interface under equilibrium condition. The Fermi level of the TiO_2 ALD layer lays 200 meV below the reduction potential of H_2O. In the literature the Fermi level of TiO_2 also found above the reduction potential of water (163). Nevertheless the processing conditions also change the band edge position and hence the relative Fermi level also changes (164). When the Fermi level of the TiO_2 is higher than the reduction potential the band bending will give rise to the depletion layer at the interface between TiO_2/electrolyte. The depletion layer will not allow electrons flow through it, therefore when TiO_2 is used as an absorber the photo generated holes move to the electrolyte to perform oxidation reaction to produce O_2 (165).

In the present study considering the Fermi level of TiO_2 and the reduction potential, the TiO_2 would have electron accumulation layer at the TiO_2-electrolyte interface. The band bending at TiO_2/SiO_2 and Si/SiO_2 interfaces will be 0.5 and 0.15 eV, respectively, and in both cases it will be accumulation type band bending. In the res-PES measurements of ALD TiO_2 layers the CT band is obtained due to the transfer of electrons from oxygen to titanium metal levels. The width of the CT band is about 1.78 eV and it starts around 0.6 eV below the Fermi level and extend into the CB. The CT bands are localized bands that start already in the band gap. Moreover, the localized polaronic band in TiO_2 starts far below in the VB and extends into the CT band. The localized band itself cannot move but the charge carriers can move through it since these bands consist of occupied states.

The photocathode here is consisting of Si as photo absorber and the thin film of TiO_2 is used as a protector against photo corrosion. The thin TiO_2 with wide optical band gap will not absorb the light and only Si will absorb the light of incident wavelength. The photo generated charge carriers have to move through the SiO_2 and TiO_2 layer to the electrolyte. The performance of the Si photo cathode depends on the surface layer on it. Since TiO_2 is a wide band gap material it may block the flow of charge carriers to the electrolyte but the LSV measurements show that the electrons can easily move through the TiO_2 layer. The primary aim to put TiO_2 on Si photocathode is to protect it against chemical degradation. Figure 46 (c) shows that the alignment of TiO_2 and H^+/H_2 energy levels and according to literature electron accumulation layer will be formed at the TiO_2/electrolyte interface (164). The accumulation layer will help in flow of electrons through the TiO_2 layer to the electrolyte but it also reduces the TiO_2 forming Ti^{3+} states (164). The formation of Ti^{3+} states in TiO_2 will degrade the protecting layer and hence the performance of photocathode will deteriorate over the time. In our measurements the TiO_2/Si photocathode was illuminated for 12 hours and the photocathode does not show any decrease in photo response and also from the XPS Ti2p core level spectra an increase of Ti^{3+} states is not found as shown in Figure 47 .

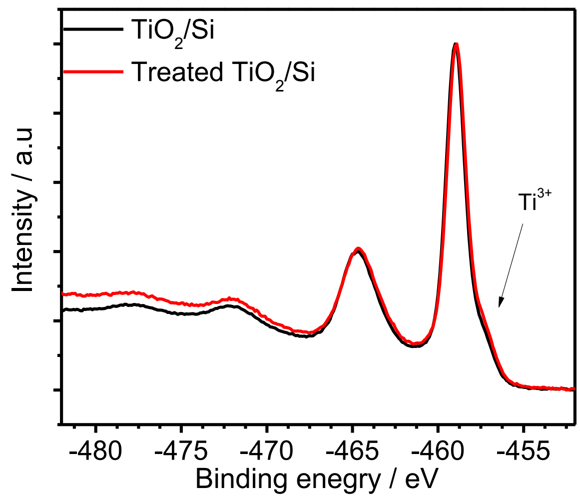

Figure 47: Ti2p XPS spectra before and after electrochemical measurements of TiO_2/Si photocathode. The XPS was measured with photon energy of 640 eV.

The alignment of the CT band of TiO_2 coincides with the VB and CB edges of the Si photoelectrodes; and the CT band is the band occupied with electrons and therefore any charge carrier can move through it. Moreover the CT band is not a single electronic state rather it works like a band with high density of electronic states. This means that the photo generated charge carriers in Si photoelectrodes have enough electronic states in TiO_2 through which the charge carriers can easily move to the electrolyte surface after tunneling through the SiO_2 layer. Hence, the presence of the CT band and its position in the TiO_2 makes TiO_2 a transparent metallic like material which provides stability against photo corrosion. Due to the metallic like behavior of TiO_2 there is no loss in overpotential of Si photoelectrode as presented in Figure 45. This fact also observed in literature [(163) (166)].

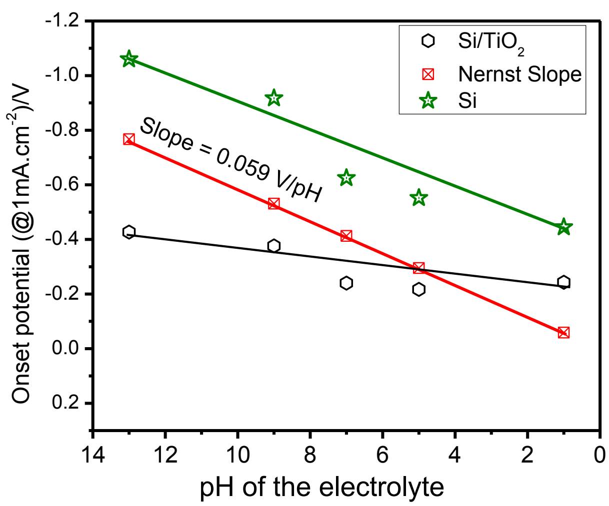

Figure 48: The Onset potential of Si and Si/SiO_2/TiO_2 photocathodes with varying pH value of the electrolyte. The onset at different pH values are compared to the Nernst slope. The potential values shown here are with respect to the Ag/AgCl reference electrode.

The TiO_2 layer also does not affect the loading of the catalyst on the photoelectrodes. In Figure 45 (b) the Pt/TiO_2/Si photoelectrode has the same onset potential as the Pt/Si photoelectrode. On the other hand, the TiO_2 over-layer on Si has a positive effect on the PEC performance of the photocathode in electrolyte media with different pH values. Figure 48 shows the onset potentials of bare-Si and TiO_2/SiO_2/Si at different pH values of the electrolyte. The onset potentials are taken here at a photocurrent density of the photocathodes 1mA/cm^2. The potential must shift by 0.059 V with the unit change in the pH of the electrolyte per decade according to Nernst equation. The red curve in Figure 48 shows the ideal Nernst plot. The redox potential of the electrolyte changes with the change in pH values and hence the VB and CB edge positions of the bare-Si also change (167). The strong change in the band edge position of bare-Si with the pH values of electrolyte restricts the generation of the maximal photovoltage from the Si photocathode. The generation of the photovoltage is responsible for the onset potential of the photocurrent of the photoelectrodes. In case of bare-Si the change in potential per pH is 0.059 V like in Nernst equation while in the case of the TiO_2/SiO_2/Si photocathode the change in potential per pH is 0.015 V. When the TiO_2 is coated on the Si surface the band bending at the interface is less than in the bare Si/electrolyte interface. In addition the band edge position of the TiO_2 covered Si does not change with the change in pH of the electrolyte resulting in higher photovoltage than in the bare-Si photocathode.

The weaker dependence of the onset potential of the TiO_2/SiO_2/Si photocathode with the change in pH could be related to the polaronic states in the TiO_2 over-layers. It is well known that charge carriers move in metal oxide by hopping mechanism thought the existing polarons. The spectroscopic measurements of the TiO_2 ALD layers in Figure 42 and Figure 43 show that the polaronic band starts in the VB and extends into the CT band. The polarons formation in TiO_2 is due to localized O2p^5 states in the VB. These localized states cannot move by themselves but the charge carriers can move easily via these states by hopping mechanism. In Figure 46(c) the band edge positions of Si and TiO_2 are shown along with the CT and polarons bands. There the existence of the polaronic band in TiO_2 can be seen and this band does not alter strongly with pH value changes due to the localized states starting from VB and extending into the CT band. The TiO_2 ALD layer has no band bending and shifts in band edge positions due to the availability of CT and polaronic states in the band gap.

The presence of CT and polaronic bands in TiO_2 makes it transparent for the flow of charge carriers through the TiO_2 layer without affecting the electrochemical performance of the photocathode and only weak shifting of the onset potential at different pH values of the electrolyte. Therefore, the thin film of TiO_2 ALD layers behave like metallic coating on Si photoelectrodes making them stable and better photoelectrodes for PEC devices. In literature TiO_2 have been used to protect both the photocathodes and photoanodes against photo corrosion [(163), (168), (166)]. This shows that our spectroscopic analysis is in agreement with our electrochemical data and can be applied to other photoelectrode systems too.

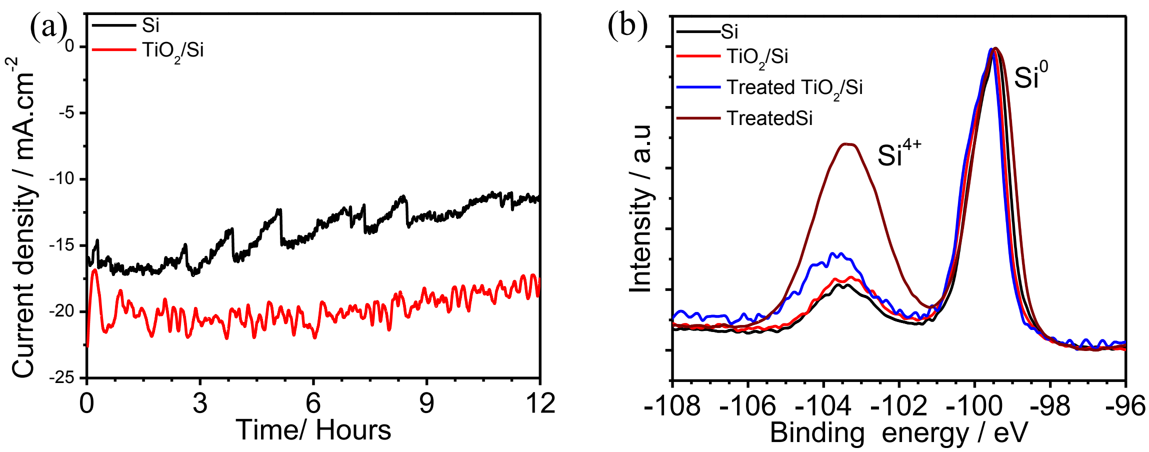

Figure 49: Chronoamperometry test of Si and TiO_2/Si photocathodes under illumination at -1V vs. RHE (a) and XPS (recorded with 1253eV excitation energy) of Si and TiO_2 before and after chronoamperometric measurements (b). The label 'treated' refers to the samples after chronoamperometry.

In Figure 49(a), the stability of the Si and TiO_2/Si photoelectrodes were examined by a chronoamperometry test at the constant applied potential of -1V vs. RHE, i.e. at the maximum power point. The Si electrode shows stable photocurrent density for 4 hours; afterwards the current density starts to decrease from -18 mA/cm^2 to -12mA/cm^2 after 12 hours. In the case of the TiO_2/Si photoelectrode the photocurrent stability extends to 8 hours and afterwards the photocurrent decreases only slightly over time from its initial value of -20 mA/cm^2 to -18.2 mA/cm^2. The stabilities of the Si and TiO_2/Si photocathodes were characterized by XPS as shown in Figure 49(b) where excitation energy of 1253 eV was used. The Si 2p lines confirm the presence of oxidized silicon at the interface. The bulk Si peak is observed at -99.4 eV binding energy whereas the second peak shifted 4 eV towards higher binding energy is attributed to silicon oxide. As expected the obtained Si 2p lines are more pronounced for the bare-Si photocathode. The ratios of both peaks change differently after the photoelectrochemical treatment (chronoamperometry for 12 hours) for the bare-Si and the TiO_2/Si electrodes. While the Si^{4+} to Si^0 peak intensity ratio is comparable for both electrodes before the treatment it changes strongly after the treatment, where the SiO_2 peak intensity becomes distinctly higher for the bare-Si electrode than for the TiO_2 coated Si electrode. Using equation 2.12, the thicknesses of the SiO_2 layers of the Si and TiO_2/Si electrodes are determined to be 0.9 and 1nm before the electrochemical treatments. The SiO_2 peak intensities increase after the electrochemical treatment and these intensities are corresponding to SiO_2 thicknesses of ~2 nm and ~1.3 for bare-Si and TiO_2/Si photocathodes, respectively. The decrease in photoresponse of bare-Si photocathode could be due to the stronger SiO_2 formation on Si during the long time electrochemical measurements. In contrast, the deterioration in photoreponse in case of the TiO_2/Si is limited due to the smaller SiO_2 formation underneath the TiO_2.

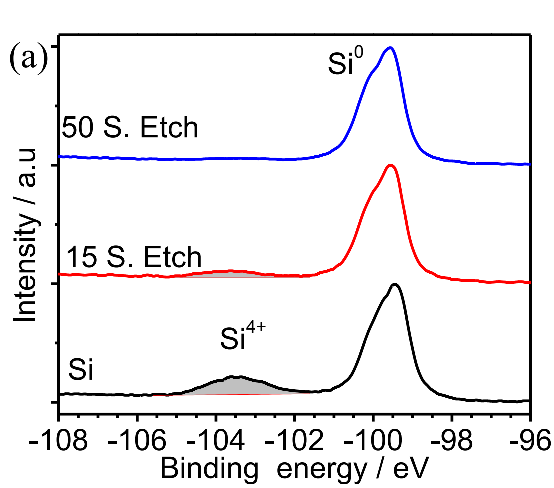

Figure 50: Si2p core level spectra of with different etching time to remove native SiO_2 (a) and Si2p spectra after deposition of TiO_2 on respective Si substrates (b).

Figure 49(a,b) shows that the formation of interfacial SiO_2 deteriorate the photoactivity of electrodes. The thicker SiO_2 layer on Si hinders the tunneling of photo generated electrons to the electrolyte surface and hence a stronger potential is needed to extract the same amount of charges through a thicker layer of SiO_2. Consequently, the increase in SiO_2 thickness causes a shift of the onset potential towards cathodic direction. The thicknesses of the SiO_2 interfacial layer must be controlled to realize better onset potentials in Si photocathodes. We vary the native SiO_2 thickness by etching the Si surface with 0.2% HF for 15 and 50 seconds, respectively. The Si2p spectra in Figure 50(a) show the corresponding Si^{4+} signals of the native SiO_2. The thickness of SiO_2 for Si with native SiO_2, after 15 seconds etching (15 S Etch) and after 50 seconds etching (50 S Etch) is 0.7, 0.4 and 0.2nm, respectively. Afterwards these electrodes were deposited by TiO_2 ALD layers. Here, the interfacial SiO_2 thickness increases with the ALD deposition. In Figure 50(b) we observe~~d~~ that the Si^{4+} signals in the Si 2p core level spectra increased after the TiO_2 deposition. The spectra after the TiO_2 deposition are noisy due to the attenuation of the signals by the TiO_2 layers. Using equation 2.12 the SiO_2 thickness underneath the TiO_2 layers are determined. The SiO_2 thicknesses for the bare Si and the etched samples before and after TiO_2 deposition are given in Table 19.

Table 19: Thickness of SiO_2 determined using Si2p core level spectra. The data of bare Si with native oxide and etched samples before and after TiO_2 deposition are shown.

Condition	Before ALD		After ALD	
	I_{SiO2}/I_{Si}	*Thickness (nm)*	I_{SiO2}/I_{Si}	*Thickness (nm)*
SiO_2 native	0.226	0.70	0.320	0.95
15S Etch	0.114	0.38	0.219	0.68
50S Etch	0.006	0.16	0.405	1.2

The chronoamperometry test and the XPS results in Figure 49 show that the photocatalytic activity of the Si photocathode deteriorates due to the increase of the SiO_2 interfacial layer. Therefore, if the SiO_2 interfacial layer can be controlled, the Si photocathode can perform better. It has been suggested by Dia et al. that an amorphous SiO_2 layer with a thickness of about 1nm can contribute to better activity of the Si photocathode (169). But the control of the SiO_2 thickness is not very straightforward, since Si is prone to oxidation in chemical and electrochemical environments. The SiO_2 interfacial thickness was controlled by etching the native SiO_2 partially and depositing TiO_2 by ALD afterwards. From the Si2p XPS spectra in Figure 50(a,b) the comparison before and after TiO_2 deposition shows a growth of SiO_2 on deposition of TiO_2. From the intensity of the Si^{4+} peak it is observed that the growth of SiO_2 is maximal when the native oxide is removed almost completely and after the TiO_2 deposition the SiO_2 thickness increases from 0.16 nm to 1.2±0.1 nm. In case of partially etched SiO_2 the growth rate is minimal and after the TiO_2 deposition the SiO_2 thickness increases from 0.38 nm to only 0.7±0.1 nm.

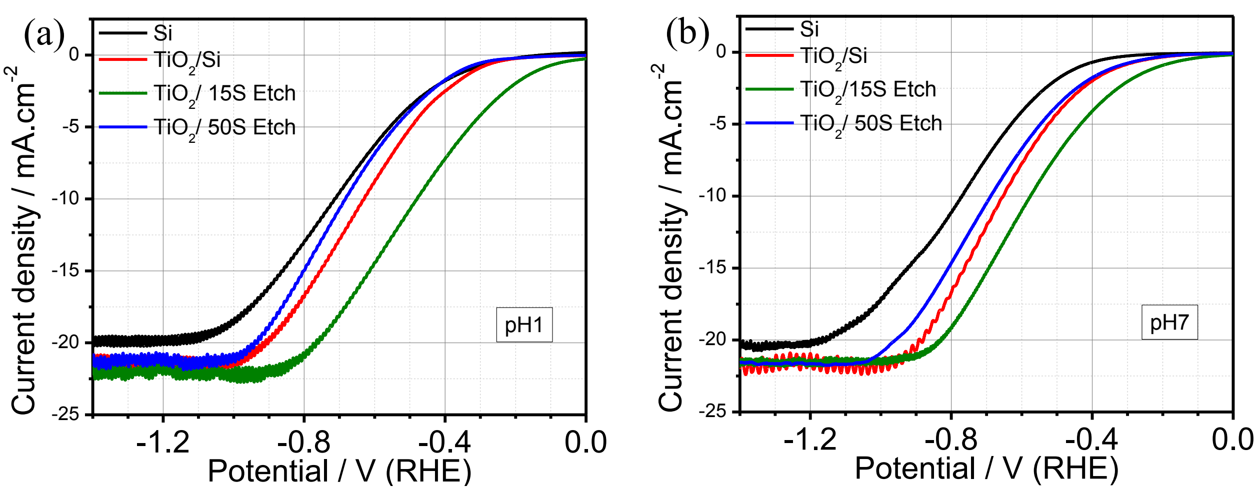

Figure 51: Linear scan voltammetry of bare SiO_2/Si and $TiO_2/SiO_2/Si$ photoelectrodes with SiO_2 interfacial layers of different thickness of. The LSV is taken under the illumination in two working electrolytes with pH = 1 (a) and pH = 7 (b).

The photoactivity of SiO_2/Si and TiO_2/SiO_2/Si photocathodes with different SiO_2 thicknesses are shown in Figure 51(a,b) in electrolytes with pH values of 1 and 7, respectively. In both electrolyte systems the SiO_2 thickness around 0.7±0.1nm (i.e. partially etched SiO_2, 15 seconds etching) shows better onset potential compare to the bare Si or TiO_2 coated native SiO_2/Si photo cathodes. In case of the sample where the native SiO_2 is completely etched the sample has about 1.2 nm SiO_2 after the TiO_2 ALD, and it shows more negative onset potential. This shift in onset potential could be due to the fast formation of SiO_2 during the ALD process. The same trend in the LSV curves of photo cathodes with different interfacial oxide thickness are observed in pH=1 and pH=7 electrolytes. In case of pH=1 the onset potential for the TiO_2 coated native SiO_2/Si and 15S Etch Si are -0.330 and -0.133 V (RHE), respectively, at $-1mAcm^{-2}$ current density. For pH=7 the onset potential for TiO_2 coated native SiO_2/Si and 15S Etch Si are-0.446 and -0.221 V(RHE), respectively, at $-1mA.cm^{-2}$ current density.

In the presented section the construction and operation of the photocathode for the hydrogen reduction based on a p-Si material is performed. Significant improvement in the performance is obtained by applying a protective TiO_2 layer and Pt nanoparticles as a catalyst. As it was shown that ALD can be used to control the thickness of SiO_2, with the control of interfacial SiO_2 thickness the onset potential of Si photocathode can be moved towards anodic potential. The photocatalytic activity of Si photocathode decreases when the SiO_2 thickness on Si is higher than 1 nm. The titanium dioxide layer fulfills its protective role, which is reflected in quite stable and improved performance of the photocathode. Here we combined our spectroscopic results with the photoelectrochemical results of TiO_2/Si photocathode and tried to understand the working principle of this heterojunction structured electrode. The alignment of the Si and TiO_2 band edges and the presence of the CT band allow an easy flow of photo generated charge carriers. However, due to the alignment of its energy bands with the potential of the HER, the possible photovoltage is too low to perform the efficient HER (170). Moreover due to the presence of the CT band the TiO_2 did not hinder the activity of the catalyst when added on the surface of TiO_2/Si electrodes.

3.4 Stable Si microstructured photoelectrodes

In this chapter effect of microstructuring of the Si surface on photocatlaytic water splitting and the stability issue will be addressed.

A p-type Si wafer with (100) orientation having a resistivity 10-20 Ωcm from CrysTec GmbH was taken as substrate for etching. The Si wafer was cut into pieces of 1X1 cm^2 and prior to electrochemical etching the Si pieces are sonicated for 5mins in each of these solutions: isopropanol, acetone and deionized water using an ultrasonic bath. The electrochemical etching solution is prepared by taking a mixture of HF(48%)-C_2H_5OH(99%)-H_2O in 1:1:2 by volumes [(171)]. A single compartment 2 electrode system was used for electrochemical etching. The electrochemical etching was carried out in galvanostatic mode applying current density starting from 2mA/cm^2 to 40mA/cm^2 for different etching time with a Keithley system. The preparations of microstructured Si are carried out in a fume hood to avoid contaminations from the electrochemical system during etching.

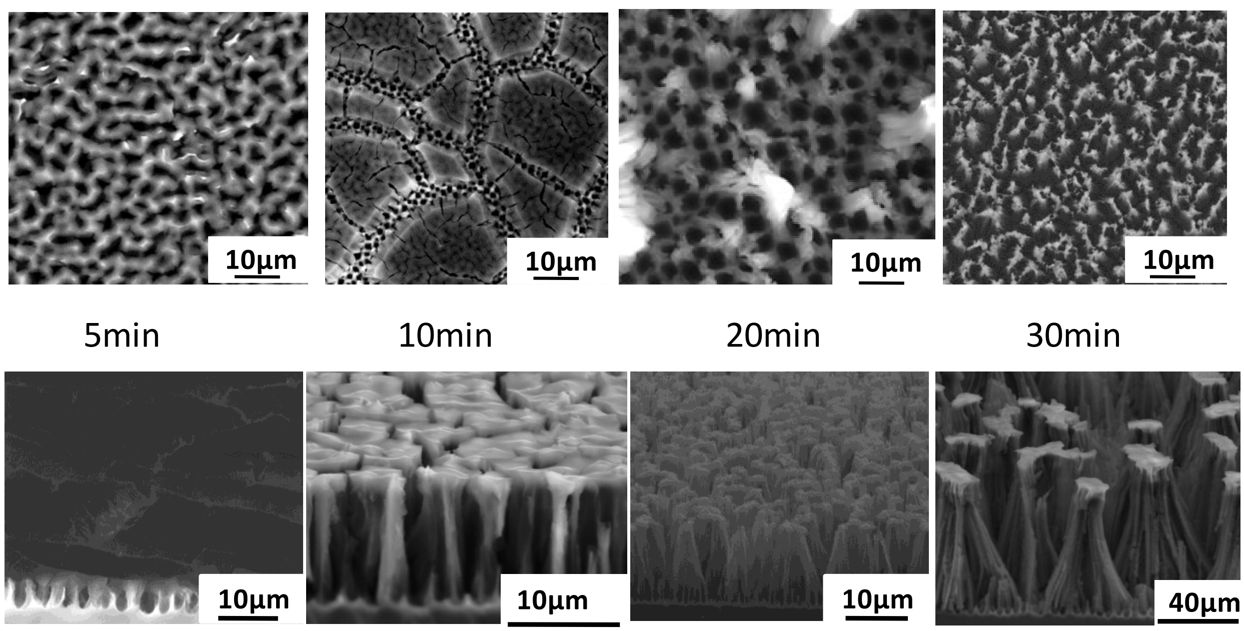

Figure 52: Scanning electron microscopy (SEM) images of etched Si after 5, 10, 20 and 30 minutes of etching with constant applied current densities of 40 mA/cm^2 in Galvanostatic mode. The upper panel shows top view of the Si microstructures and the in the lower panel the cross-sectional view of the respective Si microstructures are shows.

The scanning electron microscope (SEM) images of Si surface after etching with different time at constant applied current density is shown in Figure 52. The images shown here are corresponding to increasing etching times from 5 to 30 minutes presented here the left to the right. The thickness of the structured layers indeed increased with etching time under constant applied current density. After 5 minutes of etching the Si surface is covered with a thick initiation layer and underneath Si micro pillars (SiMPs) are formed. With the increase in etching time the initiation layer is also etched and the thickness of SiMPs increases due to the anisotropic etching. After etching for 10 minutes the initiation layer is still present on the surface, but after 20 minutes of etching the initiation layer is completely removed, as can be seen in the corresponding panel of Figure 52. When the etching time is increased to 60 minutes, the height of the microstructured Si pillars increases further and they cannot stand freely, but collapse. After 10, 20 and 30 minutes of etching the thicknesses of the layers are around 12, 22 and 40 µm respectively.

The elemental composition of the SiMPs was analyzed by XPS. As the electrochemical etching process consists of SiO_2 formation and subsequent etching with HF, we expect the presence of SiO_2 on the SiMPs, eventually removed by the HF etching. The XPS Si2p and O1s core level spectra, shown in Figure 53, indeed suggest that the as grown SiMPs samples are covered by Si-OH/SiO_2 that can be removed by HF.

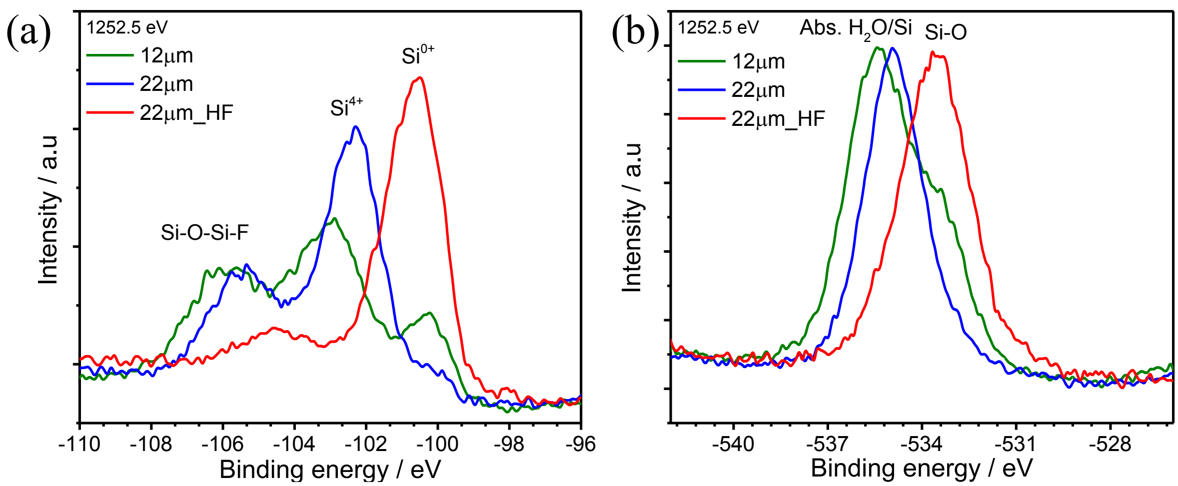

Figure 53: XPS measurements taken with Mg Kα source for Si2p (a) and O1s (b) of two as grown samples of thickness 12µm and 22µm and one HF etched sample of 22 µm. O1s spectra are normalized to the same maximum intensity to put in evidence the different peak energy, Si2p spectra are not modified.

The Si 2p core level spectra of the as grown samples (thickness 12 and 22 µm) in Figure 53(a) are composed of three main peaks at around 100, 103 and 105.5 eV. The peak around 105.5 eV corresponds to Si-O+Si-F bonding (172) and the peaks around 103 and 100 eV are attributed to SiO_x and Si respectively. The appearance of all three peaks in the spectra of the as grown SiMPs samples suggests that the as grown samples are covered with Si-OH/SiO_2. The O1s core level spectra of the as grown Si microstructured pillars (Figure 53(b)) consist of two main peaks at around 533.3 and 535 eV corresponding to Si-O and absorbed H_2O [(173) (174)]. Thus, both the Si2p and O1s XPS spectra of the as grown samples show that the SiMPs formed by electrochemical etching are covered by a thick layer of Si-OH /SiO_2.

The confirmation that the microstructure pillars are formed by Si is given by the changes in the Si2p spectrum of the 22µm thick pillars etched with HF, as it shows a higher peak at 100 eV corresponding to Si and the peaks at higher binding energies disappear (Figure 53(a)). The etching of Si-OH/SiO_2 is also confirmed by the O1s spectrum of the 22 µm thick micro pillars (Figure 53(b)) as it shifts to lower binding energy and the peak at 533 eV corresponds to the SiO_2. In addition the intensity of the SiO_2 peak after etching also decreased as shown in Figure 53(a).

The as grown 12 µm sample is covered with about 1µm thick initiation layer and this layer is mainly consisting of SiO_2 and Si-OH. Hence the peaks are shifted due to the charging effect. On the other hand in the thicker sample (22 µm) the initiation layer is partially removed and less SiO_2 is present, causing the absence of charging. This is reflected in the shift of the Si2p peak back towards the typical binding energy. Also the O1s spectrum of the 12 µm sample exhibits the Si-OH peak at higher binding energy than the 22 µm sample.

The photoelectrochemical activity of the microstructured Si electrodes was checked with VERSTAT4 potentiostat with a three electrode bottom cell electrochemical setup. As electrolyte 0.1M H_2SO_4 was used and Ag/AgCl and Pt were applied as reference and counter electrodes, respectively. The scan rates for CV and j-V measurements were 50 mV/sec. A visible light source with an intensity of 40 mW/cm^2 at the wavelength of 580 nm was used for photoelectrochemical measurements.

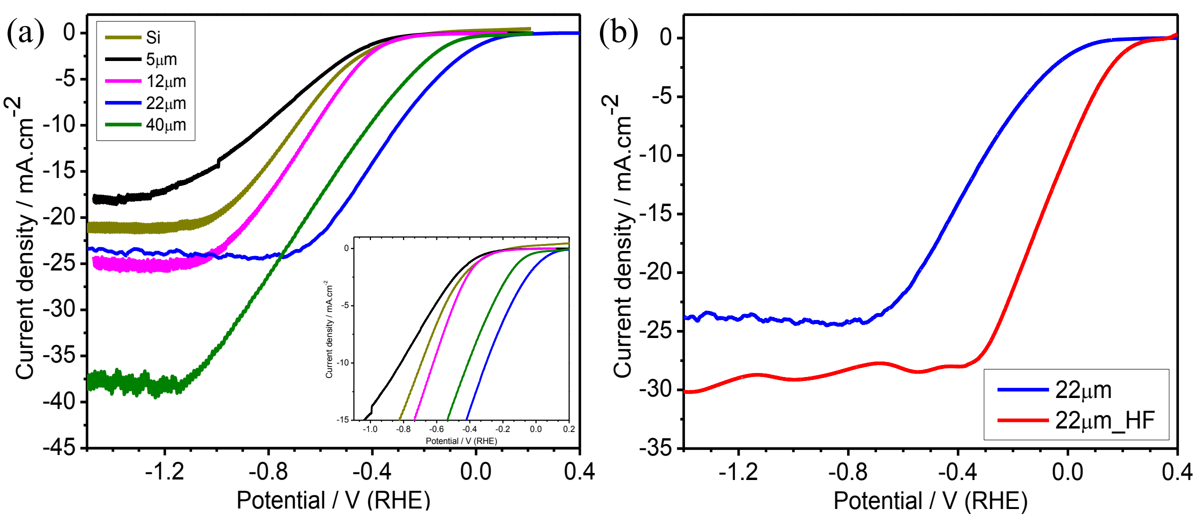

Figure 54: Photoelectrochemical activity (j-V curve) of (a) planar Si and microstructured Si photocathodes prepared with pillars of different thickness as given in the legend to check the H_2 production performance under visible light irradiation in 0.1M sulfuric acid and the inset plot shows the differences in onset potential of SiMPs. (b) Comparison of the PEC activity of the microstructured Si samples before and after HF etching.

The photocurrent density vs. voltage (j-V) graph in Figure 54 shows the performance of planar Si and SiMPs photocathodes of different thickness in 0.1M sulfuric acid electrolyte. In the j-V curve the photocurrent of Si starts to change at around -400 mV (RHE) and reaches saturation at around -1V (RHE). The SiMPs photocathodes show the same behavior but in most of the SiMPs photocathodes the photocurrent density is higher and the onset potential (shown inset of Figure 54) is lower than for the planar Si electrode, with the exception of the 7 µm thick sample where the photo current starts at more negative voltage and the saturation current is lower compared to the planar Si photocathode.

The increase of the photocurrent density and the shift in onset potential towards anodic direction shows the improvement in electrochemical performance of the SiMPs when a thickness larger than 7 µm is used. However, we observed that the diameter of the pillars is similar (~ 1 µm) in all the SiMPs samples whereas their height is different. Therefore, we tentatively suggest that the photoelectrochemical performance depends on the height of the pillars.

In our set-up, we found that the saturation current density of the planar Si is about 21 mA/cm^2 whereas for the 7, 12, 22 and 40 µm thick SiMPs it displayed values of 18, 25, 24 and 37.5 mA/cm^2, respectively (Figure 54). The difference in saturation photocurrent could be related to the surface reflectance. Indeed, the planar Si electrode is expected to have a higher surface reflectance of the incident light of about 25% (175), compared to the SiMPs. For example, the photoabsorption property of microstructures is discussed in the literature in terms of enhanced light trapping that enhances the photocurrent of nanostructured Si (176). Also SiMPs with diameters of around 1µm were used as efficient photoabsorbers by Warren et.al [(177)]. The orthogonal light absorption and the radial diffusion of photogenerated minority carriers in microstructured pillars have been demonstrated to efficiently increase the photocurrent density of microstructured Si (178). The increase in photocurrent density in case of SiMPs samples could be due to the higher light absorption efficiency and larger surface area for water reduction reaction. In case of the 7 µm sample the photocurrent density is lower due to the thicker initiation layer that hinders the transfer of photo generated minority carriers to the electrolyte.

To check the influence of the SiO_2 layer covering the SiMPs, we compared the behavior of the 22 µm thick film with and without HF etching. After the removal of the SiO_2, confirmed by the XPS analysis, the saturation current density increased from 24 to 30 mA/cm^2 and the onset moved further into anodic direction (Figure 54(b)). Dai et.al have shown that a Si nanowire with 1nm thin layer of SiO_2 exhibits higher photoelectrochemical performance than the planar Si or nanowire with thicker SiO_2 layer on it (169). A possible explanation for this result is that, due to the removal of the SiO_2 layer from the SiMPs photocathode, the photogenerated electrons can move to the electrolyte surface with a reduced recombination probability, producing a higher photocurrent as well as the shift of the onset potential in anodic direction.

Table 20: Open circuit potential, onset potential at 1mA/cm² current density and saturation current density of Si and SiMPs samples of different thickness and 22 μm sample etched with HF.

sample	OCP (V vs RHE)	On set pt. at -1mA.cm^{-2} (V/RHE)	Saturation current density mA/cm^2
Si	0.080	-0.341	21
7μm	0.034	-0.390	18
12μm	0.080	-0.328	25
22μm	0.170	0.090	24
22μm_HF	0.245	0.134	30

The open circuit potentials (OCP) of the Si and SiMPs are measured under light illumination and are given in Table 20. For higher OCP the shift in onset of the photocurrent is higher. The microstructuring of the electrode surface results in higher OCP of the SiMPs photocathodes than in the planar Si with the exception of the 7μm thick SiMPs. The increase of the OCP of SiMPs photocathodes reflects the onset shift towards more anodic direction in the j-V characteristics.

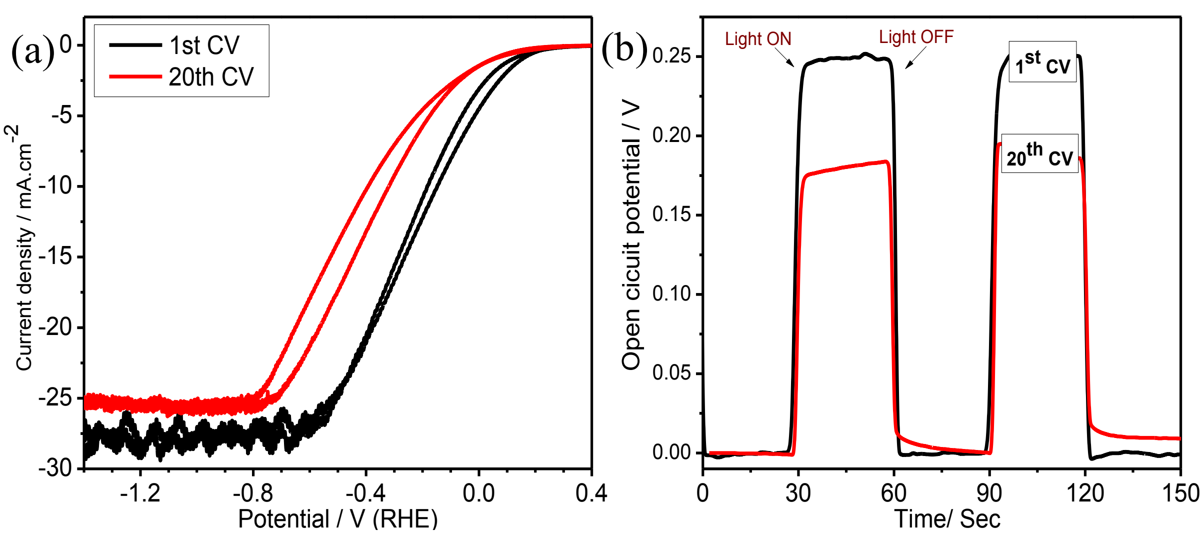

Figure 55: (a) 1st and 20th light irradiated cyclic voltammetry (CV) curves of 22 μm thick SiMPs samples etched with HF. (b) OCP after 1st and 20th CV cycle.

The stability of the SiMPs photocathodes is checked by continuous cyclic voltamogram under illumination and the results of the 22μm thick sample etched with HF are shown in Figure 55(a), the corresponding OCP is shown in Figure 55(b). The photoelectrochemical performance of the SiMPs deteriorates after 20 CV cycles where both the onset potential and the saturation photo current decrease. The decrease in photo response is also reflected in the OCP measurements shown in Figure 55(b). The OCP of the 22 µm SiMPs electrode decreases from 249 mV in the first CV cycle to 180 mV after 20 CV cycles. The decrease in photocurrent density and the shift in onset potential towards cathodic direction are related to the photo-generated charge separation at the electrode-electrolyte interface. The decrease in the PEC performance of the photocathode could be due to the formation of a thicker SiO_2 layer on the micropillars. For the stable performance of the photocathodes the SiMPs surface must be modified to avoid further oxidation.

The SiMPs surface can be protected by deposition of a conducting layer on it as already shown in the section 3.3. The best SiMPs sample is taken to deposit TiO_2 on it and test its electrochemical performance and stability for water splitting. The TiO_2 layer is deposited onto the 22 µm HF etched sample by applying 200 ALD cycles. The LSV measurements for TiO_2 deposited on 22 µm_HF SiMPs photo cathode is shown in Figure 56. After the deposition of TiO_2 onto the SiMPs sample the electrochemical performance show a very small change in onset potential but the photocurrent density remains the same. The OCP of the TiO_2 coated SiMPs is about 20 mV higher than that of the bare SiMPs samples (inset in Figure 56). This increase of the OCP results in a shift of the onset potential in more anodic direction by about 30 mV compared to its uncoated counterpart.

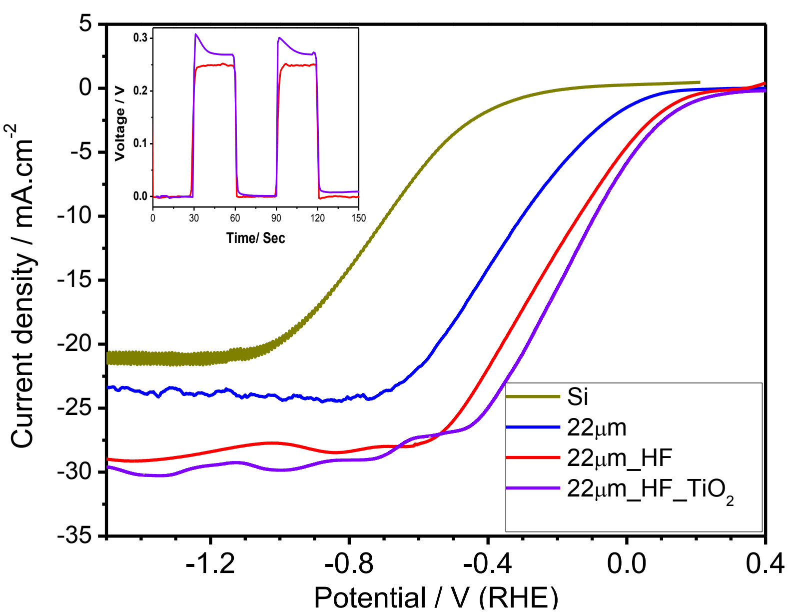

Figure 56: LSV measurement under illumination showing j-V curve of TiO_2 coated SiMPs in comparison to bare SiMPs and planar Si photocathodes. The OCPs of the TiO_2 coated and the bare 22 µm thick and HF etched (22µm_HF) SiMPs are shown in the inset.

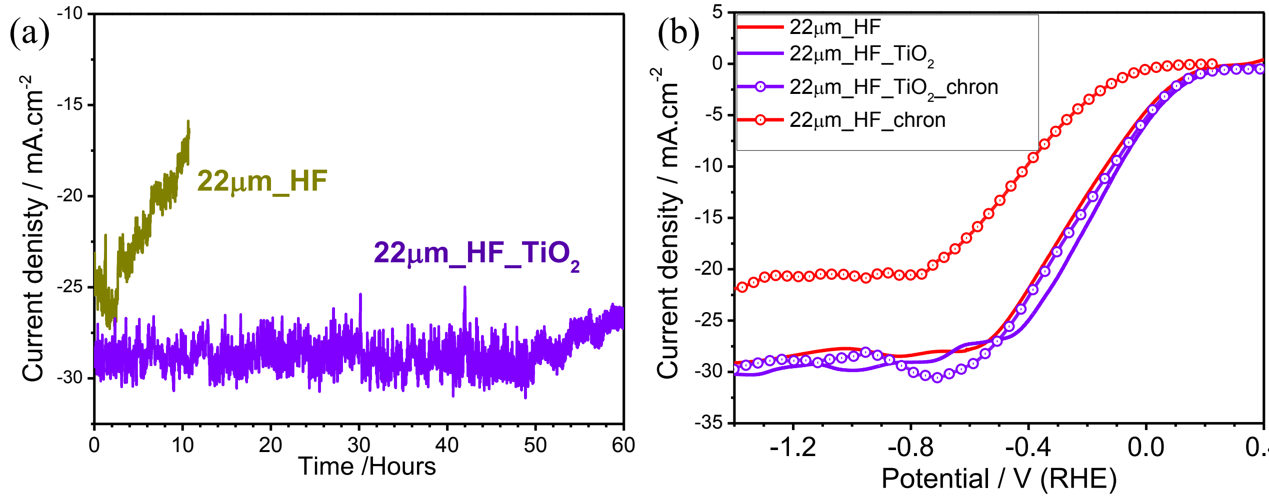

Figure 57: Chronoamperemetry test of TiO_2 coated and bare SiMPs sample at -0.8 V of applied (a) and the j-V curve before and after chronoamperometry test (b). In the latter the curves with circles joined with line shows the j-V curve after chronoamperometry test.

The photoelectrochemical stability of the TiO_2 coated and bare SiMPs samples are checked by the chronoamperometry test under illumination and the result is shown in Figure 57(a). In case of bare SiMPs the current density remains constant within the noise signal for 2 hours of illumination and then it starts to decrease gradually. After 10 hours of illumination, the current density of bare SiMPs decreased from 28 to 20 mA/cm^2. On the other hand the SiMPs sample coated with TiO_2 shows considerable stable current density of 30 mA/cm^2 for 3.5 hours and then a small fluctuation is observed. Unlike the bare SiMPs, the decrease in photocurrent density is slow in case of the TiO_2 coated SiMPs sample where the value changes from 30 mA/cm^2 to 27 mA/cm^2 after illumination in electrochemical medium for 50 hours. Furthermore, the LSV data of the coated and uncoated electrode before and after the chronoamperometric test (Figure 57(b)) underline the improved performance of the SiMPs photoelectrode where almost no change is observed for the TiO_2 coated electrode while a strong degradation is found for the unprotected sample. The thin and compact TiO_2 film deposited by ALD does not allow the SiMPs to be in direct contact with the electrolyte. Moreover the thickness of TiO_2 here is about 4 nm and hence the TiO_2 cannot effectively absorb light. So the coating of the SiMPs with TiO_2 does not compromise the optical properties of the SiMPs photocathode. The onset potential and the current density show that the TiO_2 did not negatively affected the electrical property of the SiMPs sample as shown in Figure 56 and Figure 57(b). The photogenerated minority charge carriers move through the thin TiO_2 film to the electrolyte to perform the chemical reaction. The protection of Si against photoelectrochemical corrosion have been studied by using insulating Al_2O_3, (179) conducting graphene layer (180), and semiconducting TiO_2 layers (2). In case of Al_2O_3 the limiting thickness for photo generated electrons to be transferred to the electrolyte is 3 nm since the Al_2O_3 is insulating and the charge carriers have to tunnel through this layer. On the other hand, when using TiO_2 prepared by ALD the thickness of TiO_2 can go up to more than 40 nm since this layer is amorphous and carries a high conductivity. In our study the TiO_2 grown by ALD is amorphous (181) so it has higher conductivity than the crystalline TiO_2. The ALD layers facilitate the easy flow of charge carriers through the Si/TiO_2 interface and protect the Si surface against direct contact to the electrolyte. Therefore, after electrochemical dissociation of the electrolyte the H_2 and O_2 will not be in direct touch with the Si surface and none of them can interact with the Si surface to decrease the photoelectrochemical properties of the photocathode.

The as prepared SiMPs have thick interfacial SiO_2 layer developed during the fabrication and the presence of this SiO_2 layer hinders the photo catalytic properties of the Si and SiMPs photocathodes. In the present study the SiMPs are etched with HF to realize the optimal SiO_2 thickness and afterwards they are coated with TiO_2 by ALD method. The ALD layer protects the Si against oxidation and hence increases the life time of the photocathodes. The TiO_2 coated SiMPs have two benefits for the photocathode application in water splitting device. It not only increases the photocurrent density but also shifts the onset potential towards anodic direction without any catalyst. Moreover TiO_2 coated SiMPs are stable for a long period of experiment such as 24 hours or more.

.

Chapter 4

SUMMARY

This thesis work embodies a detailed study of TiO_2 deposition by atomic layer deposition and subsequent characterization of the films by X-ray based spectroscopy. Referring to the characterization both the laboratory and synchrotron based X-ray are used to study the growth of TiO_2 with ALD and simultaneously ensuring the quality of the films. The electronic properties of the grown layers are characterized by X-ray absorption spectroscopy and compared to anatase and rutile reference samples single crystal. Additionally, it is already reported that ultra thin TiO_2 films are used to protect the Si photoelectrode against photo-corrosion. In our work, the effect and the stability of TiO_2 overlayer on p-type Si photoelectrode is studied as well. The thin TiO_2 layer is also beneficially against the corrosion of Si microstructured electrodes for photoelectrochemical devices prepared by electrochemical etching. It is also observed that the deposition of TiO_2 can be used to control the thickness of the interfacial SiO_2 layer which considerably influences the photoelectrochemical process.

Thin TiO_2 films were deposited using ALD technique with different precursors such as Titanium tetraisopropoxide and Titanium methoxide. The deposition process was carried out in the temperature range of 150 -315 °C to find the proper ALD window for both precursors. The growth rate per cycle obtained for TTIP and TiOMe are 1.5 and 0.6 Å per cycle, respectively, as determined by XPS analysis. The growth rate for TiOMe is lower than for TTIP due to its lower vapor pressure. From the XPS analysis the calculated stoichiometric (O: Ti) ratio of TiO_2 deposited either with TTIP or TiOMe is 1.97 respectively 1.7. In addition, the XPS results show that the Ti^{3+}:Ti^{4+} ratio in TiO_2 is 0.082 and 0.043 for the TiO_2 layers grown using TTIP and TiMeO precursors, respectively. The comparative study of the two precursors revealed that the growth rate is lower in case of TiOMe while the quality of the films is better (higher amount of Ti^{4+} states) than the films produced from TTIP. In contrast, the layers prepared with TTIP precursor show better and almost perfect O: Ti ratio of around 2. One of the most important finding of our work is that the TiO_2 ALD layer has higher amount of defect states in the band gap around 1eV below the Fermi level related to Ti3d states.

The effect of different substrates (Si, WO_3, RuO_x, Cu_xO_y, AlON) on the growth of TiO_2 was also investigated. We would like to report that a similar kind of film quality (O: Ti ratio and Ti^{3+}:Ti^{4+}) is found for all the substrates but the growth rate on RuO_x substrate is lower than on the others. The XAS measurements can be used as a fingerprint to identify the polymorphs of TiO_2 and it was found that the ALD films were amorphous in nature. When the TiO_2 film is grown at 315 °C the anatase polymorph can be obtained while it is not possible to achieve the rutile phase by ALD using TTIP.

The resonant photoelectron spectroscopy at O1s and Ti 2p edges is used to determine the corresponding unoccupied states in the TiO_2 ALD layers. Utilizing res-PES analysis we also determined the pDOS in the conduction band while the valance band measurements at resonance energies informs about the pDOS in the VB. The pDOS of VB and CB is used to determine the electronic band gap of TiO_2 which is found to be around 4.4 eV for the ALD sample while it is around 4.3 eV and 4.1 eV for the anatase and rutile reference samples. From the analysis of the res-PES data the oxygen vacancy derived polaronic states, the charge transfer band and their positions with respect Fermi level were deduced. The pDOS in the VB and CB is used to determine the charge neutrality level in TiO_2. From the res-PES measurements we discovered further an unusual Auger decay process where both the binding and kinetic energies change. We define that this kind of Auger decay process is related to the formation of three hole final states. We conclude that the use of res-PES measurement helps to evaluate various electronic properties of TiO_2 such as electronic band gap, pDOS, CNL, defect states and Auger processes. Moreover the electronic band gap of any colored material can be obtained with this technique since it does not involve the absorption of visible light like the UV-visible spectroscopic technique.

The effect of TiO_2 deposition onto Si based photocathodes on their catalytic activity is also investigated in this thesis work. The XPS study on Si photocathodes shows that even at cathodic potential the Si gets oxidized. The oxidation of Si can be reduced by the thin layer of TiO_2 on it. The native SiO_2 thickness increases from 0.9 nm to 2 nm for the bare Si photocathode during long time PEC operation while that one of the photocathode covered with TiO_2 increases only from 1 nm to 1.3 nm under the same conditions. Moreover the thin TiO_2 layer on the Si photocathode makes it stable for a period of 20 hours under illumination in electrochemical medium. The TiO_2 not only stabilizes the Si surface but it has also positive effect on the catalytic activity of the Si photocathode. For p-type Si TiO_2 is used as a protecting layer and it is proved that the TiO_2 layer facilitates the easy flow of charge carriers from the Si to the electrolyte through the TiO_2. The spectroscopic findings and the electrochemical results are correlated to investigate the flow of charge carriers through the TiO_2 protecting layer on the Si photoelectrode. The deposition of TiO_2 decreases the band bending at the Si/SiO_2 interface which in return results in higher open circuit potential and hence the overpotential of the TiO_2 coated Si photocathode decreases in comparison to the bare electrode. The CT and the polaronic bands of TiO_2 are also discussed and aligned to the Fermi level. The CT band is consisting of delocalized charges below the CB of TiO_2 and hence the charge carriers can easily move through this layer. When the CT band of TiO_2 is aligned with the Fermi level, the minimum of the CT band lays below the VB maxima and extend into the CB minima of p-Si. This shows that both types of charge carriers (electron/hole) can move via the CT to the electrolyte to perform the redox reaction. In addition, the TiO_2 layer helps the Si surface to suppress direct contact with the electrolyte medium to avoid oxidation as well as the reaction of evolved gases (O_2 or H_2) with the Si. The spectroscopic and electrochemical studies of TiO_2 ALD layers on Si photocathodes are addressed to understand the interfacial properties of the TiO_2 coating layer on photoelectrodes.

In the concluding part of this thesis the photocatalytic activity and the stability of Si micro pillars photocathodes prepared by electrochemical etching were investigated. The grown SiMPs are controlled and can be reproduced well by this technique. The XPS results on these SiMPs show that they are covered with a thick SiO_2 layer due to electrochemical oxidation during etching. The removal of SiO_2 overlayer results in shifts of the overpotential in photo-electrochemical measurements on SiMPs photocathodes. But the SiMPs are not stable for long time in the electrochemical medium. Therefore, the stability of the SiMPs is increased by the deposition of TiO_2 ALD layers on top of them.

In conclusion, the thesis is on the deposition of thin TiO_2 layers and their spectroscopic characterization using XPS, XAS and res-PES. The TiO_2 overlayers are useful to increase the stability of planar Si and SiMPs photocathodes in photoelectrochemical media. The main outcomes of this thesis are the appearance of defect and polaronic states and the determination of the electronic band gap in TiO_2 as well as the correlation between the spectroscopic data and the effect of TiO_2 deposition on the Si photoelectrode performance.

References

1. *Electrochemical photolysis of water at semicoudnctor electrode.* A. Fujishima and K. Honda. 1972, Nature, Vol. 238, p. 37.
2. *Amorphous TiO_2 coatings stabilize Si, GaAs, and GaP photoanodes for efficient water oxidation.* S. Hu, M. R. Shaner, J. A. Beardslee , M. Lichterman, B. S. Brunschwig and N. S. Lewis,. 2014, Science, Vol. 344, p. 1005.
3. *The surface sceince of titanium dioxide.* U.Diebold. 2003, Surface science reports, Vol. 48, p. 52.
4. *Switching phenomena in titanium oxide thin films.* F.Argall. 1968, Solid-state electron., Vol. 11, p. 535.
5. *Reinvestigation of the phase diagram for the system titanium–oxygen.* P.G. Wahlbeck, P.W. Gilles,. 1966, J. Am. Ceram. Soc., Vol. 49, p. 180.
6. M.M.Klinger, F.Rahemtullam, C.W.Prince, L.C. Lucas, and J.E. Lemons,. 1998, Oral. Bio.Med., Vol. 9, p. 449 .
7. *Thermodynamic analysis of phase stability of nanocrystaline titania.* H. Zhang and J.F.Banfield. 1998, J.Mater.Chem., Vol. 8, p. 2073.
8. *Structure and Energetics of water Adsorbed at TiO_2 antase (101) and (001) sruface.* A. Vittadini, A.Selloni, F.Rotzinger and M. Gratzel,. 1198, Phy. Rev. Lett., Vol. 81, p. 2954.
9. *Properties of amorphous and crystalline titanium dioxide from first principles.* B. Prasai, B. Cai, M. K.Underwood, J. P. Lewis and D. A. Drabold,. 2012, J. Mater. Sci., Vol. 47, p. 7515.
10. V.K. rao, S.V.N Naidu and L. Iyengar. 1970, J.Am. Ceram. Soc., Vol. 53, p. 124.
11. *Structureal-electronic relationships in inorganic solids: powder neutron diffraction studies of the rutile and anatase polymoprhs of titanium dioxide at 15 and 295 K.* . J.K. Burdett, T. Hughbanks, G.J. Miller, J.W. Richardson and J.V. Smith. 1987, J.Am. Chem. Soc., Vol. 109, p. 3639.
12. *Electrical and optical properties of rutile single crystals.* Cronemeyer, D.C. 1952, Phys. Rev., Vol. 87, p. 876.
13. *Electronicstructure of ideal TiO_2(110), TiO_2(001) and TiO_2(100) surfaces.* S.Munnix and M. Schmeits. 1984, Phys. Rev. B, Vol. 30, p. 2207.
14. *The surface science of metal oxides.* V.E. Henrich and P.A. Cox. 1994, 1st ed.. Cambridge University Press, Cambridge.
15. *Density Functional Theory Calculations of Dense TiO_2 Polymorphs: Implication for Visible-Light-Responsive Photocatalysts.* Mi.Y. Kuo, C.L. Chen,C.Y. Hua, H.C. Yang and P. Shen. 2005, J. Phys. Chem. B,, Vols. 109,, pp. 8693-8700.
16. *DFT+U calculations of crystal lattice, electronic structure, and phase stability underpressure of TiO2 polymorphs,.* M. E. A. de Dompablo, A. M. García, and M. Taravillo. 2011, J. Chem. Phys., Vols. 135, , pp. 054503,.
17. *Resonant photoemission of anatase TiO_2 (101) and (001) single crystals.* A. G. Thomas, W. R. Flavell, A. R. Kumarasinghe, A. K. Mallick, D. Tsoutsou and G. C. Smith. 2003, Phys. Rev. B, Vol. 67, p. 035110.
18. *Electronic and optical properties of three phases of titanium dioxide: rutile m anatase and brookite,.* S.D.Ching and W.Y. Mo. 1995, Phys.Rev.B, Vol. 51, p. 13023.
19. *Labeling interacting configurations throgh an anlysis of excitation dynamics in a resoannt photoemssion experiment: the case of rutile TiO2.* G. Drera, L. Sangaletti, F. Bondino, M. Malvestuto, L. Malavasi, Y. D. Fernandez, S. Dash, M. C. Mozzati and P. Galinetto. 2013, J. Phys.: Condens. Matter., Vol. 25, p. 075502.
20. *First-principles study of point defects in rutile TiO_{2-x}.* E. Cho, S. Han, H.-S. Ahn, K.-R. Lee, S. K. Kim, and C. S. Hwang. 2006, Phys.Rev.B, Vol. 73, p. 193202.
21. *The electronic structure and optical response of rutile, anatase and brookite TiO_2.* M Landmann, E Rauls and W G Schmidt,. 2012, J. Phys.: Condens. Matter, Vol. 24, p. 195503.

22. *Lattice dynamics and dielectric properties of incipient ferroelectric TiO_2 rutile.* C. Lee, P. Ghosez, and X. Gonze,. 1994, Phys.Rev.B, Vol. 50, p. 13379.
23. *Electronic and optical properties of anatase TiO_2.* R. Asahi, Y. Taga,W. Mannstadt and A.J. Freeman,. 2000, Phys.Rev. B, Vol. 61, p. 7459.
24. *Electronic properties of oxygen-deficient and aluminum-doped rutile TiO_2 from first principles.* M. M. Islam, T. Bredow, and A. Gerson,. 2007, Phys.Rev.B, Vol. 76, p. 045217.
25. *Electronic Structures of Manganese-Doped Rutile TiO_2 from First Principles.* G. Shao. 2008, J. Phys. Chem. C, Vol. 47, p. 18677.
26. *Electronic and optical properties of three phases of titanium dioxide: Rutile, anatase, and brookite.* Ching, Shang-Di Mo and W. Y. 1995, Phys.Rev.B, Vol. 15, p. 13023.
27. *Bulk and Surface Properties of Rutile TiO_2 from Self-Consistent-Charge Density Functional Tight Binding.* H. Fox, K. E. Newman, W. F. Schneider, and S. A. Corcelli,. 2010, J.Che.Theo. Comp., Vol. 6, p. 499.
28. *Ab initiostudy of the electronic states induced by oxygen vacancies in rutile and anatase TiO_2.* G. Mattioli, F. Filippone, P. Alippi and A. A. Bonapasta,. 2008, Phys. Rev. B, Vol. 78, p. 24120(R).
29. *Oxygen K near-edge fine structure: An electron-energy-loss investigation with comparisons to new theory for selected 3d Transition-metal oxides.* L. A. Grunes, R. D. Leapman, C. N. Wilker, R. Hoffmann, and A. B. Kunz,. 1982, Phys. Rev. B, Vol. 25, p. 7157.
30. *Ab-initio Electronic and Structural Properties of Rutile Titanium Dioxide.* C.E. Ekuma and D.Bagayoko. 2011, J. J. App.Phys., Vol. 50, p. 101103.
31. *A Theoretical Study on the Electronic Structures of TiO_2: Effect of Hartree-Fock exchange.* Y.F. Zhang, W. Lin, Y.i Li, .K.N. Ding, and J.Q. Li,. 2005, J.Phys.Chem.B, Vol. 109, p. 19270.
32. *Theoretical electronic properties of TiO_2 (rutile) (001) and (110) surfaces.* R. V. Kasowski and R. H.Tait. 1979, Phys. Rev. B, Vol. 20, p. 5168.
33. *Theoretical analysis of the structures of titanium dioxide crystals.* A.Fahmi, C. Minot, B. Silvi and M. Causa. 1993, Phys. Rev.B, Vol. 47, p. 11717.
34. *Pseudopotential periodic hartree-fock study of rutile TiO2.* B. Silvi, N. Fourati, R. Nada, and C. R. A. Catlow,. 1991, J. Phys. Chem. Solids, Vol. 52, p. 1005.
35. *Density functional theory analysis of the structural and electronic properties of TiO_2 rutile and anatase polytypes: Performances of different exchange-correlation functionals.* F. Labat, P. Baranek, C. Domain, C. Minot, and C. Adamo. 2007, J.Checm.Phys., Vol. 126, p. 154703.
36. *Structural and Electronic Properties of Selected Rutile and Anatase TiO2 surfaces :An ab initio investigation.* F.Labat, P.Baranek and C.Adamo,. 2008, J. Chem. Theory Comput, Vol. 4, p. 341.
37. *Insights into Current Limitations of Density Functional Theory.* A. J. Cohen, P. M. Sanchez and W. Yang,. 2008, Science, Vol. 321, p. 792.
38. *Challanges for density functional theory.* A.J. Cohen, P.M. Sanchez and W.Yang,. 2011, Chem. Rev., Vol. 112, p. 289.
39. *Band theory and Mott insulators: Hubbard U instead of Stoner I.* V. I. Anisimov, J. Zaanen, and O. K. Andersen,. 1991, Phys.Rev.B, Vol. 44, p. 943.
40. *Linear response approach to the calculation of the effective interaction parameters in the LDA+U method.* M. Cococcioni and S. de Gironcoli. 2005, Phys.Rev.B, Vol. 71, p. 035105.
41. *Density-functional thermochemistry. III. The role of exact exchange* . Becke, A. D. 1993, J. Chem. Phys, Vol. 98, p. 5648.
42. *Rationale for mixing exact exchange with density functional approximations.* J. P. Perdew, M. Ernzerhof and K. Burke. 1996, J. Chem. Phys, Vol. 1005, p. 9982.
43. *Anatase-rutile phase transformation of titanium dioxide bulk makterial: a DFT+U approach.* N. H. Vu, H. V. Le, T. M. Cao, V. V. Pham, H. M. Le and D. N. Manh,. 2012, J. Phys. : Condens. Matter, Vol. 24, p. 405501.

44. *Energy level alignment of a Zinc (II) tetraphenylporphyrin dye absorbed onto TiO_2 (111) and ZnO(1120) surface.* S. Rangan, S. Katalinic, R. Thorpe, R. A. Bartynski, J. Rochford and A. Galoppini. 2010, J. Phys. Chem. C, Vol. 114, p. 1139.
45. *Fine structure in the intrinsic absorption edge of $_{TiO2}$.* J. Pascual, J. Camassel and H. Mathieu,. 1978, Phys. Rev. B, Vol. 18, p. 5606.
46. *Self-energy and excitonic effects in the electronic and optical properties of TiO_2 crystalline phases.* L. Chiodo, J. M. G. Lastra, A. Iacomino, S. Ossicini, J. Zhao, H. Petek and A. Rubio,. 2010, Phys. Rev. B, Vol. 82, p. 045207.
47. *High resolution photoemission and x-ray absorption spectroscopy of a lepidocrocitelike TiO_2 nanosheet on Pt(110) (1 × 2).* L. E. Walle, S. Agnoli, I.-H. Svenum, A. Borg, L. Artiglia, P. Krüger, A. Sandell and G. Granozzi. 2011, J. Chem. Phys., Vol. 135, p. 054706.
48. *Predicting the band gap of ternary oxides containing 3d10 and 3d0 metals.* J. A. McLeod, A. Moewes, D. A. Zatsepin, E. Z. Kurmaev, A. Wypych, I. Bobowska, A. Opasinska and S. O. Cholakh. 2012, Phys. Rev. B, Vol. 86, p. 195207.
49. *Oxygen vacancies in transition metal and rare earth oxides: Current state of understanding and remaining challenges.* M. V. G. Pirovano, A. Hofmann and J. Sauer,. 2007, Surface Science Reports, Vol. 62, p. 219.
50. *First-principles study of native defects in anatase TiO_2.* S. Na-Phattalung, . . Smith, K. Kim, M. H. Du, S. H. Wei, S.B. Zhang, and S. Limpijumnong,. 2006, Phys. Rev. B, Vol. 73, p. 125205.
51. *Excess electron states in reduced bulk anatase TiO_2: Comparison of standrad GGA, GGA+U, and hybrid DFT calculations.* E. Finazzi, C. D. Valentin, G. Pacchioni and A. Selloni,. 2008, J. Checm. Phys., Vol. 129, p. 154113.
52. *Electronic structure of anatase TiO_2 oxide.* R. Sanjinés, H. Tang, H. Berger, F. Gozzo, G. Margaritondo and F. Lévy. 2006, Phys. Rev. B, Vol. 73, p. 125205.
53. *Surface electronic structure of TiO_2: Atomic geometry, ligand coordination, and the effect of adsorbed hydrogen.* Kurtz, V.E. Henrich and R.L. 1981, Phys. Rev. B, Vol. 23, p. 6280.
54. *Insights into photoexcited electron scavenging processes on TiO_2 obtained from studies of the reaction of O2 with OH groups adsorbed at electronic defects on TiO_2(110).* M.A. Henderson, W.S. Epling, C.H.F. Peden and C.L. Perkins. 2003, J. Phys. Chem. B, Vol. 107, p. 534.
55. *High mobility ntype charge carriers in large single crystals of anatase (TiO_2).* L. Forro, O. Chauvet, D. Emin, L. Zuppiroli, H. Berger and F. Lévy. 1994, J. App. Phys., Vol. 75, p. 633.
56. *Calculation of point defects in rutile TiO_2 by the Screened Exchange Hybrid Functional.* H. Y. Lee, S. J. Clark and J. Robertson,. 2012, Phys. Rev. B, Vol. 86, p. 075209.
57. *Synchrotron radiation studies of H_2O adsoprtion on TiO_2(110).* R. L. Kurtz, R. Stouckbar and T. E. Madey,. 1989, Surface Science, Vol. 218, p. 178.
58. *The Role of Interstitial Sites in the Ti3d Defect State in the Band Gap of Titania.* S. Wendt, P. t. Sprunger, E. Lira, G. K. H. Madsen, Z. Li m J. Ø. Hansen, J. Matthiesen, A. B. Rasmussen, E. Laegsgaard, B. Hammer and F. Besenbacher,. 2008, Sience, Vol. 320, p. 1755.
59. *Reoxidation of TiO_2,,110… via Ti interstitials and line defects.* K. T. Park, M. Pan, V. Meunier and E. W. Plummer,. 2007, Phys. Rev. B, Vol. 75, p. 245415.
60. *Theoretical Study of the Interstitial Oxygen Atom in Anatase and Rutile TiO_2: Electron Trapping and Elongation of the r(O-O) Bond.* H.i Kamisaka and K.Yamashita. 2010, J. Phys. Chem. C, Vol. 115, p. 8265.
61. *2p X-ray abosrption of Titanium in minerals.* F. M. F. de Groot, M. O. Figueiredo, M. J. Basto, M. Abbate, H. Petersen and J. C. Fuggle,. 1992, Phys. Checm. Miner., Vol. 19, p. 140.
62. *Ferroelectric distortion in $_{SrTiO3}$ thin films on Si,,001… by x-ray absorption fine structure spectroscopy: Experiment and first-principles calculations.* J. C. Woicik, E. L. Shirley, C. S. Hellberg, K. E. Anderson, S. Sambasivan, D. A. Fischer, B. D. Champan, E. A. Stern, O. Ryan, D. L. Ederer adn H. Li. 2007, Phys. Rev. B, Vol. 75, p. 140103.

63. *Bethe–Salpeter treatment of X-ray absorption including core-hole multiplet effects.* Shirley, E. L. 2005, J. Eelctron Spectrosc. Relat. Phenom., Vols. 144-147, p. 1187.
64. *X-ray absorption spectroscopy of titanium oxide by time dependent density functional calculation.* G. Fronzoni, R. De Francesco, M. Stener and M. Causa. 2006, J. Phys. Chem. B, Vol. 110, p. 9899.
65. *Multichannel multiple scattering calculation of L2,3-edge spectra of TiO_2 and $SrTiO_3$: importance of multiplet coupling and band structure.* P. Krüger. 2010, Phys. Rev. B, Vol. 71, p. 125121.
66. *Understanding the L2,3 x-ray absorption spectra of early 3d transition elements.* R. Laskowski and P. Blaha. 2010, Phys. Rev. B, Vol. 82, p. 205104.
67. *Suggested terms and definations in photocatalysis and radio catalysis.* N. Serpone and A, V. Emeline,. 2002, Intern. J. Photoeenrgy., Vol. 4, p. 91.
68. *Limiting and realizable efficiency of solar photolysis of water.* J. R. Bolton, S.J. Stickler and J.S. Connolly,. 1985, Nature, Vol. 316, p. 595.
69. *Solar water splting : progress using hematite (a-Fe_2O_3) photoelectrodes.* K. Sivula, F. Le Formal and M. Grätzel. 2011, Chem Sus Chem, Vol. 4, p. 432.
70. *Solar hydrogen production with nanostructured metal oxides.* R. van de Krol, Y. Liang and J. Schoonman,. 2008, J. Mater. Chem., Vol. 18, p. 2311.
71. Gerischer, H. Solar photoelectrolysis with semicoductor electrodes. [book auth.] B. O. Seraphin. *Solar Energy Conversion.* s.l. : Springer, 1979, Vol. 31, p. 115.
72. *Heterogeneous photocatalyst materials for water splitting.* A. Kudo and Y. Miseki. 2008, Chem. Soc. Rev., Vol. 38, p. 253.
73. *Photoelectrocatalysis: principles, nanoemitter applications and routes to bio-inspired systems.* H. J. Lewerenz, C. Heine, K. Skorupska, N. Szabo, T. Hannappel, T. Vo-Dinh, S. A. Campbell, H. W. Klemm and A. G. G. Muñoz. 2010, Energy Environ. Sci., Vol. 3, p. 748.
74. *Ideal hydrogen termination of the Si (111) surface.* G. S. Higashi, Y. J. Chabal, G. W. Trucks and K. Raghavachari. 1990, Appl. Phys. Lett., Vol. 56, p. 656.
75. *Spectroscopic Studies of the Modification of Crystalline Si(111) Surfaces with Covalently-Attached Alkyl Chains Using a Chlorination/Alkylation Method.* A. Bansal, X. L. Li, S. I. Yi, W. H. Weinberg and N. S. Lewis. 2001, J. Phys. Chem. B, Vol. 105, p. 10266.
76. *Photoelectrochemical behavior of n-Type Si(111) Electrodes Coated with single layer of graphene.* A. C. Nielander, M. J. Bierman, N. Petrone, N. C. Stadwitz, S. Ardo, F. Yang, J. Hone and N. S. Lewis. 2013, J. Am. Chem. Soc., Vol. 135, p. 17246.
77. *Behavior od n- and p-type single crystal semicoductors covered with n-TiO_2 films.* P.A. Kohl, S. N. Frank, and A.J. Bard. 1977, J. electrochem. Soc., Vol. 124, p. 225.
78. *Atomic layer-deposited tunnel oxide stabilizes silicon photoanodes for water oxidation.* Y. W. Chen, J. D. Prange,S. Dühnen, Y. Park, M. Gunji, C. E. D. Chidsey and P. C. McIntyre. 2011, Nat. mat., Vol. 10, p. 539.
79. *Photoelectrohcemistry: application to solar energy convesion.* Nozik, A. J. 1978, Ann. Rev. Phys. Chem., Vol. 29, p. 189.
80. *Improvment of photoelectrochemical hydriogen generation by surface modification of p-type Silicon semicoductor photocathodes.* R. N. Dominey, N. S. Lewis, J. A. Bruce, D. C. Bookbinder and M. S. Wrighton. 1982, J. Am. Chem. Soc., Vol. 104, p. 467.
81. *Hydrogen production using a molybdenum sulfide catalyst on a titanium-protected n^+p-Silicon photocathode.* B. Seger, A. B. Laursen, P. C. K. Vesborg, T. Pedersen, O. Hansen, S. Dahl, and I. Chorkendorff. 2012, Angew. Chem. Int. Ed., Vol. 51, p. 9128.
82. *Evaluation of Pt, Ni, and Ni–Mo electrocatalysts for hydrogen evolution on crystalline Si electrodes.* R. McKone, E. L. Warren, M. J. Bierman, S. W. Boettcher, B. S. Brunschwig, N. S. Lewis and H. B. Gray. 2011, Energy Envior. Sci., Vol. 4, p. 3573.
83. *Wireless solar water splitting using Silicon-based semicodcutors and eath-abundant catlysts.* S. Y. Reece, J. A. Hamel, K. Sung, T. D. Jarvi, A. J. Esswein, J. J. H. Pijpers and D. G. Nocera. 2011, Science, Vol. 334, p. 645.

84. *Chemistry of High-Temperature Materials.* A. M. Shevjakov, G. N. Kuznetsova, and V. B. Aleskovskii,. Leningard : s.n., 1967. Proceedings of the Second USSR Conference on High-Temperature Chemistry of Oxides. p. 149.
85. T. Suntola and J.Antson. *4,058,430* U.S., November 15, 1977.
86. *Über eine neue Art von Strahlen.* Röntgen, W. C. 1898, Annalen der Physik,, Vol. 1, p. 300.
87. *Radiation from electrons in a synchrotron.* F. R. Elder, A. M. Gurewitsch, R. V. Langmuir, and H. C. Pollock,. 1947, Phys. Rev., Vol. 71, p. 829.
88. SOLEIL. [Online] http://www.docsciences.fr/IMG/swf/soleil.swf.
89. X-ray Laser XFEL. [Online] http://mpsd.cfel.de/images/content/e208/e209/index_eng.html.
90. *The versatility of collimated plane grating monochromators.* Follath, R. 2001, Nucl. Instrum. Methods Phys. Res., Vol. 467, p. 418.
91. *Spektroskopie der Röntgenstrahlen .* Siegbahn, M. Berlin, : Springer, 1931.
92. *Calculations of electron inelastic mean free paths V Data for 14 organic compounds over the 50-2000 eV range.* S. Tanuma, C.J. Powell, D.R. Penn,. 1994, Surf. Interface Anal., Vol. 21, p. 165.
93. *Atomic subshell photoionization cross sections and asymmetry parameters: 1 Z 103.* J. Yeh, I. Lindau,. 1985, Atomic Data and Nuclear Data Tables, Vol. 32, p. 1.
94. Stöhr, J. *NEXAFS Spectroscop.* New York : Springer-Verlag, 1992. Vol. 25.
95. *Resonant X-ray spectroscopy to study K absorption pre-edges in 3d transition metal compounds,.* P. Glatzel, M. Sikora and M. Fernandez-Garcia,. 2009, Eur. Phys. J. Special Topics , Vol. 169, p. 207.
96. *Atomic radiative and radiationless yields for K and L shells.* Krause, M.O. 1979, J. Phys. Chem., Vol. 8, p. 307.
97. *New type of auger efect and its influence on the X-ray spectrum.* D. Coster and R. Kronig. 1935, Physica,, Vol. 2, p. 13.
98. *Rhe L2:L3 intensity ratio in soft X-ray emission spectra of 3d-metals.* E. Kurmaev, A. Ankudinov, J. Rehr, L. Finkelstein, P. Karimov and A. Moewes,. 2005, J. Elc. Spec. Rel. Phenom., Vol. 148, p. 1.
99. *Atomic radiative and radationless yields for K and L shells.* M.O. Krause. 1979, J. Phys. Chem., Vol. 8, p. 307.
100. *Ultrafast charge transfer and nuclear dynamics studied with resonant X-ray spectrscopy.* Foehlisch, A. 2006, Appl. Phys. A,, Vol. 85, p. 351.
101. Richter, M. H. *Excitation and polarons in resonant auger decay process.* Cottbus : BTU Cottbus-Senftenberg, 2014. PhD Thesis.
102. *Electronic properties of ideal and interface-modified metal-semiconductor interfaces.* Monch, W. 1996, J. Vac. Sci. Technol. B, Vol. 14, p. 2985.
103. *Band offsets of wide-band-gap oxides and implications for futre electronics.* J. Robertson. 2000, J. Vac. Sci. Technol. B, Vol. 18, p. 1785.
104. *Band offsets, Schottky barrier heights, and their effects on electronic devices.* J. Robertson. 2013, J. Vac. Sci. Technol. A, Vol. 31, p. 050821.
105. *Titanium isopropxide as a perecursor in atomic layer epitaxy of titanium dioxide thin flm.* M. Ritala, M.Leskelä, L. Niinistö and P.Haussalo,. 1993, Chem. Mater., Vol. 5, p. 1174.
106. *Atomic layer deposition of photocatalytic TiO_2 thin films from titanium tetramethoxide and water.* V. Pore, A. Rahtu, M. Leskelä, M. Ritala, T. Sanjavaara and J. Keinonen,. 2004, Checm. Vap. Deposition, Vol. 10, p. 143.
107. *TiO_2 thin films by chemical vapor deposition: control of the deposition process and film characterisation.* Derking, Z. Chen and A. 1993, J. Mater. Chem., Vol. 3, p. 1137.
108. *Reaction Mecahnism studies on titanium isopropoxide-water atomic layer depostion process.* A. Rahtu and M.Ritala. 2002, Chem. Vap. Depo., Vol. 8, p. 21.
109. *Final state condtirbution to the Si 2p binding energy shift in SiO_2/Si(100).* T. Eickhoff, V. Medicherla and W. Drude. 2004, J. Ele. Spec. Rel. Phen., Vol. 137, p. 85.
110. *Electronic states at the interface of Ti-Si oxide on Si(100).* C.C. Fulton, G. Lucovsky and R.J. Nemanich,. 2002, Vol. 20, p. 1726.

111. *Understanding the interface reaction of tutile TiO_2 grown by atomic layer deposition on oxidized ruthenium.* M. Popovici, A. Delabei, C. Adelmann, J. Meersschaut, A. Franquet, M. Tallarida, J. van Den Berg, O. Richard, J. Swerts, K. Tomida, M. S. Kim, H. Tielens, H. Bender, T. Conard, M. Jurczak, S. Van Elshocht and D. Schmeisser. 2013, J. Sold. Stat. Sc. Tech., Vol. 2, p. N23.
112. *TiO_2 thin films prepared by pulsed beam chemical vapor deposition from titanium tetraisopropoxide and water.* H. Döring, K. Hasimoto and A. Fujishima,. 1992, Ber. Bunsenges. Phys. Chem., Vol. 96, p. 620.
113. *Titanium isopropoxide as a precursor for atomic layer deposition: characterization of titnium dioxide growth process.* J. Aarik, A. Aidla, T. Uustare, M. Ritala and M. Leskela,. 2000, Appl. Surf. Sc., Vol. 161, p. 385.
114. *Selective atomic layer deposition of titanium oxide on patterned self-assembled monolayers formed by microcontact printing.* M. H. Park, Y. J. Jang, H. M . Sung-Suh and M. M. Sung,. 2004, Langmuir, Vol. 20, p. 2257.
115. *Fityk: ageneral-purpose peak fitting program.* Wojdyr, M. J. Appl. Cryst., Vol. 43, p. 1126.
116. *Oxygen vacancy origin of the sruface band-gap state of TiO_2(100).* C. M. Yim, C.L. Pang and G. Thornton. 2010, Phys. Rev. Lett., Vol. 104, p. 036806.
117. *Growth of TiO2 wit thermal and plasma enhanced atomic layer deposition.* M. Tallarida, D. Friedrich, M. Städter, M. Michling, and D. Schmeißer. 2011, J. Nanoscience and Nanotechnology, Vol. 11, p. 1.
118. *Interface effects in the lectronic structure of TiO_2 deposited on MgO, Al_2O_3 and SiO_2 substrates.* L. Soriano, M. S. Agudo, R.J.O. Mossanek, M. Abbate, G. G. Fuentes, P.R. Bressler, L. Alvarez, J. Mendez, A. Gutierrez and J. M. Sanz,. 2011, Surf. Sc., Vol. 605, p. 539.
119. *In situ ALD experiments with synchrotron radiation photoelectron spectroscopy.* M. Tallarida and D. Schmeisser. 2012, Semicond. Sci. Technol., Vol. 27, p. 074010.
120. *Polaronic satellites in X-ray asboprtion spectra.* Laan, G. van der. 1990, Phys. Rev. B, Vol. 41, p. 12366.
121. *Ti2p and O1s X-ray absorption of TiO2 polymorphs.* R. Ruus, A. Kikas, A. Saar, A. Ausmees, E. Ndmmiste, J. Aarik, A. Aidla, T. Uustared and L. Martinson'. 1997, Sol. Stat. Comm., Vol. 104, p. 199.
122. *Ferroelectric distortion in $SrTiO_3$ thin films on Si(001) by x-ray absorption fine structure spectroscopy: Experiment and first-principles calculations.* J. C. Woicik, E. L. Shirley, C. S. Hellberg, K. E. Andersen, S. Sambasivan, D. A. Fischer, B. D. Chapman, E. A. Stern, P. Ryan, D. L. Ederer and H. Li,. 2007, Phys. Rev. B, Vol. 75, p. 140103.
123. *Electronic structure of titania aerogels from soft x-ray absorption spectroscopy.* S. O. Kucheyev, T. van Buuren, T. F. Baumann, J. H. Satcher, Jr., T. M. Willey, R. W. Meulenberg,. 2004, Phys. Rev. B, Vol. 69, p. 245102.
124. *Electronic polaron excitations inthe X-ray absorption spectrum of TiO_2.* G. Van Der Laan, C. S. Mythen and H. A. Padmore,. 1990, Europhys. Lett., Vol. 11, p. 67.
125. *Plorization dependence of resonant X-ray emission spectra in 3dn transition metal coompounds with $n = 0, 1, 2, 3$.* M. matsubara, T. Uozumi, A. Kotani, Y. Harada, and S. Shin,. 2002, J. Phys. Soc. Jap., Vol. 71, p. 347.
126. *Properties of disorder-engineered black titanium dioixde nanoparticles through hydrogenetaiton.* X. Chen, L. Liu, Z. Liu, M. A. Marcus, W.C Wanf, N. A. Oyler, M. E. Grass, B. Mao, P. A. Glans, P. Y. Yu, J. Guo and S. S. Mao. 2013, Scientific report, Vol. 3, p. 1.
127. *Electronic structure of cluster assembled nanostructured TiO_2 by resonant photoemission at the Ti $L_{2,3}$ edge.* T. Caruso, C. Lenardi, R. G. Agostino, M. Amati, G. Bongiorno, T. Mazza, A. Policicchio, V. Formoso, E. Maccallini, E. Colavita, G. Chiarello, P. Finetti, F. Šutara, T. Skála, P. Piseri, K. C. Prince and P. Milani,. 2008, J. Chem. phys., Vol. 128, p. 094704.

128. *The effect of valence state and site geometry on Ti $L_{3,2}$ and O K electron energy-loss spectra of TixOy phases.* E. Stoyanov, F. Langenhorst and G. S. Neumann,. 2007, American Mineralogist, Vol. 92, p. 577.
129. *A Ti L-edge X-ray absorption study of Ti-silicate glasses.* G. S. Henderson, X. Liu and M. E. Fleet,. 2002, Phys. Chems. of Minerals, Vol. 29, p. 32.
130. *L2,3 x-ray-absorption edges of d0 compounds: K^+, Ca^{2+}, Sc^{3+}, and Ti^{4+} in Oh (octahedral) symmetry.* F. M. F. de Groot, J. C. Fuggle, B. T. Thole and G. A. Sawatzky,. 1990, Phys. Rev. B, Vol. 41, p. 928.
131. *L2,3 absorption spectra of the lighter 3d transition metals.* J. Zaanen, G. A. Sawatzky, J. Fink, W. Speier and J. C. Fuggle. 1985, Phys. Rev. B, Vol. 32, p. 4905.
132. *Electron-Hole Excitations in Semiconductors and Insulators.* M. Rohlfing and S. G.Louie. 1998, Phys. Rev. Lett., Vol. 81, p. 2312.
133. *X-ray absorption spectra at the Ca $L_{2,3}$ edge calculated within multichannel multiple scattering theory.* P. Krüger and C. R.Natoli. 2004, Phys. Rev. B, Vol. 70, p. 245120.
134. *Electron energy loss and X-ray absorption spectroscopy of rutile and anatase: a test of structural sensitivity.* R. Brydson, H. Sauer, W. Engel, J. M. Thomass, E. Zeitler, N. Kosugi and H. Kuroda,. 1989, J. Phys: Cond. Matt., Vol. 1, p. 797.
135. *Strong polaronic effects on rutile TiO2 electronic band edges.* C. Persson and A. F. da Silva. 2005, Appl. Phys. Lett., Vol. 86, p. 231912.
136. *Ti 2p X-ray absorption in titanium dioxides (TiO_2): the influence of the cation site environment.* J. P. Crocombette and F. Jollet. 1994, J. Phys: Cond. Matt., Vol. 6, p. 10811.
137. *New fine structure resolved at the ELNES Ti-$L_{2,3}$ edge spectra of anatase and rutile: comparision between experiment and claculation.* M. Ceynet, S. Pokrant, S. Irsen and P. Krüger,. 2010, Ultramicroscopz, Vol. 110, p. 1046.
138. *The CTM4XAS program for EELS and XAS spectral shape analysis of transition metal L edges.* Groot, E. Stavitski and F. M. F. de. 2010, Micron, Vol. 41, p. 687.
139. *Bulk and surface polarons in photoexcited anatase TiO2.* C. D. Valentin and A.Selloni. 2011, J. Phys. Chem. Lett., Vol. 2, p. 2223.
140. *Hybridization and bond-orbital components in site-specific X-ray spectra of rutile TiO_2.* J. C. Woicik, E. J. Nelson, Leeor Kronik, M. Jain, J. R. Chelikowsky, D. Heskett, L. E. Berman, and G. S. Herman. 2002, Phys. Rev. Lett., Vol. 89, p. 077401.
141. *Electronic structure of anatase TiO_2 oxide.* R. Sanjinés, H. Tang, H. Berger, F. Gozzo, G. Margaritondo and F. Lévy. 1994, J. Appl. Phys., Vol. 75, p. 2945.
142. *Dterminationof coudction and valence band electronic structure of anatase and rutile TiO_2.* J. Szlachetko, K. M.- Mauke, M. Nachtegaal and J. Sa,. 2014, J. Chem. Sci., Vol. 126, p. 511.
143. *Oxygen 1s x-ray-absorption edges of transition-metal oxides.* F. M. F. De Groot, M. Grioni, J. C. Fuggle, J. Ghijsen, G. A. Sawatzky and H. Petersen,. 1989, Phys. Rev. B, Vol. 40, p. 5715.
144. *Thermal and plasma enhanced atomic layer deposition of TiO_2: Comparison of spectroscopic and electric properties.* C. Das, K. Henkel, M. Tallarida, D. Schmeißer, H. Gargouri, I. Kärkkänen, J. Schneidewind, B. Gruska, M. Arens. 2015, J. Vac. Sci. Tech. A, Vol. 33, p. 01A144.
145. *Role of point defects on the reactivity of reconstructed anatase titanium dioxide (001) surface.* Y. Wang, H. Sun, S. Tan, H. Feng, Z. Cheng, J. Zhao, A. Zhao, B. Wang, Yi. Luo, J. Yang and J.G. Hou,. 2013, Nat. Comm., Vol. 4, p. 1.
146. *Oxygen K near-edge fine structure: An electron-energy-loss investigation with comparisons to new theory for selected 3d Transition-metal oxides.* L. A. Grunes, R. D. Leapman, C. N. Wilker, R. Hoffmann and A. B. Kunz. 1982, Phys. Rev. B, Vol. 25, p. 7157.
147. *X-ray absorption spectra of niobium dichalcogenides and their first-row transition-metal.* Sarode, P. R. 1987, J. Phys. F, Vol. 17, p. 1605.
148. *Size effect on the conduction band orbital character of anatase TiO_2 nanocrystals.* L. Vayssieres, C. Persson and J.-H. Guo. 2011, Appl. Phys. Lett., Vol. 99, p. 183101.

149. *Quantum size efefcts in TiO_2 thin films grown by atomic layer deposition.* M. Tallarida, C. Das and D. Schmeisser,. 2014, Beilstein J. Nanotechnol., Vol. 5, p. 77.
150. *Electronic structure of cobalt–nickel mixed oxides.* S. Schmidt and D.Schmeisser. 2012, Sol. stat. Ionic, Vol. 225, p. 737.
151. *Multiple auger decay at resonant photon-excitation in carbon thin films.* M. Richter, I. Paloumpa, D. Friedrich and D. Schmeisser,. 2013, ECS Trans., Vol. 20, p. 9.
152. *Resonant photomeission at the O1s thresold to characterize In2O3 single crystals.* J. Haeberle, M. Richter, Z. Galazka, C. Janowitz and Schmeisser. 2014, Thin Solid Films., Vol. 555, p. 53.
153. *Valence and Conduction band states of PCBM as probed by photoelectron spectroscopy at resonant excitation.* M. Richter, D. Friedrich and D. Schmeisser. 2012, Bionno Science., Vol. 2, p. 59.
154. *Multiple Auger process in graphene.* M. Richter, U. Starke and D. Schmeisser,. 2014, J. Elet. Spec. Relt. Phen., Vol. 192, p. 1.
155. *Oxygen vacancies in transition metal and rare earth oxides: Current state of understanding and remaining challanges.* M. V. G-Pirovano, A. Hofmann and J. Sauer,. 2007, Surf. Sc. Rept., Vol. 62, p. 219.
156. *Electronics structure of amrophous ZnO films.* D. Schmeisser, J. Haeberle, P. Barquinha, D. Gaspar, L. Pereira, R. Martins and E. Fortunato,. 2014, Phys. Status Solid C, Vol. 11, p. 1476.
157. *Effects of configuration interaction on intensities and phase shifts.* Fano, U. 1961, Phys. Rev., Vol. 124, p. 1866.
158. *Fano resonance in nanoscale structures.* A. E. Miroshnichenko, A. Flach and Y. S. Kivshar. 2010, Rev. Mod. Phys., Vol. 82, p. 2257.
159. *Resonant photoemssion at the O1s thresld to characterize β-Ga_2O_3 single crystal.* M. Michling and D. Schmeisser. 2012, IOP Conf. Series: Materials Science and Engineering, Vol. 34, p. 012002.
160. *Band alignment of rutile and anatase TiO_2.* D. O. Scanlon, C. W. Dunnill, J. Buckeridge,S. A. Shevlin, A. J. Logsdail,S. M. Woodley, C. R. A. Catlow, M. J. Powell, R. G. Palgrave, I. P. Parkin, G. W. Watson,T. W. Keal, P. Sherwood, A. Walsh and A.A. Sokol,. 2013, Nat. Mat, Vol. 12, p. 798.
161. *Photoelectrochemical conversion in a WO_3 coated p-Si photoelectrode: effect of annealing temperature.* K.H. Yoon, C.W. Shin and D.H. Kang. 1997, J. Appl. Phys., Vol. 81, p. 7024.
162. *Silicon photoelectrodes modified with ultrafine metal islands.* Y. Nakato and H. Tsubomura. 1992, Electrochemical Acta, Vol. 37, p. 897.
163. *Using TiO_2 as a conductive protective layer for photocathodic H2 evolution.* B. Seger, T. Pedersen, A.B. Laursen, P.C.K. Vesborg, O. Hansen and I. Chorkendorff. 2013, J. Am. Chem. Soc., Vol. 135, p. 1057.
164. *Ultrathin films on copper(I) oxide water splitting photocathodes: a study on performance and stability.* A. Paracchino, N. Mathews, T. Hisatomi, M. Stefik, S. D. Tilley and M. Grätzel,. 2012, Enrgy Environ. Sci., Vol. 5, p. 8673.
165. *Photocatalytic waters plitting using semicondcutor particles: History and recent developments.* K. Maeda. 2011, J Photochem. photobio. C: Photochem Rev., Vol. 12, p. 237.
166. *Amorphous TiO_2 coatings stabilize Si, GaAs, and GaP photoanodes for efficient water oxidation.* S. Hu, M. R. Shaner, J. A. Beardslee, M. Lichterman, B.S. Brunschwig and N. S. Lewis. 2014, Science, Vol. 344, p. 1005.
167. *Photoelectrochemical cells.* Grätzel, M. 2011, Nature (London), Vol. 414, p. 338.
168. *Highly active oxide photocathode for photoelectrochemical water reduction.* A. Paracchino, V. Laporte, K. Sivula, M. Grätzel and E. Thimsen,. 2011, Nat. Mat., Vol. 10, p. 456.
169. *Solar hydrogen generation by silicon nanowires modified with platinum nanoparticle catalysts by atomic layer deposition.* P. Dai, J. Xie, M. T. Mayer, X. Yang, J. Zhan, and D. Wang,. 2013, Angew. Chem. Int. Ed. , Vol. 11119, p. 52.
170. *Silicon photoelectrodes modified with ultrafine metal islands.* Y. Nakato and H.Tsubomura. 1992, Electrochemica Acta, Vol. 37, p. 897.

171. *Wide-band "black silicon" based on porous silicon.* L.L. Ma, Y.C. Zhou, N. Jiang, X. Lu, J. Shao, W. Lu, J. Ge, X.M. Ding and X.Y. Hou,. 2006, Appl. Phys. Lett., Vol. 88, p. 171907.
172. *In situ x-ray photoelectron spectrsocpy analysis of SiOxFy passivation layer obtained in a SF_6/O_2 cryoetching process.* J. Pereira, L. E. Pichon, R. Dussart, C. Cardinaud, C. Y. Duluard, E. H. Oubensaid, P. Lefaucheux, M. Boufnichel and P. Ranson,. 2009, Appl. Phys. Lett., Vol. 94, p. 071501.
173. *SiO_2/Si (100) interface studied by Al Kα x-ray and synchrotron radiation photoelectron spectroscopy.* Z. H. Lu, M. J. Graham, D.T. Jiang and K.H. Tan. 1993, Appl. Phys. Lett., Vol. 63, p. 2941.
174. *Growth and Structure of Water on SiO_2 Films on Si Investigated by Kelvin Probe Microscopy and in Situ X-ray Spectroscopies.* A. Verdaguer, C. Weis, G. Oncins, G. Ketteler, H. Bluhm and M. Salmeron,. 2007, Langmuir, Vol. 23, p. 9699.
175. *Nanoporous black silicon photocathode for H_2 production by photoelectrochemical water splitting.* J. Oh, T. G. Deutsch, H. C. Yuan and H. M. Branz,. 2011, Energy Environ. Sci., Vol. 4, p. 1690.
176. *Light trapping in Silicon nanowire solar cells.* E. Garnett and P. Yang. 2010, Nano letters, Vol. 10, p. 1082.
177. *Photoelectrochemical water splitting: silicon photocathodes for hydrogen evolution.* E. L. Warren, S. W. Boettcher, J. R. McKone and N. S. Lewis,. 2010, Proc. of SPIE., Vol. 7770, pp. 77701F-7.
178. *Comparison of the device physics principles of planar and radial p-n junction nanorod solar cells.* B. M. Kayes, H. A. Atwater and N. S. Lewis,. 2005, J. Appl. Phys. Lett., Vol. 97, p. 114302.
179. *Long-term durable silicon photocathode protected by a thin Al_2O_3/SiO_x layer for photoelectrochemical hydrogen evolution.* M. J. Choi, J. Y. Jungt, M. J. Park, J. W. Song, J. H. Lee and J. H. Bang,. 2014, J. Mater. Chem., Vol. 2, p. 2928.
180. *N-doped monolayer graphene catalyst on silicon photocathode for hydrogen production.* U. Sim, T. Y. Yang, J. Moon, J. An, A. Hwang, J. H. Seo, J. Lee, K. Y. Kim, J. Lee, S. Han, B. H. Hong and K. T. Nam,. 2013, enrgy Environ. Sc., Vol. 6, p. 3658.
181. *Linear dichroism in ALD layers of TiO_2.* C. Das, M. Tallarida and D. Schmeisser,. 2013, Environ. Earth Sc., Vol. 70, p. 3785.
182. P.Willmott. *An introduction to synchrotron radaition techniques and application.* Swiss Ligth Source - Paul Scherrer Institute : Wiley, 2011.
183. SOLEIL. [Online] http://www.docsciences.fr/IMG/swf/soleil.swf.
184. *Inherent post-collision interaction in spectator: AUger-transition in metal and charge-trasfer systems.* Ohno, M. 2001, J. Elect. Spec. Relt. Pheno., Vol. 120, p. 33.
185. *Heterojunction solar cell prepared by chemical vapour deposition of doped SnO_2 on textured silicon.* S.R. Vishwakarma, Rahmatullah and H.C. Prasad. 1993, Sol. Stat. Commun., Vol. 85, p. 1055.
186. *Polaronic satellites in X-ray absroption spectra.* Laan, G. van de. 1990, Phys. Rev. B, Vol. 41, p. 12366.
187. *Self-energy and excitonic effects in the electronic and optical properties of TiO_2 crystalline phases.* L. Chiodo, J. M. G.-Lastra, A. Iacomino, S. Ossicini, J. Zhao, H. Petek and A. Rubio,. 2010, Phys. Rev. B, Vol. 82, p. 045207.
188. *The surface sceince of titanium dioxide.* U.Diebol. 2003, Surface science reports, Vol. 48, p. 52.
189. Antson, T. Suntola and J. *4,058,430* U.S., November 15, 1977.

Abbreviation of phrases

AAC	Atomic absorption coefficient
ALD	Atomic layer deposition
CB	Conduction band
CBM	Conduction band maxima
CIS	Constant initial state
CT	Charge Transfer
CV	Cyclic voltammetry
CVD	Chemical vapor deposition
CNL	Charge neutrality level
DOS	Density of states
HER	Hydrogen evolution reaction
GPC	Growth per cycle
KE	Kinetic energy
pDOS	Partial density of states
PEC	Photoelectrochemical
PEY	Partial electron yield
RHE	Reverse hydrogen electrode
TiOMe	Titanium methoixde
TTIP	Titanium isopropoxide
Res-PES	Resonance photoelectron spectroscopy
SEM	Scanning electron microscopy
TEY	Total electron yield
VB	Valence band
VBM	Valence band maxima
XAS	X-ray absorption spectroscopy
XLD	X-ray linear dischroism
XPS	X-ray photoelectron spectroscopy

List of Publications

Own Publications:

1. **C.Das**, M. Richter, M. Tallarida and D. Schmeisser, Electronic properties of ALD films, anatase and rutile TiO_2 studied by resonant photoemission spectroscopy. (under review)

2. **C.Das**, M. Tallarida and D. Schmeisser, Si microstructures laminated with a nanolayer of TiO_2 as long-term stable and effective photocathodes in PEC devices. Nanoscale 2015, 17, 7726.

3. **C.Das**, K. Henkel, M. Tallarida, H. Gargouri, I. Kärkkänen, J. Schneidewind, B. Gruska, M. Arens and D. Schemeisser, Thermal and Plasma enhanced ALD of TiO_2: comparison of spectroscopic and electric properties. *J. Vac. Sci. Technol. A* 2015, 33, 01A144

4. M. Tallarida, **C. Das**, D. Cebrev, K. Kukli, A. Tamm, M. Ritala, T. Lana-Villareal, R. Gómez, M. Leskela and D. Schemisser, Modification of Hematite Electronic Properties with Trimethyl Aluminum to Enhance the Efficiency of Photoelectrodes. *J. Phys. Chem. Lett. 2014, 5, 3582.*

5. M. Tallarida, **C. Das** and D. Schmeisser, Quantum size effects in TiO_2 thin films grown by atomic layer deposition. *Beilstein Journal of Nanotechnology, 2014, 5, 77.*

6. **C. Das**, M. Tallarida and D. Schmeisser, Linear Dichroism in ALD layers of TiO_2. *Env. Earth Sci. 2013, 8, 3785*.

Publication in collaboration work:

1. A. Indra, P. W. Menezes, **C. Das**, C. Göbel M. Tallarida, D. Schmeisser and M. Driess, Unveiling the Role of $Co^{2+}/^{3+}$ in Octahedral and Tetrahedral Sites for Water Oxidation: Structure Activity Relationship in Cobalt Oxide Catalysts. (under preparation)

2. D. Cibrev, **C. Das**, M. Tallarida, D. Schmeisser and R. Gómez, A study of the electrochemicaly pretreated hematite photoanode with improved properties for water splitting.(under preparation)

3. D. Cibrev, **C. Das**, M. Tallarida, D. Schmeisser and R. Gómez, The electron enrichment as an efficient strategy to improve the water splitting performance on TriMethylAluminum epitaxially coated hematite photoanodes.

4. A. Indra, P. W. Menezes, **C. Das**, M. Tallarida, D. Schmeisser and M. Driess, Multi-Shelled Cobalt Manganese Oxide Hollow Spheres as the Bifunctional Catalyst for the Photoelectrochemical Water Splitting. (submitted)

5. A.Indra, P. Menezes, N.Ranjbar Sahraie, A. Bergmann, **C. Das**, M. Tallarida, D. Schmeisser, P. Strasser and M. Driess, Unification of Catalytic Water Oxidation and Oxygen Reduction Reactions: Amorphous Beat Crystalline Cobalt Iron Oxides. *J. Am. Chem. Soc. 2014, 136, 17530.*

6. D. Barreca, G. Carraro, A. Gasparotto, C. Maccato, F. Rossi, G. Salviati, M. Tallarida, **C. Das**, F. Fresno, D. Korte, U. L. Stangar, M. Franko and D. Schmeißer, Surface Functionalization of Nanostructured Fe_2O_3 Polymorphs: From Design to Light-Activated Applications. *ACS Appl. Mat. & Int. 2013, 5, 7130*.

Conference contribution

Oral Presentations

1. Si microstructures coated with TiO_2 film and nano islands by ALD for photocathodes in PEC device
   C. Das, M. Tallarida, D. Schmeißer
   EMRS, Sept. 15-18, 2014, Warsaw, Poland
2. X-ray linear dichroism in atomic layer deposited Titanium dioxide layers.
   C. Das, M. Tallarida, D. Schmeißer, DPG Spring meeting 2014, Dresden
3. Control of thickness of SiO_2 interfacial layer for photocatalytic water splitting on Si photocathodes.
   C. Das, M. Tallarida, D. Schmeißer , DPG Spring meeting 2014, Dresden
4. Surface modified Si photocathode used for a wide range of electrolyte pH values
   C. Das, M. Tallarida, D. Schmeißer , Symposium A "Energy conversion applications of atomic layer deposition" EMRS- May 27-31, 2013 Strasburg, France
5. TiO_2 thin layer on p-Si for efficient and pH independent photo catalytic water splitting.
   C. Das, U. I. Kramm, M. Tallarida, D. Schmeißer , Hybird photovolitcs 2013 symposium,May 15-17, 2013 Berlin, Germany
6. An efficient Si photo cathode for a wide range of electrolyte pH values.
   C. Das, M. Tallarida, K. Skorupska, H.-J. Lewerenz, D. Schmeißer , DPG Spring meeting, March 10-15, 2013 Rgensburg , Germany.
7. XMLD and electrochemical properties of TiO_2 layers grown by ALD methods on p-Si (100).
   C. Das, M. Städter, M. Tallarida, D. Schmeiße , 2012 International Students and Young Scientists Workshop "Photonics and Microsystems" July 06-08, 2012, Szklarska Poręba, Poland
8. TiO_2 ALD on p-type Si to enhance and stabilize Si as photoelectrochemical absorber.
   C. Das, M. Tallarida, D. Schmeißer, K. Skorupska, H.-J. Lewerenz, AVS12th International Conference on Atomic Layer Deposition (AVS) June 17-20, 2012, Dresden.
9. Investigation of Linear Dichroism in ALD layers of TiO_2.
   C. Das, M. Städter, M. Tallarida,D. Schmeißer, DPG-Spring meeting , March 25-30, 2012 Berlin

Poster presentation

1. Electrochemically prepared microstructured Si photocathodes for water splitting. C. Das, M. Tallarida, D. Schmeißer , IPS-20, July 27- Aug 01, 2014 Berlin , Germany.
2. Electrochemically prepared microstructured Si photocathodes for water splitting. C. Das, M. Tallarida, D. Schmeißer, EMRS-Spring meeting , May, 26-30, 2014, Lille, France
3. Electronic properties of TiO_2 films grown by atomic layer deposition. M. Tallarida, C. Das, D. Schmeißer, 20th International Conference on Electronic Properties of Two-Dimensional systems , July, 01-05, 2013, Wrocław, Poland
4. Linear dichroism and electrochemical properties of TiO_2 grown by atomic layer deposition on Si. C. Das, M. Tallarida, K. Skorupska, H.-J. Lewerenz, D. Schmeißer, 17th Workshop on Dielectrics in Microelectronics (WoDim 2012) June 25 - 27, 2012, Dresden
5. TiO_2 ALD on p-type Si to enhance and stabilize Si as photoelectrochemical absorber.
   C. Das, M. Tallarida, D. Schmeißer, K. Skorupska, H.-J. Lewerenz, AVS12th International Conference on Atomic Layer Deposition, June 17th to 20th, 2012, Dresden, Germany.
6. Investigation of Linear Dichroism in ALD layers of TiO_2.
   C. Das, M. Städter, M. Tallarida,D. Schmeißer, DPG-Spring meeting , March 25-30, 2012 Berlin

Curriculum Vitae

Since Auguest 2011	Ph.D student in BTU Cottbus –Senftenberg,
	Chair of Applied Physics and Sensors
	International Graduate School
October 2009 to Auguest 2011	Research Assistant
	Friedrcih Alexander University, Nurenberg-Erlangen
July 2007 to May 2009	Master of Technology
	Material Science Center
	Indian Institute of Technology Khragpur, India
November 2006 to April 2007	Teaching Physics to High School Student
	KendriyaVidyalay , Rourkel , India
July 2005 to June 2006	Bachelor in Education
	Sambalpur University, India
July 2003 to June 2005	Master of Science in Physics
	Sambalpur University, India
July 2000 to May 2003	Bachelor of Science
	Sambalpur University , India

Acknowledgement

I would like to express my keen gratitude to Prof. Dr. Dieter Schmeißer for providing me an opportunity to work on my PhD thesis with him. It was his advice and discussion on different scientific issue that led my work to reach at thesis level.

I would like to thank Dr. Massimo Tallarida, who was supervising me during my PhD work. He introduced me to the ALD and synchrotron experimental setups to perform experimental work and also very helpful in discussing the data and planning the experiments.

I am thankful to Dr. Karsten Hankel who help in things range from science to academics as well as he extended his help in personal level. He was main instrumental in corrected my thesis at a final level.

Many thanks to Dr. Matthias Richter for his help at BESSY, data analysis and facilitate with software to work without much difficulties.

I thank Dr. Ulrike Kramm who helped me to understand electrochemical methods and the analysis of the measurements.

I would like to thank Dr. Silma Alberton Correa for her help in work, correcting my thesis and valuable scientific inputs.

I am thankful to my peer group colleagues Jörg Haeberle, Simone Brizzi, Matthias Städter, Sakeeb Hassan Choudhery, Zied Rouissi, Shine Philip, Klaus Müller, Ioanna Poulumpa, Fabian Rachow Evgenia Charlafti, Johannes Israel, Carola Schwiertz for their help in my experiments and valuable suggestions. It was really nice to be with them in the Mensa to discuss ideas out of the world where the participants are mainly Zied and Simone.

I would like to thank Guido Beuckert for his help in setting of experimental setups and help to operate different instruments.

I am thankful to Dr. Małgorzata Sowinska for her help to finalize this thesis, printing them out and fruitful coffee times.

I am thankful to the International Graduate School of BTU to provide me financial assistance during my research work.

Finally, I will thank to the almighty GOD to lead me to this point of life, without his mercy it would not be possible.